Multiplication of microwave photons via inelastic Cooper pair tunneling

Romain Albert

Communauté
UNIVERSITÉ Grenoble Alpes

THÈSE

Pour obtenir le grade de

DOCTEUR DE LA COMMUNAUTÉ UNIVERSITÉ GRENOBLE ALPES

Spécialité : Physique de la Matière Condensée et du Rayonnement

Arrêté ministériel : 25 mai 2016

Présentée par

Romain ALBERT

Thèse dirigée par **François LEFLOCH**

et **Max HOFHEINZ**, Université de Sherbrooke

préparée au sein du **Laboratoire PHotonique, ELectronique et Ingéniérie QuantiqueS**
dans **l'École Doctorale Physique**

Multiplication de photons dans le domaine du micro-onde grâce au tunneling inélastique de paires de Cooper

Multiplication of microwave photons via inelastic Cooper pair tunneling

Thèse soutenue publiquement le **6 novembre 2019**,
devant le jury composé de :

Monsieur ÇAGLAR GIRIT
CHARGE DE RECHERCHE, COLLEGE DE FRANCE - PARIS, Rapporteur
Monsieur FRANK WILHELM-MAUCH
PROFESSEUR, UNIVERSITE DE LA SARRE - ALLEMAGNE, Rapporteur
Madame HELENE BOUCHIAT
DIRECTRICE DE RECHERCHE, CNRS ILE-DE-FRANCE GIF-SUR-YVETTE, Examinateur
Monsieur SERGE FLORENS
DIRECTEUR DE RECHERCHE, CNRS DELEGATION ALPES, Président
Monsieur ZAKI LEGHTAS
PROFESSEUR ASSOCIE, MINES PARISTECH, Examinateur

Remerciements

First, I would like to thank all of my jury members, Çağlar Girit, Frank Wilhelm-Mauch, Hélène Bouchiat, Serge Florens and Zaki Leghtas, for their involvement in this essential part of a PhD project. Your questioning and following discussions were extremely interesting and gave me others points of view on my work. Moreover, you were very available during the defense organization which was very appreciated during this stressful moment.

Ensuite, j'aimerais remercier très chaleureusement les personnes qui ont été au cœur même de ce projet. Tout d'abord, je dois beaucoup à l'encadrement scientifique de mon directeur de thèse Max Hofheinz qui m'a transmis l'ensemble des clés pour comprendre et mettre en œuvre ces expériences. Il m'a également permis d'acquérir une grande autonomie qui fût essentiel pour la conduite des expériences à Grenoble suite à son départ à Sherbrooke Je tiens à remercier mon deuxième directeur de thèse, François Lefloch, qui a notamment pris en charge les soucis du quotidien à Grenoble suite à ce départ. Vos nombreuses qualités humaines ont été déterminantes pour moi, autant dans les recherches menées que dans l'écriture de ma thèse.

Mes collègues, et amis avant tout, ont également été essentiel dans la réussite de cette thèse. I will begin with Dibyendu Hazra which was a post-doc working on the same project than me. Thank you for clearing the decks for me, it was essential to my sucecss ! Moreover, it was a real pleasure to work with you and your good humor. Ensuite, je me souviendrai toujours de mes premières mesures sur un échantillon de Sahla Jebari qui avait osé me les confier, merci de m'avoir fait confiance et pour ton dynamisme quotidien. Finalement, je tiens à souligner le courage de Florian Blanchet de m'avoir supporté pendant plus de deux ans dans notre bureau. Plus sérieusement, tes échanges quotidiens ont été plus qu'essentiel à la réussite de ma thèse et une bonne partie de ce travail n'aurait pas abouti sans ta présence.

Je dois également beaucoup à Frédéric Gustavo et Jean-Luc Thomassin qui ont fabriqué l'essentiel de mes échantillons, ma participation dans celle-ci n'aurai eu aucun effet sans votre implication et vos connaissances extensives en nano-fabrication. Par ailleurs, votre bonne humeur en salle-blanche m'a toujours aidé à garder le moral lors des nombreux échecs que nous avons affrontés.

Il me faut remercier Jean-Pascal Brison, vice-directeur de Pheliqs, et Marc Sanquer, directeur du Lateqs, qui m'ont toujours apporté leurs soutiens humains, scientifiques et administratifs. Dans ce cadre, je ne peux que transmettre toute ma gratitude à Marielle Perrier qui a supporté mes errements administratifs et a su les résoudre avec une efficacité redoutable.

Par ailleurs, il me faut également souligner l'importance des relations humaines au sein du laboratoire dans la réussite des thésards. Je ne peux que remercier chaudement les permanents du laboratoire, Claude, Silvano, Louis, Christophe, Xavier, Romain M., Vincent (et ta présence dans un C1 fantomatique pendant la fin de ma rédaction), Daniel, Georg, Alexandre, Michel, Iulian, Frédéric P. et Pierre, qui permettent de se sentir bien au sein du laboratoire. Les discussions autour de la machine à café ont été un plaisir quotidien, qu'elles aient été sur des sujets scientifiques ou beaucoup plus futiles parfois.

Ces années à Grenoble ont également été marquées par les rencontres et les activités avec les thésards et post-doc du laboratoire. Je commencerai en remerciant mes prédécesseurs, Alexandre A., Patrick, Juan-Carlos, Salha, Andrea et Alessandro, qui m'ont accueilli au sein du laboratoire et qui m'ont immédiatement intégré au sein de leurs sorties « Carré » du vendredi soir. Je remercie particulièrement Loic et Sahla pour les multiples soirées jeux qui furent organisées et grandement appréciées.

Je dois également remercier Florian B. qui non seulement me supportait au sein du laboratoire mais fut également très patient lors de nos nombreuses soirées escalades, tu m'as beaucoup aidé à progresser. Merci également de nous avoir accueilli chez toi pour de nombreuses soirées avec Estelle M., Anthony, Florian V. et Thomas que ce soit pour jouer ou regarder un bon film. Pour évoquer quelques souvenirs communs : Estelle et nos dimanches escalades pendant la rédaction, Anthony et les nombreuses parties de tarot, Florian V. et ses explications créatives de nouveaux jeux, Thomas et les nombreuses sorties montagnes ou ski que tu as organisées ou proposées ! Mon séjour à Grenoble aurait été plus terne sans toutes ces activités communes.

Je remercie également la nouvelle génération qui a beaucoup participé à l'ambiance du laboratoire, notamment, Tom, Agostino, Rami, Gonzalo et Nicolas P. Je dois notamment particulièrement remercier Cécile et Baptiste qui m'ont sortie du laboratoire pendant la rédaction ainsi que Florie et Estelle V. pour nos activités en montagne. Je tiens à distinguer également le plus suisse des post-doc Simon qui a toujours été extrêmement dynamique (et équipé) dans les activités d'extérieur, ainsi que volontaire pour une bonne bière.

Je dois également remercier l'équipe de Max à Sherbrooke, Sarah, Youcef, Charles-Alexis, Edouard et Hugo, pour leurs accueils chaleureux qui ont rendu mes deux passages très agréables. Je dois spécifiquement remercier Max et Eva Dupont-Ferrier (ainsi que son groupe à Sherbrooke) pour leur accueil lors de mes deux séjours à Sherbrooke, je dois dire qu'ils auraient été très solitaires sans vous. Je vous souhaite beaucoup de bonheur dans votre palace ! Je souhaite également beaucoup de courage à Joël qui a pris la suite de mon projet de thèse et je te souhaite une réussite éclatante dans ton travail.

Cette thèse s'est également nourrie d'amitiés extérieures au laboratoire. Merci Juliette pour le partage de très nombreuses randonnées et pour ta quiétude dans les galères, notamment météorologiques, qui a grandement participé à la joie qu'elles m'évoquent maintenant. Nicolas C., Guillaume, Lawana, Claire, Arnaud et Boris furent également les compagnons de nombreuses activités, j'attribuerai l'Eurovision à Nicolas, le Cornafion à Guillaume, une joyeuse galette à Lawana, la dent de Crolles à Claire, Orpierre à Arnaud et Catane à Boris.

Pour finir, je dois remercier ma famille qui m'a supportée toute au long de cette thèse et plus généralement au cours de mes études. Votre soutien dans les moments d'échecs et le partage des réussites furent extrêmement importants pour moi, Une pensée émue va à Gérard qui fut particulièrement important dans ma vocation de scientifique.

Abstract

During the last 15 years, many quantum optics experiments were reproduced with microwave photons using superconducting circuits by building on the strong interaction of electromagnetic fields with Josephson junctions.

This thesis focuses on the demonstration of a process where one microwave photon is converted to several photons at a different frequency. Contrary to phase-insensitive amplification, this multiplication can, in principle, be performed without added noise, thereby providing a building block for a simple single photon detector which is still missing for microwave photons.

In order to attain efficient photo-multiplication, strong nonlinear coupling is required. We have designed high-impedance resonators coupled to voltage-biased Josephson junctions in order to provide the necessary non-linearity. The high-impedance resonators are designed using planar coils and are fabricated together with SIS Josephson junctions in a niobium trilayer process providing low capacitance junctions.

Experimentally, we demonstrate the conversion from one to two photons with 80% efficiency and observe conversion from one to three photons, in agreement with theory. Cascading of at least two such multiplication stages should allow for discriminating an incoming one photon state from vacuum using a subsequent quantum limited amplifier, which can be realized using similar physics. Such a chain would then implement a number-resolving microwave single photon detector without dead time.

Résumé

Durant les quinze dernières années, un grand nombre d'expériences d'optique quantique ont été reproduites dans le domaine des micro-ondes. Ces expériences ont été rendues possible grâce à l'interaction entre les champs électromagnétiques et jonctions Josephson au sein de circuits intégrés supraconducteurs.

Cette thèse démontre l'existence d'un processus de conversion d'un photon dans le domaine des micro-ondes vers plusieurs photons possèdant une fréquence différente. Cette photo-multiplication n'impose théoriquement pas d'ajout de bruit, au contraire d'un processus d'amplification standard. Ce processus peut donc être à la base d'un détecteur de photon unique simple, ce qui n'existe pas encore à ces fréquences.

Pour obtenir une photo-multiplication efficace, un couplage non-linéaire fort est nécessaire. Nous avons conçu des résonateurs avec une grande impédance caractéristique et les avons couplés avec des jonctions Josephson polarisées avec une tension continue, la jonction étant à l'origine de la non-linéarité . Ces résonateurs sont constitués de bobines planaire et sont fabriqués simultanément aux jonctions Josephson grâce à un procédé exploitant une tri-couche de niobium. Ce procédé permet la fabrication de jonctions SIS de faible capacité parasite.

Expérimentalement, nous avons mesuré une conversion d'un photon vers deux photons avec une efficacité de 80% et observé la conversion d'un photon vers trois photons, en accord avec la théorie. En principe, ce processus peut être répété pour mettre au point un détecteur de photon unique, distinguant le nombre de photons simultanés en entrée. Un tel détecteur serait constitué d'au moins deux étages de photo-multiplication puis d'un amplificateur limité quantiquement en sortie.

Introduction

The goal of this thesis is to demonstrate that a Josephson junction polarized at a dc voltage can absorb a photon at one frequency and convert it into multiple photons at a different frequency. This work fits in the wider field of Josephson photonics, which relies on the interaction of quantum microwave radiation with the inelastic tunneling of Cooper pairs through dc-biased Josephson junction. In this field, single photon [1, 2] and coherent [3, 4] sources have already been demonstrated, just as microwave quantum limited amplification [5]. The device presented here is a step towards a single photon detector and therefore to complete this set of microwave tools.

This work is based on several decades of research, and we will present an overview of its scientific connections. Then, we will present the working principle of the device and outline the structure of this work.

Scientific context

The main non-linear element of our devices is a Josephson junction which is put out of equilibrium with a dc voltage. The charge tunneling induce a wide variety of effects which need to be understood. Tunneling events are probabilistic in most case, therefore they can induce quantum current fluctuations or shot noise, see [6] for review. Depending on the system, these fluctuations can be seen as quantum excitation or photons in an electromagnetic environment.

We present here several milestones in the understanding of the carrier tunneling properties and highlight important experimental and theoretical works. We will start by describing the Coulomb blockade effect which enlightens the impact of charging effects on tunneling. The induced quantum current fluctuations can be heavily modified by these charging effects, the coupling between the tunneling and the electromagnetic environment having a strong effect on their properties. This leads to the development of the dynamical Coulomb blockade theory which will be introduced. Later on, the technical progress made it possible to directly examine and engineer the shot noise which led to the apparition of the Josephson photonics field. It will be the core of our devices and is heavily linked to circuit Quantum ElectroDynamic (cQED).

We will also review the single photon detectors already demonstrated for microwave radiation in order to distinguish the advantages and drawbacks of our device.

Coulomb blockade

Coulomb blockade takes place in conducting islands coupled to wires through tunneling barriers. When the size of the island decreases, the carrier tunneling can be suppressed. This peculiar phenomenon is called Coulomb blockade with the apparition of a Coulomb gap in the conductance through the island.

To understand this effect, we need to look closely at the energy scales involved. The first energy scale is the charging energy, $E_C = q^2/(2C)$ where C is the capacitance of the island.

This energy is necessary in order to add a carrier with a charge q to it, it increases when the size of the island decreases as C decreases. The second energy is the electrostatic energy qV of the electron due to the voltage difference V between a lead and the island. When these two energy scales are similar, the tunneling can be suppressed due to the Coulomb repulsion of carriers inside the island. Notice that Coulomb blockade is only observed if the thermal energy k_BT is smaller than the charging and electrostatic energy.

The observation of Coulomb blockade requires the fabrication of very small islands. The first experiment [7] relies on the self organization in small particles from an ultra-thin metal film made by evaporation. The reduction of the film conductance at low temperature shows the suppression of tunneling between the particles due do Coulomb repulsion. Later on, the progress in nano-fabrication made it possible to purposefully design small islands [8] and theoretical progress provided good understanding of the phenomenon [9, 10]. The improvement of nano-fabrication led to the observation of Coulomb blockade phenomena in a very wide range of devices with different types of islands (piece of normal metal or superconductor, different kinds of quantum dots...).

Dynamical Coulomb blockade and inelastic Cooper-pair tunneling

Canonical Coulomb blockade is only observed in presence of islands, which translates generally to the observation of a strong Coulomb gap. For single tunnel junction devices with normal metal wire, the first measurement showed the existence of a slight Coulomb gap in their conductance at low biasing voltage [11, 12]. However, this gap was considerably suppressed compared to canonical Coulomb blockade.

To understand its origins, we need to look at the impact of the environment and the density of states of the junction. We represent in figure 1, the schematic of a typical experiment in a). The impedance presents a resonance here to illustrate its impact, but the first experiments had an ohmic behavior.

We first focus on the behavior of the system with normal tunnel junction which is represented in b). At low biasing voltage, the conductance channels come from the carrier tunneling from occupied state to empty state with the same energies, then they relax to the Fermi sea. When the environment is shaped as presented, the resonance induces additional conductance channels. A carrier can dissipate part of its energy in the resonator, if its energy is higher than the resonator excitation energy. Therefore, for $eV > \hbar\omega_0$, the conductance increases. For nearly flat impedance, this effect is present too, but only significant for a high impedance environment compared to the quantum of resistance $R_H = h/e^2 = 25.8\,\mathrm{k}\Omega$. This explains the suppression of the Coulomb gap for the first experiments, see [13] for the first experiment with high impedance and a strong Coulomb gap.

The early theoretical works [14, 15] explained the origin of the effect and the importance of high impedance environments to enhance its impact. These theoretical developments led to the $P(E)$ theory [16, 17] which provides a quantitative explanation for these measurements.

Until now, we have only considered normal tunnel junctions. The behavior of Josephson junctions is a bit different due to the difference in the density of state. In figure 1 c), we represent the density of state of Cooper pairs for a Josephson junction. We only consider biasing voltage under the superconducting gap and therefore neglect the quasi-particle

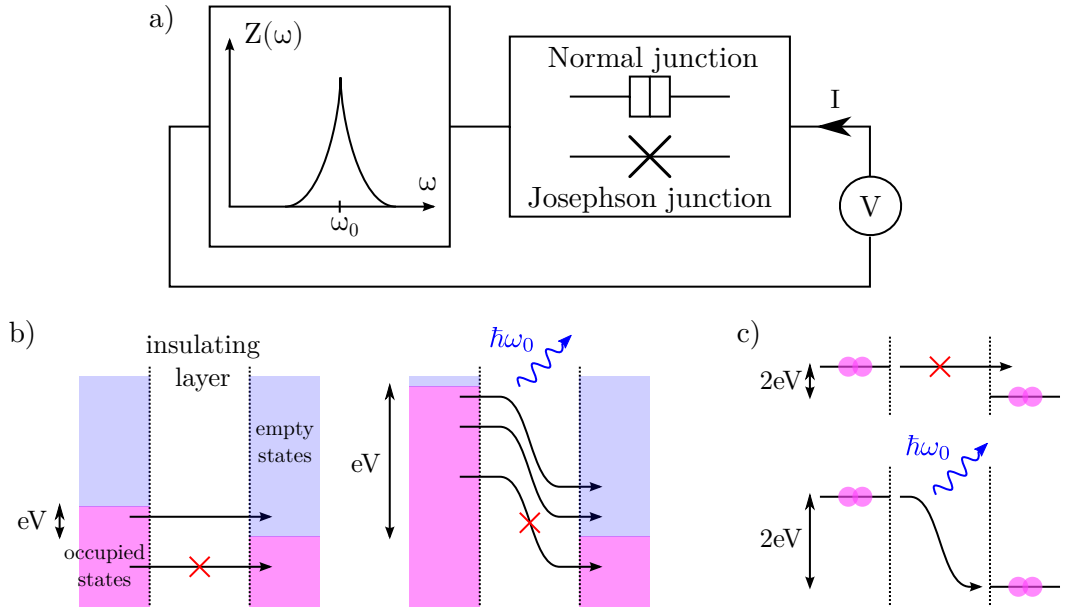

Figure 1: a) Schematic of a typical experiment for the measurement of the dynamical Coulomb blockade phenomenon. Depending on the materials used, the junction is either a normal tunnel junction or a Josephson junction. It is coupled to an electromagnetic environment (with a resonance here) and a dc-voltage source. b) Density of states for the two leads of a normal tunnel junction with an insulating layer in between. On the left, we present the classical behavior, the carrier can tunnel from occupied state to empty state and the number of these channels depends on the dc-biasing voltage V. However, if there is a resonance in the environment, additional conductance channels can appear, as presented on the right. The carrier tunneling can be associated with an excitation of the environment, if the carrier energy is high enough. c) We represent the density of states under the gap of a Josephson junction, in that case, only the Cooper-pair condensates are important. Without the environment, the tunneling of a carrier is impossible as the Cooper pairs cannot dissipate their energies. However a conduction channel appears when the tunneling energy of a Cooper pair exactly matches the energy of an excitation of the environment.

branches. Classically, no dc-current can flow through the junction for a finite dc-voltage, as the Cooper pairs cannot dissipate their energies during the tunneling. By coupling the system with resonances in the environment, we create dissipation channels which authorize the tunneling. Therefore, peaks of dc-current are expected when the tunneling energy of a Cooper pair $2eV$ matches exactly the energy of an excitation in the system $\hbar\omega_0$. This effect is what we call inelastic Cooper-pair tunneling.

This effect was first observed in [18], the main schematic and the result is presented in figure 2. The sample is constituted by a $\lambda/4$ transmission-line resonator and a Josephson junction. The environment impedance presents a peak for each resonance of the transmission line resonator, at every odd harmonic of the fundamental resonance frequency. The result shows peaks of current for specific voltages V_1, V_2... They can be easily explained with the energy conservation: V_1 corresponds to the creation of one photon at the funda-

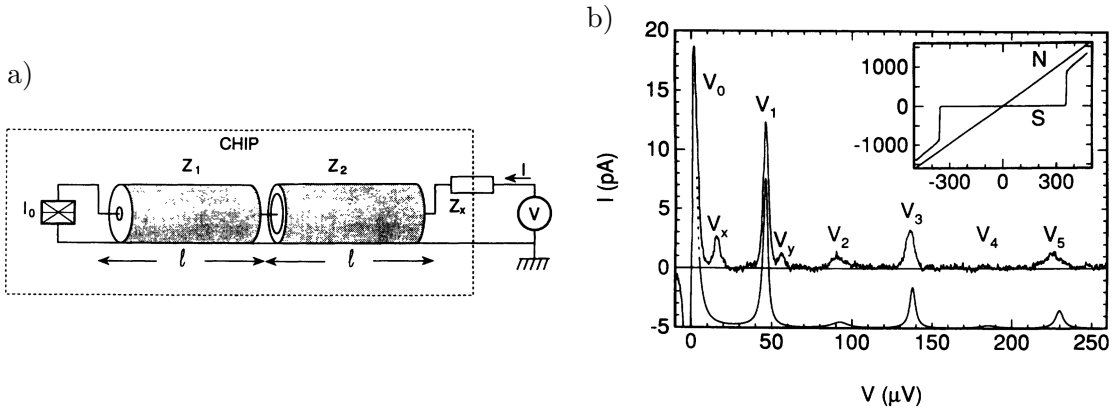

Figure 2: a) Electrical schematic of the sample, a Josephson junction is coupled to a $\lambda/4$ transmission line resonator and the current going through it is measured. b) Current as a function of the biasing voltage, the bottom line is computed with the $P(E)$ theory. The drawing are extracted from [18].

mental frequency for the tunneling of one Cooper pair and V_3 corresponds to the creation of one photon at the first odd harmonic. V_2 corresponds to a higher order process, indeed, the tunneling of one Cooper pair gives rise to two photons at the fundamental frequency. All the peaks can be understood with the same description, except for V_x and V_y which are parasitic resonances of the ground plane.

Circuit Quantum ElectroDynamics and Josephson photonics

In the early 90s, it was technically only possible to measure the current. The development of ultra-low noise microwave amplifiers in the 2000s allowed for the direct measurement and manipulation of microwave photons. In conjunction, the field of circuit Quantum Electro-Dynamics (cQED) expands rapidly, notably with the boom of superconducting Qubits [19, 20]. In nearly all cQED experiments, the Josephson junction is used in its superconducting state and the control is done with microwave radiation.

The field of Josephson photonics appeared at the beginning of the 2010s with the first measurement of the electromagnetic field emitted by a dc-bias Josephson junction coupled to a resonator [3].

In figure 3 a), the sample and measurement apparatus are represented. We recognize a transmission line resonator coupled to a Josephson junction polarized with a dc voltage. The measurement is performed simultaneously on the radio-frequency side and low frequency side to obtain the result presented in figure 3 b). The main observation is the confirmation of our interpretation that each Cooper pair emits a photon inside the resonator, which then leaks to a microwave amplifier: The tunneling rate closely matches the photon emission rate. Moreover, the $P(E)$ theory explains quantitatively these measurements.

Since this experiment, the field of Josephson photonics was expanded with the measurement of single photon sources [1, 2], the observation of lasing [4] or the emission of non-classically correlated fields [21]. Measurements of scattering of microwave radiation by such systems show near quantum limited amplification [5] without the need of a strong

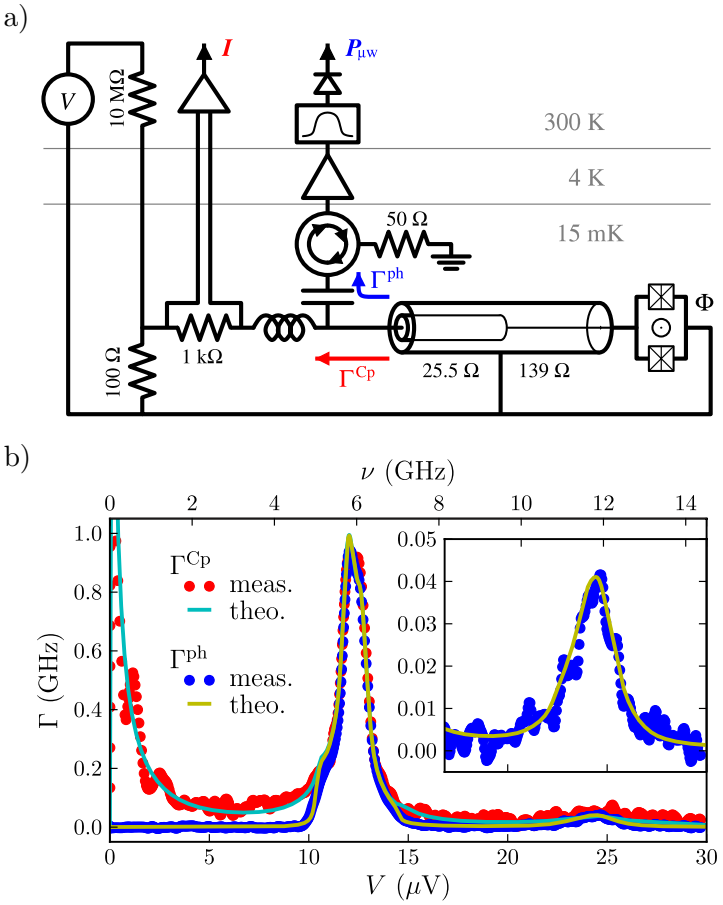

Figure 3: a) Electrical schematic of the sample and of the measurement scheme. The sample is very similar to figure 2 a) with a transmission line resonator coupled to a SQUID which acts as a Josephson junction. The current and the emitted microwave power is simultaneously measured. b) Γ^{Cp}, Cooper-pair tunneling rate, and Γ^{ph}, the photon emission rate, as a function of the biasing voltage. The theoretical curve are computed with the $P(E)$ theory. The drawings are extracted from [3].

radio-frequency field for input power as for classical quantum limited amplifiers [22–24].

Single photon detector for microwave frequencies

There is currently no off-the-shelf single photon detector for microwave frequencies, even if a lot of efforts are put forward. We first explain why amplification is not enough to detect a single photon, and then we will review what is currently used for detection.

We spoke about quantum limited amplifier, but we did not explain what it is before. From quantum mechanics, one can show [25] that a phase insensitive amplifier adds at least half a photon of noise (for a high gain amplifier). This comes from the unavoidable mixing of the signal with an idler signal which contains at least the vacuum fluctuations. This added noise prevents the distinction of a single photon state from vacuum, therefore, an amplifier is not enough to create a single photon detector.

We focus on the detection of single photon in the low frequency part of the microwave domain: 1-50 GHz. For higher frequencies, other schemes such as bolometers [26] or microwave kinetic inductance detectors [27] can be used thanks to the higher photon energy. They are notably used for radio-astronomy.

For low frequency microwave radiation, the main schemes imply the use of superconducting Qubits. In broad outline, it is initialized in its ground state, if a photon arrives, the Qubit can absorb it and become excited. Then the Qubit is read and a photon is detected, if it is in the excited state. The main difficulty of this system is that the probability of the system to go back to the ground state and release the photon is high without careful engineering. Notice that there are a lot of other theoretical propositions [28–30] which we will not explain here.

The first device was the so-called Josephson Photo-Multiplier (JPM) [31–33]. Schematically, it is a phase Qubit which is tuned to present different escape rates for its ground and existed states to a continuum. The system is initially put in the ground state with a very low escape rate. If a photon is absorbed, the excited state tunnels rapidly to the continuum, which prevents the photon to be released and the system to go back to the ground state. The escape from the excited state translates to a peak of voltage which marks the absorption of a photon. The main limitation of this device is the need to regularly initialize the system in the ground state, as the ground state eventually also escapes.

In order to break the reverse process, another possibility is to convert an incoming photon into an excitation of a Qubit and a waste photon which is designed to rapidly leak from the system. When the waste photon is no more in the system, the Qubit is trapped in the excited state and can be read. This principle was realized with a three level system [34] and with a Qubit coupled to two resonators with very different bandwidth [35]. Notice that these devices need as well to be regularly initialized to the ground state and take a bit of time to be read, therefore there is always a dead time.

Photo-multiplication process

The goal of this thesis is to use the strong non-linear light-matter interaction in dc-biased Josephson junctions to convert an incoming photon into several outgoing photons at a different frequency. In this conversion process, the quantum limitation on the added noise of amplification is no more relevant. Therefore, such a device provides an increase of power without added noise in principle. It can be used to displace the input state further away from vacuum in order to detect it through subsequent phase-insensitive amplification and can be the first stage of a single photon detector without dead-time. Moreover, its linearity allows to measure the input photon number in principle.

To realize this photo-multiplier, we consider a device which is constituted of two resonators, an input and output resonator (the distinction is arbitrary here). These resonators interact through a dc-biased Josephson junction and are coupled to transmission lines, as presented in figure 4. The idea behind the photo-multiplication effect is to absorb a single photon to emit several output photons by using the tunneling of a Cooper pair to supply the missing energy. By tuning the dc-bias voltage V, we can reach the resonance of the

conversion from one photon to n photons:

$$2eV_n + \hbar\omega_i = n\hbar\omega_o$$

It is interesting to note that the leaking of an output photon prevents the system to go back, as there is not enough energy for the reverse phenomenon anymore.

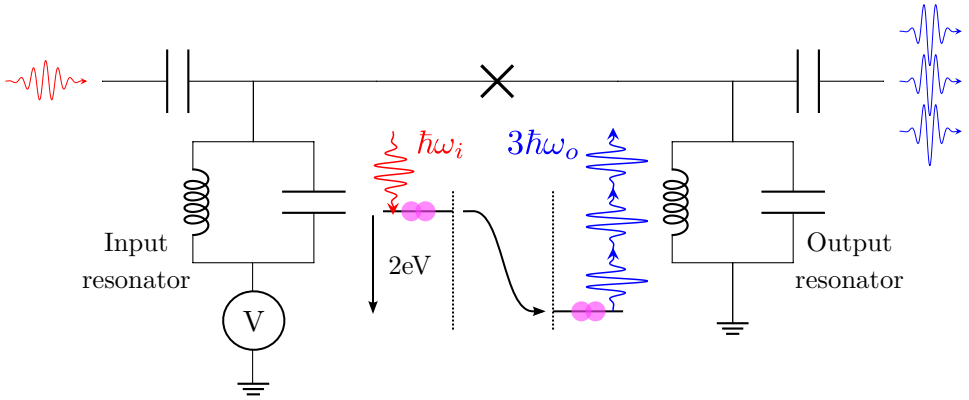

Figure 4: We consider a sample consisting of two resonators coupled to a dc-biased Josephson junction. These resonators are capacitively coupled to transmission lines which allows for applying and measuring microwave radiation. The goal of this thesis is to characterize the possibility of absorbing one photon while emitting several photons in the other mode with the simultaneous tunneling of a Cooper pair. We present in the center of the image the energy conservation for the conversion of one photon to three photons.

As we see in figure 3, the amplitudes of the multi-photons emission peaks are small compared to the emission of one photon peak. This is due to the low characteristic impedance Z_c of the mode of emission. Indeed, the ratio of the two peaks is given by the $P(E)$ theory as $\frac{\pi Z_c}{2R_Q}$ where $R_Q = h/(4e^2) = 6.5\,\mathrm{k}\Omega$. To increase the amplitude of multi-photons processes, one needs to reach high characteristic impedance [1].

Notice that, a very similar device was studied before [21] to measure the non-classical correlation between the simultaneous emission photons to both sides. However, the two resonators possessed low characteristic impedances and the photon multiplication effect was not observed.

Thesis structure

This thesis is divided in five chapters, we will first review the theory and then explain the nano-fabrication and its limitations. Using this two elements, we will present the design of our sample. We will then describe the experimental measurement scheme, before presenting results from a photo-multiplier sample. We will now give a short overview for each chapter.

Chapter 1: Theoretical elements of inelastic Cooper pair tunneling

We first introduce the $P(E)$ theory and its properties to understand the emission properties of our devices. We notably apply it to an example and propose an approximate treatment

in order to obtain a better grasp of this theory. This theory will be extremely useful to verify the behavior of the electromagnetic environment on our actual device in last chapter.

Secondly, we present an input-output treatment of the same device in order to derive its elastic and inelastic scattering properties. We notably show that a perfect conversion of one photon to several photons is possible when the Josephson energy of the system is tuned. Moreover, we present the existing trade-off between the dark-noise of the processes, the dynamical range and the bandwidth.

Chapter 2: Device fabrication

We present the nano- fabrication process which is based on a trilayer of Niobium/Aluminum-Aluminum oxide/Niobium forming the Josephson junction. We show how it is patterned and connected with additional layers of insulating silicon nitride and niobium. We present how we can fabricate our base elements, namely Josephson junctions, capacitors, transmission lines and high impedance resonators (made from planar coils).

Each of these elements were independently measured. Their experimental and numerical characterizations are presented and compared. We notably show that the Sonnet simulation must be careful considered, parasitic capacitance changes heavily with the dielectric stack considered. These measurement fix limits for the design of the sample.

Chapter 3: Sample design

We explain the design of two samples. The first sample uses transmission line resonator and is conceived to test the experimental setups. To complete it, we put the bias-T on the chip itself for the first time in our group.

The second sample is a photo-multiplier device. The SQUID is coupled to two planar coils which form the input and output resonators, a transmission line transformer is added to increase the bandwidth of the output resonator. We present its physical implementation and extract the parasitic elements to estimate their impact.

Chapter 4: Experimental setup

We start by describing the radio-frequency measurement scheme, we first explain the role and organization of its numerous physical elements. Then we present how we measure the power spectral density, which constitutes the key measurements we will use to characterize the photo-multiplier. We finally explain how this scheme can be used to fully calibrate the experiment.

In a second part, we explain how we dc-bias our device. Indeed, we need to impose a flux through the SQUID to control its Josephson energy and a dc-voltage on it. We work in particular on the voltage-biasing of the junctions as extremely low voltage noise is needed.

Chapter 5: Experimental results

We divide this chapter into two parts, first we study the self-emission properties of the system and extract the resonator characteristics. Moreover, we describe what happens

when we leave the range of validity of $P(E)$ approximation. We notably observe emission with the simultaneous tunneling from several Cooper pairs.

In the second part, we explore the scattering of microwave radiation by the system and measure a highly efficient conversion of one photon to two photons. We show that the conversion of one photon to three photons exists but cannot reach the same efficiency due to the limited Josephson energy of the SQUID in the device we explored.

Contents

Chapter 1

Theoretical elements of inelastic Cooper-pair tunneling

Contents

The goal of this chapter is to introduce the theoretical elements necessary to understand the working principle of our samples. We will start to review the effect of dissipation on the tunneling of Cooper pair described by dynamical Coulomb blockade theory. Then, we will apply it to a typical example in an approximated approach which will give us a more intuitive understanding of the implied physics. Finally, we will explain how we can engineer the electromagnetic environment of a Josephson junction to generate a photon multiplication effect.

The quantization of superconducting circuits is well explained in [36] (updated version of [37]) and will be heavily used in this chapter. Moreover, the review [38] is a great resource to understand the link between quantum world and the classical measurements we are able to perform at the end of the experimental scheme.

1.1 Photon emission through inelastic Cooper-pair tunneling

As already discussed in the introduction, photon-emission is described by dynamical Coulomb blockade theory. We will review this theory here, starting first with a description of dissipation in quantum mechanics. We will then use it to compute its impact on a tunnel Josephson junction in order to understand dissipation via spontaneous emission.

1.1.1 Dissipating electromagnetic environment

One difficulty of quantum mechanics is to describe the dissipation of energy in quantum systems, as they break the unitary evolution of isolated quantum system. The common way to model it is to couple the system to an infinite number of degrees of freedom which can then absorb the energy. We focus on the Caldeira-Leggett model here, another option, the input-output formalism, will be introduced in section 1.3. This presentation follows closely [36].

The idea behind the Caldeira-Leggett model is to map a general impedance $Z(\omega)$ to an infinite number of LC resonators in series, as presented in figure 1.1. It is important to remember that it only works for elements which can be described by an impedance, therefore it only describes linear dissipation. The impedance of two-terminal electrical components is defined through a convolution with a linear response function $Z(t)$:

$$v(t) = \int_{-\infty}^{\infty} \mathrm{d}t' Z(t') i(t - t') \tag{1.1}$$

Most of the time, we use its Fourier transform:

$$Z[\omega] = \int_{-\infty}^{\infty} \mathrm{d}t Z(t) \exp(\mathrm{i}\omega t) \tag{1.2}$$

We will retain this convention for this thesis[1]. Notice that this convention is different from the one commonly used in electrical circuits, so to be coherent we will use $\mathrm{j} = -\mathrm{i}$ when we describe them.

The impedance of an LC resonator is purely imaginary and presents a divergence at the resonance frequency. These two properties make it hard to describe a general impedance with a series of LC resonators. To treat correctly the infinite series, which possesses a non-zero real part, we define a generalized impedance:

$$\tilde{Z}[\omega] = \lim_{\substack{\eta \to 0 \\ \eta > 0}} \int_{-\infty}^{\infty} \mathrm{d}t Z(t) \exp[\mathrm{i}(\omega + \mathrm{i}\eta)t] \tag{1.3}$$

The generalized admittance of the k-th LC resonator is:

$$\tilde{Z}_k[\omega] = Z_k \left\{ \frac{\pi \omega_k}{2} [\delta(\omega - \omega_k) + \delta(\omega + \omega_k)] + \frac{\mathrm{i}}{2} \left[\mathrm{p.v.} \left(\frac{\omega_k}{\omega - \omega_k} \right) + \mathrm{p.v.} \left(\frac{\omega_k}{\omega + \omega_k} \right) \right] \right\} \tag{1.4}$$

[1] The inversion is: $Z(t) = 1/(2\pi) \int_{-\infty}^{\infty} \mathrm{d}\omega Z[\omega] \exp(-\mathrm{i}\omega t)$.

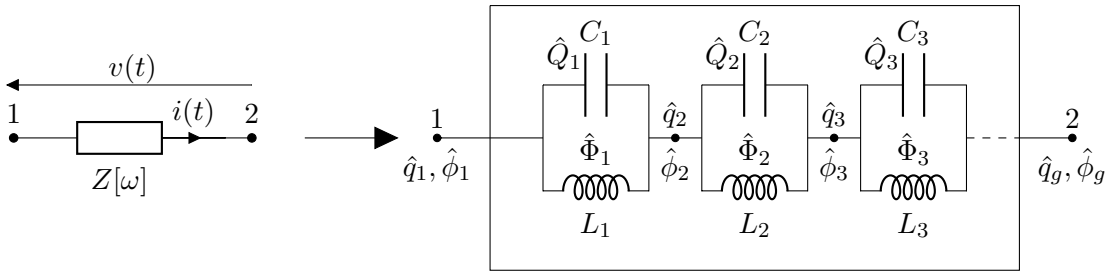

Figure 1.1: The impedance $Z[\omega]$ is transformed to an ensemble of LC resonators in the Caldeira-Legett Model. These resonators can be described by two sets of variables, the charge $\hat{q}_k$ and flux $\hat{\phi}_k$ at the node k or the flux $\hat{\Phi}_k$ through the inductor k and the charge $\hat{Q}_k$ of the capacitor k. For the quantization, one side of the impedance is connected to the ground which is indicated by $\hat{q}_g, \hat{\phi}_g$.

where p.v. indicates the Cauchy principal value and[2]:

$$\omega_k = k\Delta\omega \quad \text{and} \quad Z_k = \frac{2\Delta\omega}{\pi\omega_k}\mathrm{Re}(Z[\omega_k]) \tag{1.5}$$

The generalized impedance can be written as a series of the impedance of the LC resonators. The real part of an impedance can then be replaced by a dense comb of delta functions, while the imaginary part comes from the Cauchy principal value[3]:

$$\tilde{Z}[\omega] = \lim_{\Delta\omega\to 0}\lim_{K\to\infty}\sum_{k=1}^{K}\tilde{Z}_k[\omega] \tag{1.6}$$

The Hamiltonian of the series of LC resonator can be written:

$$\hat{H}_{env} = \sum_{k=1}^{K}\left[\frac{\hat{Q}_k^2}{2C_k} + \frac{\hat{\Phi}_k^2}{2L_k}\right] = \sum_{k=1}^{K}\hbar\omega_k\hat{a}_k^\dagger\hat{a}_k \tag{1.7}$$

where the coupling can be computed with the flux and charge of node 1:

$$\hat{\phi}_1 = \sum_{k=1}^{K}\hat{\Phi}_k = \sum_{k=1}^{K}\sqrt{\frac{\hbar Z_k}{2}}\left(\hat{a}_k + \hat{a}_k^\dagger\right) \quad \text{and} \quad \hat{q}_1 = \hat{Q}_1 = \sqrt{\frac{\hbar}{2Z_1}}\frac{\left(\hat{a}_1 - \hat{a}_1^\dagger\right)}{\mathrm{i}} \tag{1.8}$$

The natural variables of quantization are the inductor fluxes and the capacitor charges. In general, the quantization is done through the charge and flux at the node (or loops) of the circuit as it directly eliminates superfluous degree of freedom. The correspondence with this method is given in appendix A.1.

From equation (1.6), we can see that there are two limits to be taken. The first one $K \to \infty$ pushes the cut-off frequency to the infinite and the second one $\Delta\omega \to 0$ creates the **dense** delta comb[4]. In principle, they need to be carefully taken into account as they create divergences (common in quantum field theory). The original article of Caldeira-Leggett [39] used the path integral formalism for this reason. Here, we will stick to the canonical quantization, and we will ignore these divergences.

[2] Or in equivalent term: $C_k = \frac{\pi}{2\Delta\omega\mathrm{Re}(Z[\omega_k])}$ and $L_k = \frac{2\Delta\omega}{\pi\omega_k^2}\mathrm{Re}(Z[\omega_k])$

[3] This Cauchy principal value enforces the Kramers-Kronig relations for the impedance.

[4] Notice that we choose to not treat the case of finite impedance at zeros impedance which need a slight modification to this LC resonator array, see [36].

1.1.2 Cooper-pair tunneling

We would like to compute the effect of the electromagnetic environment, described by an arbitrary impedance $Z[\omega]$, on the tunneling of Cooper pair in a Josephson junction, see [16] for reference. The environment and the Josephson junction are put out of equilibrium by a voltage bias in series with them, as shown in figure 1.2. We will first write the Hamiltonian, then solve it to compute the DC current through the junction.

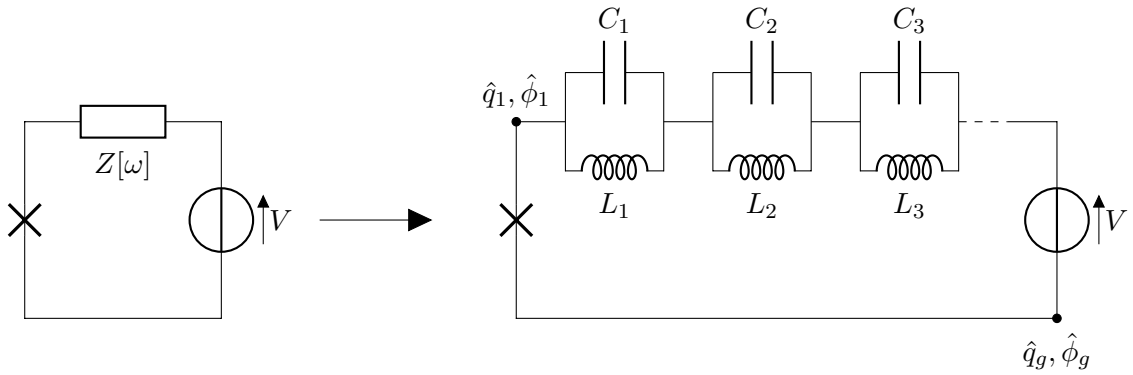

Figure 1.2: We consider the circuit on the left, notice that we choose to absorb the capacitance of the Josephson junction inside the impedance $Z[\omega]$. It is described with the Caldeira-Leggett decomposition on the right.

The Hamiltonian of the system can be divided in two parts, the environment and the Josephson junction:

$$\hat{H} = \hat{H}_{env} + \hat{H}_J \quad \text{with} \quad \hat{H}_J = E_J \cos \frac{\hat{\Phi}_J}{\Phi_0} \tag{1.9}$$

where $\hat{\Phi}_J$ is the flux across the junction, E_J its energy and $\Phi_0 = \hbar/(2e)$ the flux quantum.

The flux across the junction can be expressed as a function of the environment variable and biasing voltage:

$$\hat{\Phi}_J = \hat{\phi}_1 + \hat{\Phi}_V = \sum_{k=1}^{K} \hat{\Phi}_k + \hat{\Phi}_V \tag{1.10}$$

where $\hat{\Phi}_V$ is the flux induced by the DC-bias voltage. The flux through a branch is related to the voltage across this branch through the relation:

$$\Phi(t) = \int_{-\infty}^{t} V(t')\mathrm{d}t' \quad \text{therefore} \quad \hat{\Phi}_V(t) = Vt + A \tag{1.11}$$

Notice that $\Phi(t)/\Phi_0$ is consistent with the AC Josephson effect and that A can be eliminated trough a change in the time origin.

In second quantization, the Hamiltonian of the junction can be written:

$$\hat{H}_J = E_J \cos\left[\sum_{k=1}^{K} g_k\left(\hat{a}_k + \hat{a}_k^\dagger\right) + \omega_J t\right] = \frac{E_J}{2} \prod_{k=1}^{K}\left[e^{\mathrm{i}g_k\left(\hat{a}_k + \hat{a}_k^\dagger\right)}\right] e^{\mathrm{i}\omega_J t} + \text{h.c.} \tag{1.12}$$

with $g_k = \sqrt{\frac{2e^2 Z_k}{\hbar}} = \sqrt{\frac{\pi Z_k}{R_Q}}$ and $\omega_J = \frac{2e}{\hbar}V$. $R_Q = \frac{h}{4e^2}$ is the superconducting resistance quantum.

From the Hamiltonian of the system, we want to compute the Cooper pair tunneling rate through the junction. To solve this problem, we compute the tunneling rate using Fermi's golden rule using $\hat{H}_J$ as perturbation, as we know the eigenstates of $\hat{H}_{env}$. The limitations of this perturbation theory will be treated later in section 1.2.4. We concentrate first on transition where the Cooper pair transfers its energy to the environment. The transition rate from an initial state $|i\rangle$ to a final state $|f\rangle$ of the environment can be written:

$$\vec{\Gamma}_{i\to f} = \frac{2\pi}{\hbar}\left|\langle f|\,\hat{H}_J\,|i\rangle\right|^2 \delta(E_f - E_i) \tag{1.13}$$

Notice that the arrow denotes the fact that the Cooper pair tunnels from the side of the junction with the highest potential to the other side.

We use the fact that $\hat{H}_J$ is a harmonic perturbation and only keep the excitation term:

$$\vec{\Gamma}_{i\to f} = \frac{\pi E_J^2}{2\hbar}\left|\langle f|\prod_{k=1}^{K} e^{\mathrm{i}g_k\left(\hat{a}_k+\hat{a}_k^\dagger\right)}\,|i\rangle\right|^2 \delta(E_f - E_i + \hbar\omega_J) \tag{1.14}$$

Notice that the reverse process, the tunneling of a Cooper pair with absorption of energy from the environment, differs only by a sign $-$ before the ω_J in the delta function. Therefore, it can be computed with taking $-V$ instead of V.

The total rate of Cooper-pair tunneling can then be written:

$$\vec{\Gamma} = \sum_i \sum_f \vec{\Gamma}_{|i\rangle\to|f\rangle} P_\beta(|i\rangle) = \frac{\pi E_J^2}{2\hbar}\sum_{|i\rangle}\sum_{|f\rangle}\left|\langle f|\prod_{k=1}^{K} e^{\mathrm{i}g_k\left(\hat{a}_k+\hat{a}_k^\dagger\right)}\,|i\rangle\right|^2 P_\beta(|i\rangle))\delta(E_f - E_i + \hbar\omega_J) \tag{1.15}$$

where $P_\beta(|i\rangle)$ is the probability to find the environment in the initial state $|i\rangle$.

In the initial thermal state, the resonators are independent. This is why, we can write the initial and final states as a tensor product of the eigenstates of $\hat{a}_k^\dagger\hat{a}_k$, $|i\rangle = \otimes_k |n_k\rangle$:

$$\vec{\Gamma} = \frac{\pi E_J^2}{2\hbar}\sum_{n_1,n_2\cdots}\sum_{m_1\cdots}\prod_{k=1}^{K}\left|\langle m_k|\, e^{\mathrm{i}g_k\left(\hat{a}_k+\hat{a}_k^\dagger\right)}\,|n_k\rangle\right|^2 P_{k,\beta}(|n_k\rangle)\frac{1}{\hbar}\delta\left(\sum_{k=1}^{K}[m_k - n_k]\omega_k + \omega_J\right) \tag{1.16}$$

Notice that $P_{k,\beta}(|n_k\rangle)$ is now the state probability to find the individual k resonator in the state $|n_k\rangle$.

By taking the Fourier transform of the delta function and writing the operator in the Heisenberg picture, we can reorganize the sum to simplify it, see appendix A.2 for details. We obtain:

$$\vec{\Gamma}(\omega_J) = \frac{\pi E_J^2}{2\hbar^2}\int_{-\infty}^{\infty}\mathrm{d}t\,\exp\underbrace{\left[\sum_{k=1}^{K} g_k^2\left\langle\left(\hat{a}_k(t)+\hat{a}_k^\dagger(t)-\hat{a}_k(0)-\hat{a}_k^\dagger(0)\right)\left(\hat{a}_k(0)+\hat{a}_k^\dagger(0)\right)\right\rangle\right]}_{J(t)} e^{\mathrm{i}\omega_J t} \tag{1.17}$$

We can recognize the Fourier transform of the exponential of the function $J(t)$. The $J(t)$ function is usually called the phase-phase correlation function as it can be simply expressed in term of the phase correlation function of the junction:

$$\boxed{J(t) = \frac{1}{\Phi_0^2}\sum_{k=1}^{K}\left\langle\left(\hat{\Phi}_k(t)-\hat{\Phi}_k(0)\right)\hat{\Phi}_k(0)\right\rangle = \frac{1}{\Phi_0^2}\left\langle\left(\hat{\phi}_1(t)-\hat{\phi}_1(0)\right)\hat{\phi}_1(0)\right\rangle} \tag{1.18}$$

This function can be expressed with the usual correlation function of the harmonic oscillator:

$$\begin{aligned} J(t) &= \sum_{k=1}^{K} \frac{2\Delta\omega}{\omega_k R_Q} \mathrm{Re}(Z[\omega_k]) \left\{ \coth\left(\frac{\beta\hbar\omega_k}{2}\right)[\cos(\omega_k t) - 1] - \mathrm{i}\sin(\omega_k t) \right\} \\ &\underset{\substack{K\to\infty \\ \Delta\omega\to 0}}{=} 2\int_0^\infty \frac{\mathrm{d}\omega}{\omega} \frac{\mathrm{Re}(Z[\omega])}{R_Q} \left\{ \coth\left(\frac{\beta\hbar\omega}{2}\right)[\cos(\omega t) - 1] - \mathrm{i}\sin(\omega t) \right\} \end{aligned} \tag{1.19}$$

Notice that the harmonic oscillator are supposed in thermal equilibrium, which is a strong hypothesis of this theory.

We finally obtain:

$$\vec{\Gamma} = \frac{\pi}{2\hbar^2} E_J^2 P'[\omega_J] \quad \text{where} \quad P'[\omega_J] = \frac{1}{2\pi}\int_{-\infty}^{\infty} \mathrm{d}t \exp(J(t) + \mathrm{i}\omega_J t) \tag{1.20}$$

More usually, the tunneling is expressed in term of the $P(E)$:

$$\vec{\Gamma}(V) = \frac{\pi}{2\hbar} E_J^2 P(2eV) \quad \text{where} \quad \boxed{P(E) = \frac{1}{2\pi\hbar}\int_{-\infty}^{\infty} \mathrm{d}t \exp\left(J(t) + \mathrm{i}\frac{E}{\hbar}t\right)} \tag{1.21}$$

We can deduce the current through the Josephson junction:

$$\boxed{I(V) = 2e\left(\vec{\Gamma}(V) - \overleftarrow{\Gamma}(V)\right) = \frac{e\pi}{\hbar} E_J^2 (P(2eV) - P(-2eV))} \tag{1.22}$$

This theory was very successfully used to explain the tunneling current of DC-bias Josephson junctions coupled to resonators [18].

1.1.3 Photon emission in dynamical Coulomb blockade

To compute the radiation emission, two methods are presented in [3]. We will stick here to the explanation using the current-current correlation function.

The current operator through the Josephson junction is defined by [36]:

$$\hat{I} = \frac{2e}{\hbar} E_J \sin\left(\frac{\hat{\Phi}_J}{\Phi_0}\right) = \frac{e}{\hbar} E_J \left[\exp\left(\mathrm{i}\frac{\hat{\Phi}_J}{\Phi_0}\right) - \exp\left(-\mathrm{i}\frac{\hat{\Phi}_J}{\Phi_0}\right)\right] \tag{1.23}$$

Therefore, the current-current correlation function can be written in the Heisenberg picture:

$$S_{II}(t) = \left\langle \hat{I}(t)\hat{I}(0) \right\rangle = \frac{e^2 E_J^2}{\hbar^2} \left[\left\langle e^{\mathrm{i}\frac{\hat{\Phi}_J(t)}{\Phi_0}} e^{-\mathrm{i}\frac{\hat{\Phi}_J(0)}{\Phi_0}} \right\rangle + \left\langle e^{-\mathrm{i}\frac{\hat{\Phi}_J(t)}{\Phi_0}} e^{\mathrm{i}\frac{\hat{\Phi}_J(0)}{\Phi_0}} \right\rangle \right] \tag{1.24}$$

We can write the current-current correlation function as a function of the phase-phase correlation function and compute the current noise density with the Wiener-Khinchin theorem:

$$S_{II}(V,\omega) = \frac{2\pi e^2 E_J^2}{\hbar} (P(2eV - \hbar\omega) + P(-2eV - \hbar\omega)) \tag{1.25}$$

From this equation, we can deduce the power spectral density and the photon emission rate density:

$$\gamma(V,\omega) = \frac{PSD(V,\omega)}{\hbar\omega} \quad \text{with} \quad PSD(V,\omega) = 2\mathrm{Re}(Z[\omega])S_{II}(V,\omega) \tag{1.26}$$

Therefore, we can write the photon emission rate density as:

$$\boxed{\gamma(V,\omega) = \frac{\pi^2 E_J^2}{\hbar\omega}\frac{2\mathrm{Re}(Z[\omega])}{R_Q}(P(2eV-\hbar\omega)+P(-2eV-\hbar\omega))} \tag{1.27}$$

The photon emission from the system is deeply linked with the tunneling of Cooper pair through the $P(E)$ function. However, as described in section 1.1.2, this function is a very non-linear transformation from the impedance and it is complicated to get an intuitive understanding of it. However, general properties of the $P(E)$ function can be expressed.

1.1.4 Properties of the P(E) function

The $P(E)$ is usually interpreted as the probability for a tunneling Cooper pair to exchange the energy E with the environment, absorption for $E < 0$ and emission for $E > 0$. Indeed, from the equation (1.22), we can divide the expression of the current in two parts, the probability of tunneling of a Cooper pair to exchange the energy E and an attempt rate of Cooper hammering.

The $P(E)$ function has two main properties, its normalization (in agreement with the probability interpretation):

$$\int_{-\infty}^{\infty} \mathrm{d}E P(E) = 1 \tag{1.28}$$

and the detailed balance symmetry:

$$P(-E) = e^{-\beta E}P(E) \tag{1.29}$$

This can be understood as the probability of absorbing an energy E from the environment being directly linked to the presence of this energy E. For an energy $E > \beta$, the environment is in the ground state and this probability goes to zero.

In general, it is impossible to compute analytically the $P(E)$ function. From the numerical point of view, the computation of $P(E)$ through $J(t)$ (with the equations (1.19) and (1.21)) is complicated, as $J(t)$ is a slowly converging Fourier series and diverge for $t \to \infty$ if the environment has a purely ohmic component. The integral equation of Minnhagen, as described in [40], makes it possible to numerically evaluate $P(E)$.

1.2 Properties of typical electromagnetic environments

In order to understand more easily our devices, we will apply the presented theories to a representative example. Moreover, we will give here an approximated solution which will provide us a better understanding of their emission properties, it follows closely the explanation of [1] (see the appendices).

1.2.1 Typical electromagnetic environment

A typical device is constituted of a resonator at high frequency and a finite impedance at low frequency for voltage biasing. In figure 1.3 a), we show a possible lumped element schematics of a device. The sample can be divided in two parts, the components which are important at high frequency in gray and at low frequency in yellow. Notice that the low frequency part disappears at high frequency as the impedance of C_p is negligible at high frequency. Moreover, the dissipation at high frequency occurs through Z_0, this resistor models an infinite transmission line where emitted photons leak to a measurement apparatus.

The impedance seen from the junction can be numerically computed with a Spice-like simulator. All our electrical simulations are done with Qucs through a homemade python interface. The result are presented in figure 1.3 b).

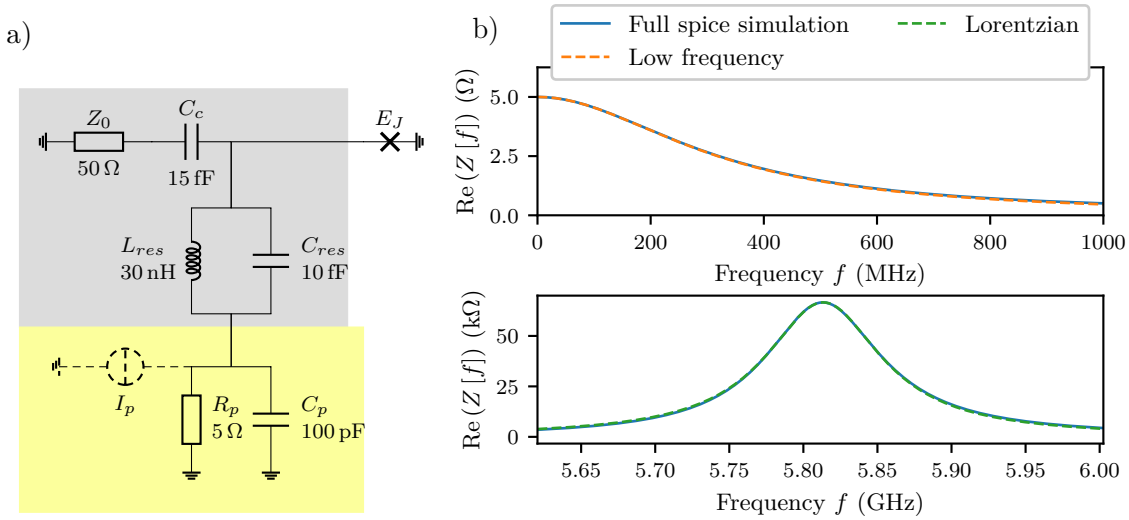

Figure 1.3: a) Electrical schematics implementing an impedance seen by the junction as in equation (1.30). This schematics can be broken in two parts, a high frequency resonator in gray and the polarization circuit in yellow, the biasing current source creating the necessary dc-bias voltage for the junction. As their working frequencies are very different, they appear separatively in the impedance. Notice that the parasitic capacitance of the Josephson junction can be absorbed in C_{res}. b) Impedance seen from the junction as a function of frequency. On top, the low frequency part is well approximated by an ohmic impedance with an f_p cut-off frequency. On the bottom, the high frequency impedance is well fitted with a Lorentzian.

To compute an approximated solution for $P(E)$ and therefore the photon emission rate density, we approximate the impedance with an ohmic part at low frequency (the voltage polarization circuit is described in section 4.2.2) and a peaked part which describes the resonator:

$$\frac{2\mathrm{Re}(Z[\omega])}{R_Q} = \frac{\rho}{1+\left(\frac{\omega}{\omega_R}\right)^2} + r\mathcal{L}[\omega,\omega_0,\gamma] \tag{1.30}$$

where $\mathcal{L}$ is a Lorentzian function:

$$\mathcal{L}[\omega, \omega_0, \gamma] = \frac{1}{\pi} \frac{\gamma\omega_0}{(\omega - \omega_0)^2 + \gamma^2} \tag{1.31}$$

The full simulation and the simple impedance (equation (1.30)) model agree very closely for frequencies of interest as presented in figure 1.3 b). The parameters from this adjustment are presented in table 1.1. From the electrical schematic, we can estimate the value of the model (approximated value given in table 1.1), see appendix A.3 for details. The approximated parameters are valid when:

$$\gamma \ll \omega_0 \tag{1.32}$$

This hypothesis corresponds to the existence of a strong resonance in the electromagnetic environment. Moreover, the existence of strong resonance means that its excitation is well-defined and matched the intuitive picture of photons.

Note that r is linked to the "classical" definition of the characteristic impedance Z_c of resonator:

$$\boxed{r = \frac{\pi Z_c}{R_Q}} \tag{1.33}$$

	Fitted value	Approximated value (expression)
Low frequency Cut-Off f_p	322 MHz	318 MHz ($\frac{1}{2\pi R_p C_p}$)
Resonance frequency f_0	5.813 GHz	5.812 GHz ($\frac{1}{2\pi\sqrt{L_{res}(C_{res}+C_c)}}$)
HWHM $\gamma/(2\pi)$	47.8 MHz	47.8 MHz ($\frac{Z_0 C_c^2}{4\pi L_{res}(C_{res}+C_c)^2}$)
Coupling ρ	Exact value: $\frac{2R_p}{R_Q} = 1.55 \times 10^{-3}$	
Coupling r	0.5329	0.5333 ($\frac{\pi}{R_Q}\sqrt{\frac{L_{res}}{C_{res}+C_c}}$)

Table 1.1: Parameters of the model in equation (1.30) describing the electrical schematics figure 1.3. The fitted values are obtained from a spice-simulation of the full circuit which is then fitted with the impedance equation (1.30). By considering the high frequency and low frequency part of the schematics, we can compute approximated parameters of the impedance which are very close to the result from the full circuit simulation, see appendix A.3 for details.

Experimentally, we only measure frequencies in a limited band and therefore, we focus on the emission at frequency $\omega \approx \omega_0$. Moreover, $\hbar\omega_0 \gg k_B T$ ($k_B T/h = 200$ MHz for $T = 10$ mK) for our devices, equation (1.27) can be simplified with the detailed balanced symmetry equation (1.29) for this specific impedance:

$$\gamma(V, \omega \approx \omega_0) = \frac{\pi^2 E_J^2}{\hbar\omega} r\mathcal{L}[\omega, \omega_0, \gamma] P(2eV - \hbar\omega) \tag{1.34}$$

We now need to estimate the function $P(2eV - \hbar\omega)$ for $\omega \approx \omega_0$. In section 1.1.4, we interpret the function $P(E)$ as the probability to exchange an energy E with the environment. Intuitively, this probability is big when the energy of the tunneling Cooper pair is equal to the energy of one or several resonant photons. Consequently, we only need to compute the function $P(E)$ for biasing voltage verifying $2eV - \hbar\omega \approx n\hbar\omega_0$ where n is an integer.

1.2.2 Approximated solution for P(E)

To compute approximately the $P(E)$ function, we use the Minnhagen equation where the ohmic part of the impedance is taken into account with the asymptotic behavior of $J(t \to \infty) = -\gamma_T t$ ($\gamma_T = \frac{\rho\pi}{\hbar\beta}$):

$$P(E) = \frac{\hbar}{E}\int_{\omega\approx\omega_0} \mathrm{d}\omega r\mathcal{L}[\omega, \omega_0, \gamma]P(E - \hbar\omega) + \frac{e^{-r}}{\pi\hbar}\frac{\gamma_T}{\gamma_T^2 + \left(\frac{E}{\hbar}\right)^2} \tag{1.35}$$

A derivation of this equation is given in appendix A.4.

From this equation, we can compute iteratively the function $P(E)$. Due to the detailed balanced symmetry, we can write:

$$P(E \approx 0) = P_0(E) = \frac{e^{-r}}{\pi\hbar}\frac{\gamma_T}{\gamma_T^2 + \left(\frac{E}{\hbar}\right)^2} \tag{1.36}$$

We can then compute:

$$P(E \approx \hbar\omega_0) = P_1(E) = \frac{\hbar}{E}\int_{-\infty}^{\infty} \mathrm{d}\omega r\mathcal{L}[\omega, \omega_0, \gamma]P_0(E-\hbar\omega) \approx \frac{re^{-r}}{\hbar\omega_0}\mathcal{L}\left[\frac{E}{\hbar}, \omega_0, \gamma + \gamma_T\right] \tag{1.37}$$

Finally, we can do the same to compute for all orders:

$$P_0(E) = \frac{e^{-r}}{\pi\hbar}\frac{\gamma_T}{\gamma_T^2 + \left(\frac{E}{\hbar}\right)^2} \quad \text{and} \quad P_{n\geqslant 1}(E) = \frac{r^n e^{-r}}{n(n!)}\frac{\mathcal{L}\left[\frac{E}{\hbar}, n\omega_0, n\gamma + \gamma_T\right]}{\hbar\omega_0} \tag{1.38}$$

To verify that this approximated computation of the $P(E)$ function is correct, we numerically compute it with [40] and we compare the approximated function $P_n(E)$ with equation (1.38). We show the result in figure 1.4, the approximation and the numerical computation match perfectly at this scale.

It is important to note that the good agreement at low frequency comes from the fact that $hf_p > k_B T$. Otherwise, the broadening of the $P(E)$ for $E \approx 0$ can be estimated by computing the Johnson–Nyquist voltage noise of the low frequency impedance.

1.2.3 Photon emission rate density

Using the approximation for $P(E)$ and equation (1.34), we can write an approximation for the photon emission rate density:

$$\gamma\left(V \approx k\frac{\hbar\omega_0}{2e}, \omega \approx \omega_0\right) = \frac{\pi^2 E_J^2}{\hbar\omega} r\mathcal{L}[\omega, \omega_0, \gamma]P_{k-1}(2eV - \hbar\omega) \tag{1.39}$$

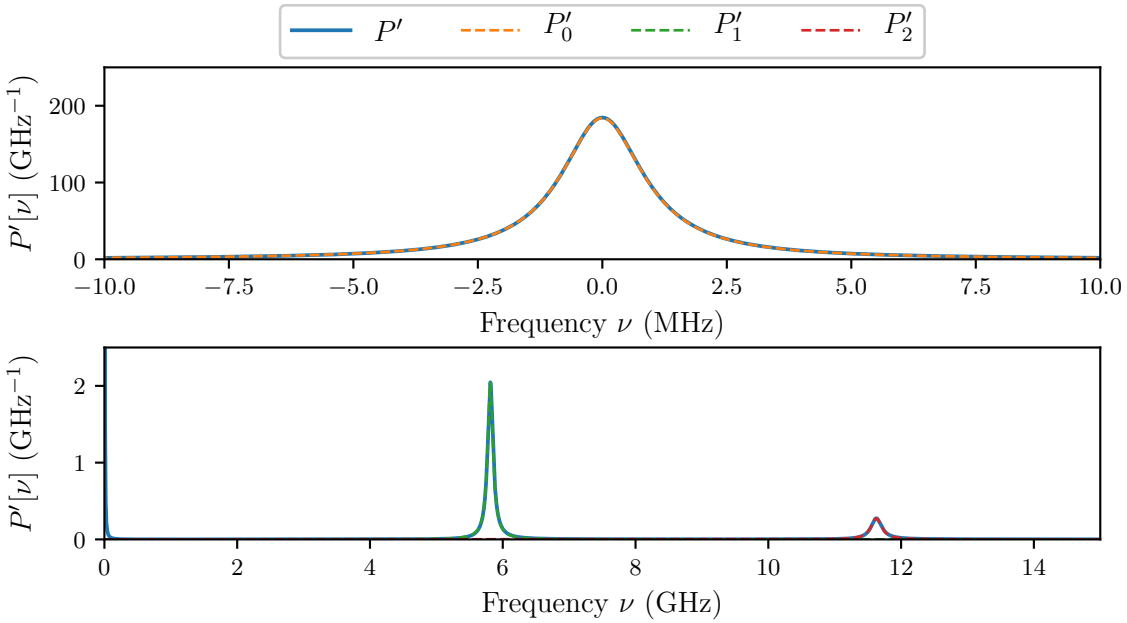

Figure 1.4: In blue, we represent $P'[\nu]$ as a function of frequency ν. We represent separately the low frequency (low energy) in top and the high frequency (high energy) in the bottom. $P'[\nu]$ is computed considering all orders and the full impedance [40]. The three other curves are computed using equation (1.38). The three approximated curves are indistinguishable from the full numerical computation at this scale. The temperature of the environment is 10 mK for all curves.

Therefore, we can easily compute the peak amplitude for the different orders:

$$\gamma\left(k\frac{\hbar\omega_0}{2e},\omega_0\right) = \frac{r^k e^{-r}}{(k-1)!}\frac{E_J^2}{\hbar\gamma\hbar((k-1)\gamma+\gamma_T)} \tag{1.40}$$

and the emitted power at the kth resonance is given by:

$$\Gamma_k = \int_{\omega\approx\omega_0} \mathrm{d}\omega\hbar\omega\gamma\left(k\frac{\hbar\omega_0}{2e},\omega_0\right) = \frac{\pi E_J^2\omega_0 e^{-r}}{\hbar}\frac{r^k}{(k-1)![k\gamma+\gamma_T]} \underset{\gamma\gg\gamma_T}{\approx} \frac{\pi E_J^2\omega_0 e^{-r}}{\hbar\gamma}\frac{r^k}{k!} \tag{1.41}$$

The main conclusion is that the amplitude of the process implying k photons scale with characteristic impedance $Z_C = rR_Q$ of a resonator as $r^k/(k!)$. Therefore, for small characteristic impedance ($r << 1$ or $Z_C << R_Q$), the simultaneous emission of several photons is much smaller than the emission of only one photon. Moreover, we can easily measure the characteristic impedance of a resonator by taking the ratio between the emitted power for the one photon process and the two-photon process: $\Gamma_2/\Gamma_1 = r/2 = \pi Z_c/(2R_Q)$.

We show in figure 1.5 the photon emission rate density and the total emitted power as a function of the biasing voltage (converted to frequency). On the photon emission rate density, we observe that the emission line at the lowest biasing voltage is very thin compared to the others. Indeed, it HWFM at fixed emission frequency is given by $\gamma_T = 2\pi R k_B T/(R_Q h) = 1$ MHz which is small at this scale. The emission line at higher voltage biasing are much wider, as their HWFM are given by $n\gamma + \gamma_T$.

The ratio $2\Gamma_2/\Gamma_1 = 0.497$ is in good agreement with $r = 0.533$, the difference come from the fact that γ_T is not infinitely smaller than γ. However this simple ratio allows us to obtain rapidly a good approximation of the characteristic impedance of a mode when the thermal noise of the biasing circuit is small.

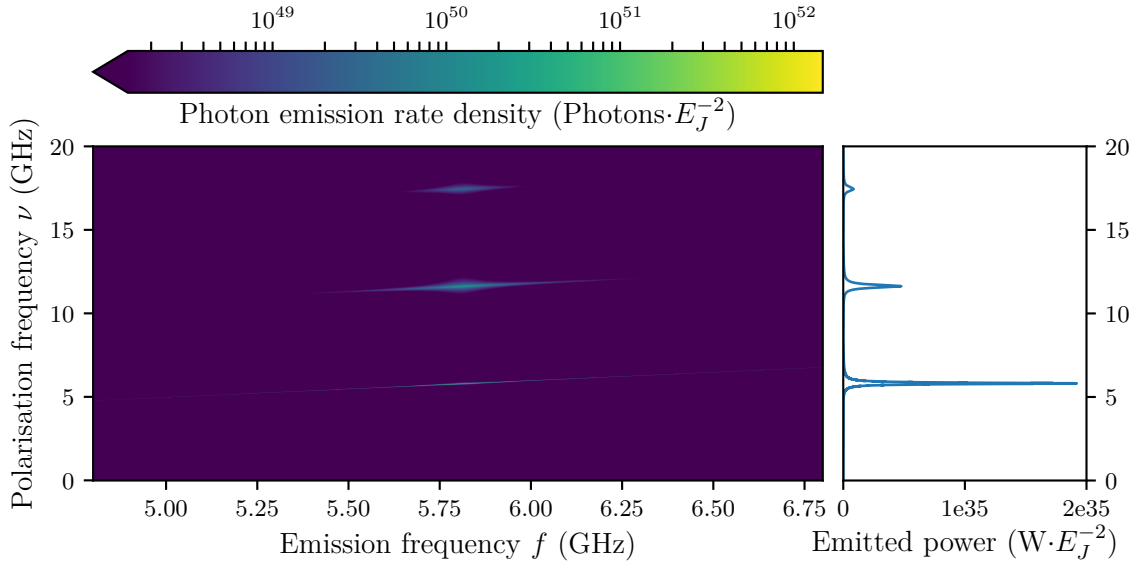

Figure 1.5: On the left, we show the photon-emission rate density as function of the frequency of emission f on the abscissa and the the bias-voltage on the ordinate. The bias-voltage is converted to frequency ($\nu = 2eV/h$). On the right, we represent the emitted power (computed with equation (1.41)) in the frequency range 3.8-7.8GHz ($\sim 40\gamma$) as a function the bias-voltage. Notice that the emission density and power are normalized by the Josephson energy, this explains the huge number as $E_J^2 = 1 \times 10^{-49}\,\mathrm{J}^{-2}$ for a critical current $I_c = 1\,\mathrm{nA}$.

1.2.4 Limits of the perturbation theory

The $P(E)$ description of the system is a perturbation theory, therefore it is only valid for specific parameters. The first limit is in the Josephson energy, indeed, we need $E_J P(E) \ll 1$ [16] to neglect higher order terms in E_J. For our typical electromagnetic environment, which was described in section 1.1.4, the function $P(E)$ is maximum for $E = 0$: $P(0) = \frac{1}{\rho k_B T}$. The perturbation theory is valid for:

$$E_J \ll \frac{2\mathrm{Re}(Z[0])}{R_Q} k_B T \tag{1.42}$$

If we do the computation for $Z[0] = R_p = 5\,\Omega$ and a temperature of 10 mK, $E_J \ll 1 \times 10^{-9}\,\mu\mathrm{eV}$ (or $I_C \ll 0.7\,\mathrm{pA}$). For our device, this condition is not verified as our critical current is in the nano-ampere range. Therefore, the photon emission is not well described for its first peak of emission.

Another consequence of the perturbative nature of $P(E)$ theory is that it only considers the conversion of the tunneling of a Cooper pair to the emission (or/and absorption) of

photons. Therefore, it does not describe the simultaneous tunneling of several Cooper pairs which can also emit photon. We will see that these phenomena can be experimentally observed, see section 5.1.3.2.

The second limit is in the environment state probability, we suppose that the electromagnetic environment is in thermal equilibrium. For the resonator point of view, it means that the photon leaks faster from the resonator than the Josephson junction generates them. The photon emission rate Γ_k must verify:

$$\Gamma_k \ll \gamma k \tag{1.43}$$

Another consequence of this hypothesis is the fact that the emission must not be correlated, the probability of emission must not depend on the state of the resonator. However, for environment with high characteristic impedance, we know that the photon emission becomes correlated, especially at low Josephson energy, (single photon emission for example [1]) and the quality of $P(E)$ approximation deteriorates.

1.3 Photo-multiplication

In the previous part, we have only considered the spontaneous emission in an environment near thermal equilibrium. In order to describe a phenomenon of photon multiplication, we need to model the impact of incoming photons in the system and to estimate what is elastically and inelastically scattered by it.

The electrical schematics of our photomultiplier is described in figure 1.6, it is constituted of two LC resonators which are coupled to a Josephson junction. Each resonator is capacitively coupled to a transmission line which can transport microwave excitations. We will consider the side a as the input of the system and the side b as the output of the system, therefore, we will only study the inelastic scattering from photons arriving through the side a to photons leaving trough the side b.

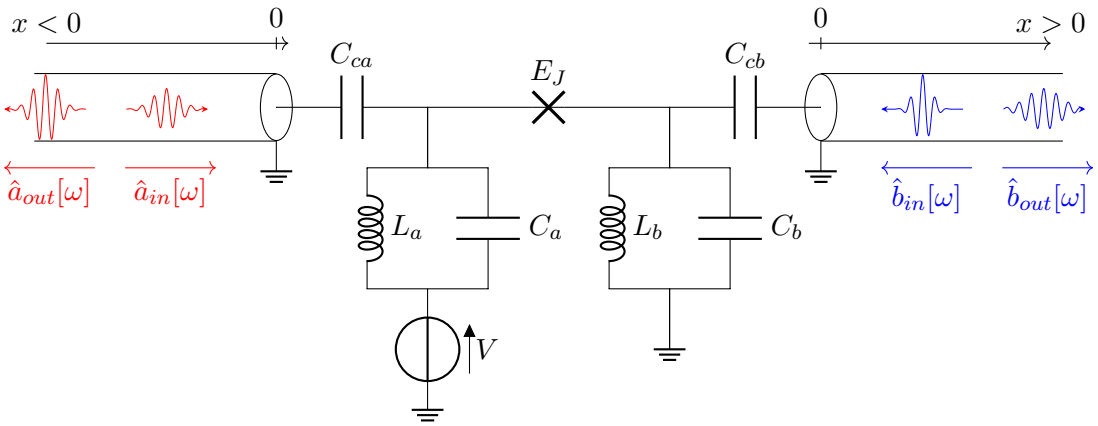

Figure 1.6: Electrical schematic for the considered photomultiplier. The two transmission lines are characterized with an impedance of Z_0 and a wave celerity of c_0. They allow for applying and extracting microwave radiation from the device.

To compute scattering of the microwave excitation, we will introduce the input-output theory. Then we will compute the effect of the coupling between the transmission line and the resonators. Finally, we will show the effect of the Josephson junction which couples the resonators. This theoretical approach was developed by Juha Leppäkangas. Here we will only introduce the elements required to understand the samples and measurements. We refer to [41] for more information.

1.3.1 Input-Output formalism

The input-output formalism is another way of treating dissipation in quantum mechanics. Instead of describing it through an infinite number of LC resonators, the energy is dissipated in transmission lines of infinite length. The main advantage of this description is to allow for modeling an input excitation (which puts the system out of equilibrium) on top of dissipation. Notice that it is possible with the Caldeira-Leggett model, if we consider a bath out of equilibrium.

The Hamiltonian of the input transmission line can be written [36, 42]:

$$\hat{H}_{TL,a} = \int_{-\infty}^{0} \mathrm{d}x \left[\frac{\hat{q}_{TL,a}(x,t)^2}{2C_0} + \frac{1}{2L_0} \left(\frac{\partial \hat{\phi}_{TL,a}}{\partial x}(x,t) \right)^2 \right] \tag{1.44}$$

where C_0 is the capacitance per unit length of the transmission line and L_0 is its inductance per unit length. The characteristic impedance Z_0 and the wave celerity c_0 are function of them: $Z_0 = \sqrt{L_0/C_0}$ and $c_0 = (\sqrt{L_0 C_0})^{-1}$.

The Hamiltonian can be solved in second quantization. For the flux, we obtain:

$$\hat{\phi}_{TL,a}(x<0,t) = \sqrt{\frac{\hbar Z_0}{4\pi}} \int_0^\infty \frac{\mathrm{d}\omega}{\sqrt{\omega}} \left[\hat{a}_{in}[\omega] e^{-\mathrm{i}\omega(t-x/c_0)} + \hat{a}_{out}[\omega] e^{-\mathrm{i}\omega(t+x/c_0)} + \text{h.c.} \right] \tag{1.45}$$

The operator $\hat{a}_{in}[\omega]$ annihilates an incoming photon[5]of pulsation ω, whereas $\hat{a}_{in}^\dagger[\omega]$ create an incoming photon. The operator $\hat{a}_{out}[\omega]$ and $\hat{a}_{out}^\dagger[\omega]$ perform the same operations for an outgoing photon.

As only pulsations near the pulsation of the input resonator ω_a couple to the resonator a, only states with such pulsation are important. We can approximate the field by:

$$\hat{\phi}_{TL,a}(x<0,t) = \sqrt{\frac{\hbar Z_0}{2\omega_a}} \left(\hat{a}_{in}\left(t - \frac{x}{c_0}\right) + \hat{a}_{out}\left(t + \frac{x}{c_0}\right) + \text{h.c.} \right) \tag{1.46}$$

where $\hat{a}_{in}(t)$ is the Fourier transform of $\hat{a}_{in}[\omega]$.

The charge in the transmission can be computed as:

$$\hat{q}_{TL,a}(x<0,t) = \sqrt{\frac{\hbar \omega_a}{2Z_0}} \left(\hat{a}_{in}\left(t - \frac{x}{c_0}\right) - \hat{a}_{out}\left(t + \frac{x}{c_0}\right) + \text{h.c.} \right) \tag{1.47}$$

Similar equations hold for the output side, the propagation direction is only inverted for the incoming and outgoing photons.

[5]This definition of a photon is not very satisfactory, as it is defined through a Fourier transform, a photon with a perfectly defined frequency has an infinite time extension. Other methods using time-frequency overcome this problem, as the definition through time windowed Fourier transform [38] or the use of wavelet [42] (appendix A.2).

1.3.2 Capacitive coupling and resonator

We consider the coupling between the transmission lines and resonators, we will focus ourself on the input resonator but the treatment is symmetrical for the output resonator. In order to write the Heisenberg equation of the resonator, we need to write the Hamiltonian of the system:

$$\hat{H}_a = \frac{\hat{q}_a^2}{2C_a} + \frac{\hat{\phi}_a^2}{2L_a} + \frac{\hat{q}_a \hat{q}_{TL,a}(x=0,t)}{C_a} + \frac{\hat{q}_{TL,a}(x=0,t)^2}{2C_s} + \hat{H}_{TL,a} \tag{1.48}$$

where $C_s^{-1} = C_{ca}^{-1} + C_a^{-1}$ and $\hat{H}_{TL,a}$ defined in the previous part.

To write the usual equation of motion for the input and output field, four steps are needed, see [41]. First, we write the charge and flux of the resonator in terms of their annihilation and creation operators, this is possible if the coupling is weak enough. Then we write the Heisenberg equation of motion for $\hat{\phi}_{TL,a}(x=0,t)$, we deduce the common boundary equation from it. The third step is to write the Hamiltonian using this boundary condition and to diagonalize it. This renormalizes the characteristic impedance and resonance frequency of the bare resonator. Finally, we write the equation of motion for the operator $\hat{\phi}_a$ and $\hat{q}_a$ and deduce the equations of motion for annihilation (and creation) operator. After a change of variable, we obtain the usual equations:

$$\dot{\hat{a}}(t) = -\mathrm{i}\omega_a \hat{a}(t) - \frac{\gamma_a}{2}\hat{a}(t) + \sqrt{\gamma_a}\hat{a}_{in}(t) \tag{1.49}$$

with the boundary condition:

$$\hat{a}_{in}(t) + \hat{a}_{out}(t) = \sqrt{\gamma_a}\hat{a}(t) \tag{1.50}$$

where $\gamma_a = \frac{Z_0 C_{ca}^2}{2L_a(C_a+C_{ca})^2}$ and $\omega_a = \frac{1}{\sqrt{L_a(C_a+C_{ca})}}$.

Notice that a minor error is presented in the article [41]. In page 15, the effective capacitance C_p is not equal to $C_a + C_s$ but to $C_a + C_{ca}$[6]. None of the conclusions are affected by this change as all formulas are expressed in term of characteristic impedances, resonance pulsations and energy decay rates.

These equations can easily be solved by taking the Fourier transform of equations (1.49) and (1.50):

$$\hat{a}_{out}[\omega] = \frac{A^*[\omega]}{A[\omega]}\hat{a}_{in}[\omega] \quad \text{with} \quad A[\omega] = \frac{\gamma_a}{2} + \mathrm{i}(\omega_a - \omega) \tag{1.51}$$

which correspond to the classical scattering of an LC resonator capacitively coupled to a transmission line.

[6] To obtain a quadratic Hamiltonian from the formula (A24), we need to solve (notation from the article [41]):

$$\frac{Z_{LC}}{4L_a} - \frac{1}{4C_a Z_{LC}} + \frac{C_s}{C_a}\frac{1}{4Z_{LC}} = 0$$

The error comes probably from a sign inversion of the last term of this equation, which gives rise to the incorrect formula.

1.3.3 Junction

It is now time to consider the coupling between the two resonators through the Josephson junction. As described in section 1.1.2, the Hamiltonian of the Josephson junction can be written:

$$\boxed{\begin{aligned}\hat{H}_J &= -E_J \cos\left(\omega_J t + \frac{\hat{\phi}_a}{\hat{\Phi}_0} - \frac{\hat{\phi}_b}{\hat{\Phi}_0}\right) \\ &= -E_J \cos\left(\omega_J t + g_a\left[\hat{a} + \hat{a}^\dagger\right] - g_b\left[\hat{b} + \hat{b}^\dagger\right]\right)\end{aligned}} \tag{1.52}$$

where $g_a = \sqrt{\pi Z_a / R_Q}$ with $Z_a = \sqrt{L_a/(C_a + C_{ca})}$ and similarly for g_b.

The Heisenberg equations of motion then take the form:

$$\begin{cases}\dot{\hat{a}}(t) = -\mathrm{i}\omega_a \hat{a}(t) + \dfrac{\mathrm{i}}{\hbar}\left[\hat{H}_J, \hat{a}(t)\right] - \dfrac{\gamma_a}{2}\hat{a}(t) + \sqrt{\gamma_a}\hat{a}_{in}(t) \\ \dot{\hat{b}}(t) = -\mathrm{i}\omega_b \hat{b}(t) + \dfrac{\mathrm{i}}{\hbar}\left[\hat{H}_J, \hat{b}(t)\right] - \dfrac{\gamma_b}{2}\hat{b}(t) + \sqrt{\gamma_b}\hat{b}_{in}(t)\end{cases} \tag{1.53}$$

The boundary conditions are not modified, see equation (1.50).

The equation (1.52) is too complicated to solve equation (1.53) analytically. However, we are only interested in specific cases: when a single photon with a pulsation ω_a is converted to n photons at ω_b. Therefore, we will only consider bias voltages near the resonance $\omega_J \approx n\omega_b - \omega_a$. Moreover, we only consider input radiation comprised of single-photons near the frequency of the input resonator: $\omega_{in} \approx \omega_a$. In these conditions, the junction Hamiltonian (equation (1.52)) can be written in the rotating wave approximation (RWA):

$$\hat{H}_J = \hbar\eta_n \hat{a}(t)\left(\hat{b}^\dagger(t)\right)^n e^{-\mathrm{i}\omega_J t} + \text{h.c.} \quad \text{where} \quad \eta_n = \frac{E_J}{2\hbar}\frac{\mathrm{i}^{n+1}}{n!} g_a g_b^n \exp\left(-\frac{g_a^2}{2} - \frac{g_b^2}{2}\right) \tag{1.54}$$

1.3.4 Single photon multiplication by a factor n

We will start to computing the probability of transmission for a linear conversion $n = 1$ and will explain how it can be extended for an arbitrary multiplication factor n. This computation does not evaluate frequency-frequency correlations, a more complete approach is presented in [41] which addresses this limitation.

1.3.4.1 Solution for $n = 1$

We can write in Fourier space the equation (1.53) in the RWA:

$$\begin{cases}A[\omega]\hat{a}[\omega] = -\mathrm{i}\eta_1^* \hat{b}[\omega + \omega_J] + \sqrt{\gamma_a}\hat{a}_{in}[\omega] \\ B[\omega]\hat{b}[\omega] = -\mathrm{i}\eta_1 \hat{a}[\omega - \omega_J] + \sqrt{\gamma_b}\hat{b}_{in}[\omega]\end{cases} \tag{1.55}$$

Using the boundary condition (equation (1.50)), we can write the output field as a function of input field thanks to several hypotheses. First, no photon arrives from side b (only quantum fluctuation). This is possible since the frequency of the output mode is high compared to thermal fluctuation and no microwave radiation is applied from this side. Secondly, we do not consider low frequency fluctuations of the bias voltage, as is done in

the $P(E)$ theory, an incoming photon at ω is convert to a photon at $\omega+\omega_J$ exactly (ω_J is negative for a down-conversion). The output field can be expressed as:

$$N_{out} = \left\langle \hat{b}^\dagger_{out}[\omega+\omega_J]\hat{b}_{out}[\omega+\omega_J] \right\rangle = \frac{\gamma_a\gamma_b|\eta_1|^2}{\left||\eta_1|^2 + A[\omega]B[\omega+\omega_J]\right|^2}\left\langle \hat{a}^\dagger_{in}[\omega]\hat{a}_{in}[\omega] \right\rangle \tag{1.56}$$

We can then deduce the conversion probability of an incoming photon at ω:

$$T_{n=1} = \frac{1}{n}\frac{\left\langle \hat{b}^\dagger_{out}[\omega+\omega_J]\hat{b}_{out}[\omega+\omega_J] \right\rangle}{\left\langle \hat{a}^\dagger_{in}[\omega]\hat{a}_{in}[\omega] \right\rangle} = \frac{\gamma_a\gamma_b|\eta_1|^2}{\left||\eta_1|^2 + A[\omega]B[\omega+\omega_J]\right|^2} \tag{1.57}$$

1.3.4.2 Extension to any n

To generalize this expression to an arbitrary n, we map the resonators to two-level systems. We consider a biasing voltage which is resonant for a photon multiplication by a factor n. When a n photon state is produced in the output resonator, two possibilities exist, this state is converted back to one photon inside the input resonator or a photon leaks to the output transmission line. In that case, all photons will necessarily leak to the output transmission line as the biasing voltage is not resonant for the process where $(n-1)$ output photon is back converted to one input photon.

The output resonator acts as a two-state system, 0-photon or n-photons. The effective decay rate of the exited state is renormalized by a factor n: $n\gamma_b$ (similarly the resonance frequency becomes $n\omega_b$) and the effective coupling becomes $\eta_n\sqrt{n!}$. The conversion probability can then be expressed as:

$$T_n = \frac{\gamma_a n\gamma_b(n!)|\eta_n|^2}{\left|(n!)|\eta_n|^2 + A[\omega]B_n[\omega+\omega_J]\right|^2} \quad \text{where} \quad B_n[\omega] = \frac{n\gamma_b}{2} + \mathrm{i}(n\omega_b - \omega). \tag{1.58}$$

For more simplicity, we express it with a normalized coupling:

$$\boxed{T_n[\omega,\omega_J] = \frac{4|\varepsilon_n|^2}{\left||\varepsilon_n|^2 + \frac{4A[\omega]B_n[\omega+\omega_J]}{\gamma_a n\gamma_b}\right|^2}} \quad \text{where} \quad \varepsilon_n = 2\eta_n\sqrt{\frac{n!}{\gamma_a n\gamma_b}} \tag{1.59}$$

This equation is rather complex as it depends on a lot of parameters: E_J, g_a, γ_a, g_b, γ_b and ω_a. To get a better understanding of their impact on the photon multiplication effect, we will discuss first the implication of this equation, then we will discuss the limits of this approach.

1.3.5 Properties of the conversion probability

The main conclusion we can extract from the equation (1.59) is the possibility of a perfect photon multiplication. If we place ourself at the resonance $\omega=\omega_a$ and $n\omega_b = \omega_J+\omega_a$, this equation is reduced to:

$$T_n = \frac{4|\varepsilon_n|^2}{\left||\varepsilon_n|^2 + 1\right|^2} \tag{1.60}$$

Therefore, we obtain a perfect photon multiplication, $T_n = 1$, when $|\varepsilon_n| = 1$.

Instead of a unique Josephson junction, we use a Superconducting QUantum Interference Device (SQUID) to be able to tune the Josephson energy. This energy can then be adjusted during the experiment whereas the other parameters are fixed by the geometry of the sample. This is why we express the Josephson energy as a function of them in order to estimate the characteristic of our SQUID:

$$E_J = \hbar \frac{\sqrt{\gamma_a \gamma_b}}{g_a g_b^n} \frac{n!}{\sqrt{(n-1)!}} \exp\left(\frac{g_a^2}{2} + \frac{g_b^2}{2}\right) \tag{1.61}$$

Another important property is the bandwidth of the photon multiplication processes. To express it, we consider incoming photon with a pulsation $\omega = \omega_a + \delta\omega$ and corresponding outgoing photons with a resonant biasing voltage $n\omega_b = \omega_J + \omega_a$, which gives us $\omega + \omega_J = n\omega_b + \delta\omega$. In that case the conversion probability takes the form:

$$T_n = \frac{4|\varepsilon_n|^2}{\left(1 + |\varepsilon_n|^2 - 4\frac{\delta\omega^2}{\gamma_a n \gamma_b}\right)^2 + 4\left(\frac{\delta\omega(\gamma_a + n\gamma_b)}{\gamma_a n \gamma_b}\right)^2} \tag{1.62}$$

To better understand that expression, we plot it in figure 1.7 for $n = 1$ for different γ_a and γ_b. It is important to note that the case $\gamma_a = 2\gamma_b$ is equivalent to considering the photon multiplication by a factor $n = 2$ when $\gamma_a = \gamma_b$.

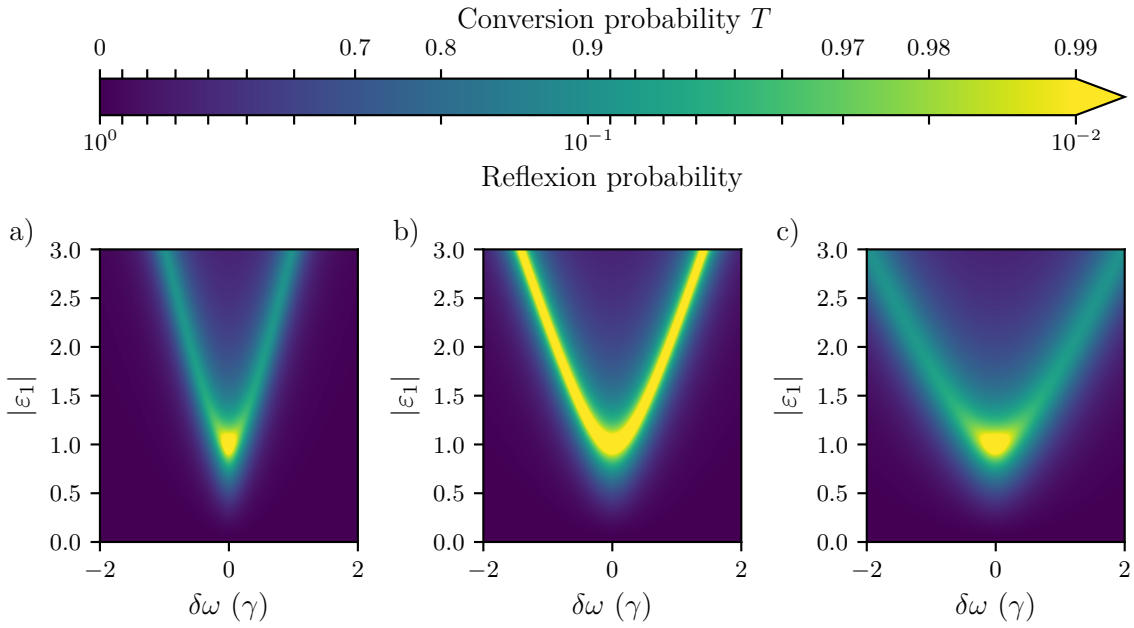

Figure 1.7: Conversion probability as a function of the input microwave detuning and of the adimensional coupling ε_1. We plot the curve for a) $\gamma_a/2 = \gamma_b = \gamma$, b) $\gamma_a = \gamma_b = \gamma$ and c) $\gamma_a = 2\gamma_b = \gamma$

For $\gamma_a = \gamma_b$ for $n = 1$ or $\gamma_a = n\gamma_b$ for an arbitrary n, we observe that a perfect transmission is possible when $|\varepsilon_1| > 1$ with a splitting of the conversion peaks. When $\gamma_b > \gamma_a$, the area of high efficiency conversion (T > 0.99) decreases, however, the HWFM increases. On the contrary, we observe a contraction of all structure when $\gamma_a > \gamma_b$.

To conclude on the bandwidth of the photon multiplication effect, the choice of the resonator bandwidths depends on the goal. If we want to maximize the bandwidth of detection, the output resonator need to have a much larger bandwidth than the input. If you want to maximize the area where $T > 0.99$, we need to verify $\gamma_a = n\gamma_b$ for the wanted photon multiplication.

Finally, we can write the conversion probability with a bias voltage offset $\delta\omega_J$ at the resonance $\omega = \omega_a$, $n\omega_b = \omega_J + \omega_a$ and $|\varepsilon|_n = 1$:

$$T_n = \frac{1}{1 + \left(\frac{\delta\omega_J}{n\gamma_b}\right)^2} \tag{1.63}$$

We recognize a Lorentzian with a HWFM of $n\gamma_b$. This can be easily understood as the offset voltage is distributed over all output photons and its impact decreases when the number of photon increases (each of them are closer to the resonance).

Until now, we have only considered the impact of E_J, γ_a and γ_b. The effect of the characteristic impedance has only a renormalization effect on the coupling constant and the resonance frequencies modify the biasing voltage to observe the photon-multiplication. However, these parameters have strong impact when the incoming field is constituted with multi-photon state which is not account for in this approach. Moreover, this linear scattering approach does not allow to compute the full frequency correlation output field.

1.3.6 Beyond the linearized approach

The linearized approach has two main limitations, first we only compute the conversion probability and cannot determine the output state for a given input state. Secondly, it is only valid for a single input photon, i.e. we cannot evaluate the dynamical range of the photon multiplication effect. These two limitations are treated in [41] and we repeat here the conclusion for completeness.

From the frequency-frequency correlation of the field, we can deduce the first and second order correlation functions, and we can show that the conversion is coherent. An input field made of the superposition of a single photon state and vacuum, $|\text{in}\rangle = c_0 |0\rangle_{\text{in}} + c_1 |1\rangle_{\text{in}}$, is converted (at the resonance) to an output state with a superposition of n-photon state and vacuum, $|\text{out}\rangle = c_0 |0\rangle_{\text{out}} + \text{i}^n c_1 |n\rangle_{\text{out}}$. It is important to note that the phase of the input photon is transferred to the ensemble of output photons.

The second question is a bit more complicated to treat as the equation (1.54) of the RWA must be modified to take into account the non-linear interaction between multi-photon states inside the resonators. Using this modified Josephson Hamiltonian and a coherent driving Hamiltonian, a Lindblad-type master equation is deduced and numerically solved to obtain the conversion probability.

We show in figure 1.8 the conversion probability as a function of the resonator bandwidth and the average input photon number of a coherent pulse drive. Two cases are presented, $g_a = g_b = 1$ and $g_a = 0.25$, $g_b = \sqrt{2}$. We observe that decreasing the characteristic impedance of the input resonator increases the dynamical range of the photo-multiplier. This comes from the decrease of the non-linearity due to the reduced characteristic impedance which limits the interaction of the photons inside the input resonator.

Secondly, an increase in the bandwidth of the resonator increases the dynamical range, simply because the average photon population is lower inside the resonators.

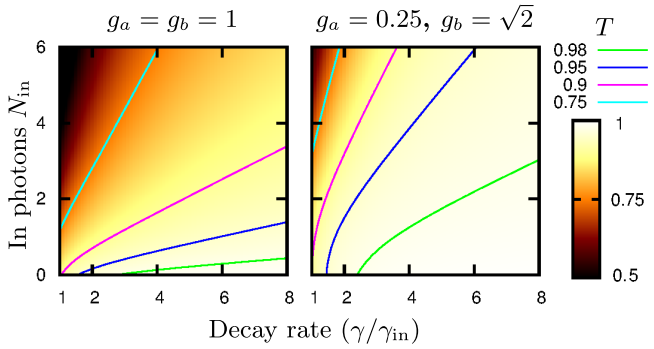

Figure 1.8: Average conversion probability for coherent-state pulse with a HWFM $\gamma_{in}/2$ as a function of the HWFM of the resonators, $\gamma_a = \gamma_b = \gamma$ and its input photon number N_{in}. The system is biased at the photon-tripling resonance ($n = 3$, $|\varepsilon_3| = 1$). This figure is extracted from [41] (FIG. 4, page 7).

The last phenomenon to discuss is the spontaneous emission which may conceal the wanted photon multiplication processes. This problem is treated with the $P(E)$ theory in [41], however we will see experimentally in chapter 5 that this theory is not valid for the Josephson energy needed for an efficient photon multiplication in our case. Therefore, we only give general guidelines on minimizing this parasitic effect.

The frequency of the input and output resonators must be carefully chosen, the biasing voltage for a given n must be far from the fundamental emission line of the bare system. To say it mathematically, for a biasing voltage: $\omega_J = n\omega_b - \omega_a$, $\omega_a \neq \omega_J/p,\ \forall p \in \mathbb{N}$ and $\omega_b \neq \omega_J/k,\ \forall k \in \mathbb{N}$. This effect is worst for the input resonator, as a spontaneous emission inside it is photo-multiplied to the output resonators.

The second optimization we need to work on is the characteristic impedance of the output resonator. Indeed, the Josephson energy increases when the impedance decreases, as described by equation (1.61), which intensifies rapidly the spontaneous emission of the device. The output resonator must therefore possess a characteristic impedance as high as possible.

Conclusion

We have first described the spontaneous emission of a resonator coupled to a voltage-biased Josephson junction through a perturbation theory. We have then applied this theory to a typical system in order to explain what can be expected from an actual device and how we can extract parameters from the measured photon emission rate. Finally, we have presented the key elements for designing a photo-multiplier based on inelastic Cooper pairs tunneling using input/output theory in a rotating wave approximation.

Chapter 2

Device fabrication

Contents

The usual nano-fabrication process for superconducting quantum circuits is based on aluminum. The main reason is the coexistence of a superconducting state and the well-known formation of a high quality oxide which allows fabricating SIS Josephson junctions, the principal building block for creating non-linear superconducting elements. Moreover, the fabrication process is often based on lift-off and double angle shadow evaporation which is possible because of the high vapor pressure at relatively low temperature of aluminum, so the resist is not burnt. Therefore, aluminum appears to be the ideal material to fabricate our sample, but it possesses several drawbacks. The limited critical temperature (1.2 K) of aluminum prevents tests in liquid helium and its gap limits the working frequency of the circuits to approximately a hundred gigahertz. Moreover, this limited gap increases the parasitic capacitance of the junction at a given Josephson energy compared to materials with higher critical temperature.

To overcome these drawbacks and to allow for the fabrication of complex devices, another fabrication process is presented in this chapter. We will first present what was previously done in the group, then the current fabrication process will be explained. Finally, we will present the possibilities opened up by this process.

2.1 Previous fabrication process

The group has developed for during several years a process [43–45] based on NbN-MgO-NbN junction. There are several advantages, first the high critical temperature of 16 K allows working frequency up to 1.2 THz. Then, a thin film of NbN has a high kinetic inductance, which makes it possible to create resonators with high characteristic impedance. As explained in the Chapter 1, this increases the amplitude of multiphoton processes and is essential to observe the photon multiplication effect.

This advantage is also its main drawback, because kinetic inductance is very sensitive to the fabrication condition and processing. Indeed, its kinetic inductance is linked to its disorder which can be easily modified during the fabrication. Moreover, the growth of NbN creates rough surfaces which increase the parasitic capacitance of the junction. A previous generation of photo-multiplier (developed by Dibyendu Hazra) was inoperative because of uncontrolled frequency shifts due to these two reasons. Another difficulty was the chemical hardness of NbN which calls for hard solid masks in order to be correctly defined by reactive ion etching.

Because of these problems, we have chosen to switch to a very similar process based on Nb-Al/Al_2O_3-Nb junctions. The main advantage is the wide literature on these junctions as they are commonly used for various applications (single flux quantum logic [46], radio-astronomy mixers [47], Josephson voltage standard [48]...) and are commercially available [49]. Moreover, the arrival of a new sputtering machine allows us to control the oxidation of aluminum, which was impossible in the previous tools.

2.2 Fabrication process

The fabrication is performed on 100 mm wafers with a mix of electron beam and optical lithography, so that 69 different chips can be made at the same time. We can note here that we have structures with very different size, from 100 nm for the junction to millimeter size for transmission lines, which is why we perform a mix of optical and electron-beam lithography.

The samples are fabricated on top of 530 µm thick sapphire wafers because of their microwave properties, notably low loss, and the high resistance to etching. The dielectric constant of sapphire is anisotropic (ε_r=11.5 parallel to C-axis, ε_r=9.3 perpendicular to C-axis), which is why we choose a wafer cut parallel to the C-plane (orthogonal to the C-axis), so the apparent ε_r is isotropic in this plane.

2.2.1 Trilayer preparation

The first step of the fabrication is to deposit a trilayer which is used for the vertical junction and the base wiring. Every layer of this first step is deposited using a Plassys sputtering system. To get a good reproducibility of this step, it is dedicated to the deposition of superconductors (niobium, aluminum or titanium) with dc-sputtering and insulators (magnesium oxide or silicon oxide) with rf-sputtering in high vacuum, the base pressure is below 2.0×10^{-7} Pa. The system makes it possible to perform co-sputtering with argon and nitrogen atmosphere which allow depositing a wide range of materials. Moreover, we can

perform controlled oxidation inside the loading chamber and clean with argon plasma inside the high vacuum chamber.

The first fabrication step is to clean the wafer with an argon plasma during 10 min. We then deposit first 50 nm of niobium, then 7 nm of aluminum, this thickness allows to fully cover and smooth the niobium surface [50] to have reproducible junction and is thin enough to be easily etched. The aluminum is next statically oxidized during 10 min with a pressure varying between 50 Pa and 5000 Pa to change the tunnel barrier thickness. Finally, we deposit 50 nm of niobium. The precise parameters for the deposition are resumed in table 2.1.

Materials	Thickness (Time)	Pressure	Argon flow	Current or Power
Niobium	50 nm (41 s) 270 nm (221 s)	0.8 Pa	70 Sccm	2 A (Dc sputtering)
Aluminum	7 nm (7 s)	0.8 Pa	70 Sccm	1 A (Dc sputtering)
Magnesium oxide	10 nm (300 s)	1 Pa	70 Sccm	200 W (RF sputerring)

Table 2.1: Sputtering recipes for the Plassys MP45045. All depositions are performed at ambient temperature (21 °C) and we pump the chamber to a pressure of 5.0×10^{-6} Pa between each deposition.

To finish the preparation of the wafer, alignment crosses are defined with electron-beam lithograph, using a JBX-6300FS from JEOL, with a PMMA resist (see the table 2.2 for the recipes). We deposit by electron-beam evaporation 10 nm of chromium then 60 nm of platinum inside a MEB550 from Plassys. We perform a standard lift-off with a night in acetone followed up with 5 min in an ultrasonic bath and rinse with isopropyl alcohol (IPA) for 2 min

Resist	Thickness	Pre-exposure bake	Exposition	Developing
LOR_A	100 nm	150 °C, 600 s	not photosensitive	AZ 326MIF
UV5[1]	450 nm	130 °C, 60 s	240 nm at 40 W/m^2, 1.3 s	AZ 326MIF, 30 s
AZ1512HS	1.2 µm	100 °C, 60 s	365 nm at 60 W/m^2, 25 s	AZ Developer diluted 1:1 in H_2O, 30 s
PMMA[2]	270 nm	180 °C, 300 s	100 kV at 13 C/m^2 with 1 nA beam	MIBK:IPA at 1:3, 45 s

Table 2.2: Lithography recipes of the resists used.

2.2.2 Trilayer definition

We shape the trilayer in three steps. We first transfer an optical mask to an aluminum mask, then we perform an electron beam lithography to finish the definition of the aluminum mask. Finally, we perform an inductively coupled plasma etching to transfer the mask to the trilayer.

For the optical part, we begin by spin coating a layer of LOR_A, bake the resist, then spin coat a layer of UV5 and perform the pre-exposure bake, see the table 2.2 for the recipes. This bilayer is insulated with an MJB4 from SUSS MicroTec, baked to activate the resist and developed. The LOR_A resist is not photosensitive but it dissolved isotropically and rapidly in the TMAH developer, so it dissolves under the UV5 resist as we can see in the figure 2.1 a), creating an undercut. It prevents the 70 nm aluminum, which is then deposited by evaporation, on top of the UV5 to directly connect with the aluminum on top of the niobium. In consequence, we are able to easily lift the aluminum with the same method as in part 2.2.1. The LOR_A is not soluble in acetone, so we arrive at the state of the figure 2.1 b). To remove it, we perform a dry etching using an inductively coupled plasma (ICP) etching system, PlasmPro 100 from Oxford, with an O_2 plasma, details on the recipe are given in Table B.1. Notice that all the dry etches are performed using this ICP etching system. The wafer then looks like in figure 2.1 c).

We then define the small structures using an electron beam lithography with a PMMA resist and perform a lift off of 70 nm of aluminum. We obtain the structure depicted in figure 2.2. The electron beam lithography is mandatory as we need small junctions with low parasitic capacitance in order to limit the hybridization of the mode at each side of the junction.

To transfer the mask to the trilayer, we start by etching the upper niobium layer with the Nb etching recipe of the Table B.1. We use a laser monitoring to stop on top of the oxidized aluminum. We then perform an overetch with a high plasma pressure to clean the border of the niobium (Nb overetch in the Table B.1). To etch the aluminum of the junction we use an argon plasma, we choose to use a mechanical etch instead of a chemical one (using BCl_3 with HBr for example) because the etching is slower. So we control more easily the depth of the etching which limits the degradation of the mask, which is also in aluminum but thicker. Moreover, we take out the wafer of the ICP system before the next step in order to form now aluminum oxide top of the mask, which hardens it. Finally, we etch the niobium of the bottom of the trilayer by repeating the step for the top one. We obtain relatively vertical flanks as we can see in figure 2.2 d). We do not remove the aluminum mask at this step as this would also attack the aluminum of the junction.

2.2.3 Chromium resistors

The next step is to perform a lift-off of chromium to create resistors, which are useful to create on-chip dissipation as for amplifiers. We perform an optical lithography over an AZ1512 HS resist then evaporate 200 nm of chromium. We lift the chromium by using acetone for 1 h then 5 min inside an ultrasonic bath and rinse with isopropyl alcohol.

[1] UV5 is an activated resist which needs a post exposure bake at 300 °C for 90 s.

[2] PMMA 950K diluted at 4% in etyhl lactate. After the developing, the resist is rinsed in IPA for 30 s.

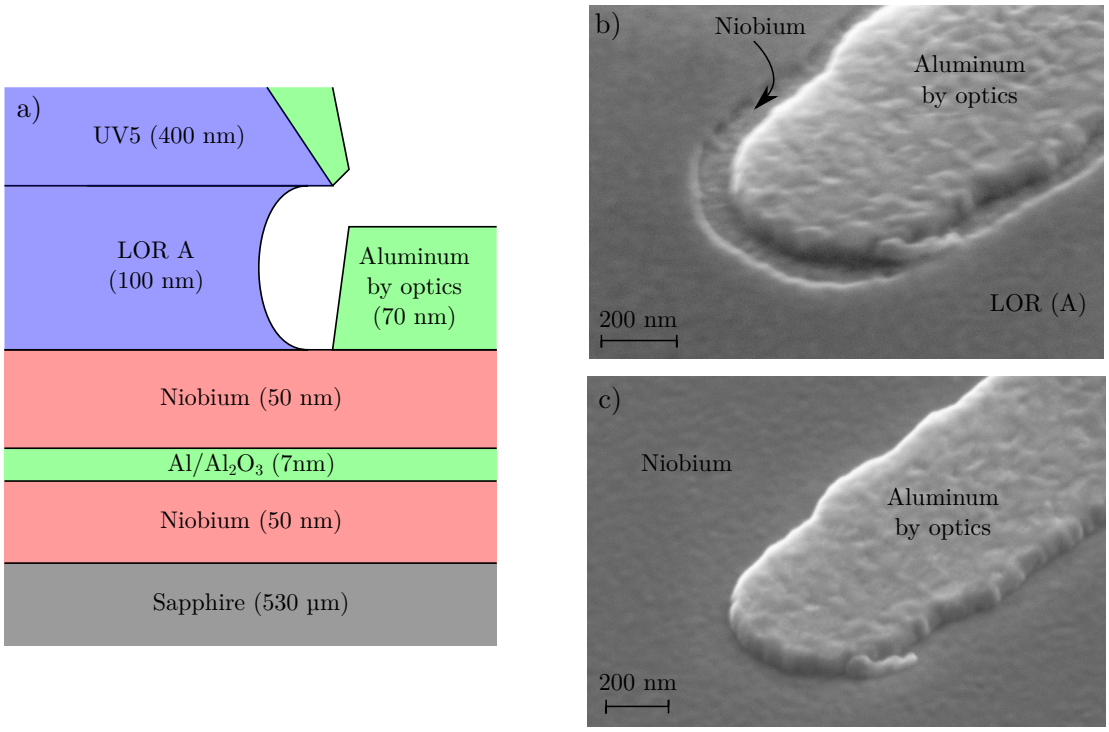

Figure 2.1: a) Representation of the trilayer structure with the optical stack before lift off of the aluminum. Note, theses schematics are not to scale as this would create difficulty to show the critical elements of the fabrication. b) Scanning electron microscopy (SEM) image after the lift-off of the aluminum, we observe the undercut of the LOR resist compared to the aluminum mask. c) SEM image after the O_2 etching of the LOR. The surface is cleaned of every residue.

2.2.4 Dielectric for spacers and bridges

After the chromium resistance deposition, we deposit 200 nm of Si_3N_4 using plasma enhanced chemical vapor deposition (PECVD) in a system from Corial (D250L). We exploit the isotropic growth of this method to obtain a higher thickness near the edges of the trilayer compared to flat areas. We then sputter 10 nm of magnesium oxide as an etching-stop layer for the following steps. We then perform an optical lithography with AZ1512 HS resist and develop it. To obtain the result of figure 2.3 a), we etch the MgO using acetic acid at 1% in volume during 12 s.

We perform a directional dry etch using the same ICP etching system (for the recipe, see Si_3N_4 in Table B.1). With this etch, we create spacers which isolate the sidewalls the trilayer, as represented in figure 2.3 b). At this stage, we can etch the aluminum of the first masks in all uncovered areas as the aluminum of the junction is protected by the silicon nitride spacer. We perform this etch using AZ 326 MIF (2.38 % TMAH in water) for around 2 min. The last step is to remove the resist with acetone and its residue with O_2 plasma. At this stage, we can observe the spacer in figure 2.3 c). Moreover, we are able to create vias through the dielectric which will allow us to cross wires or to create parallel

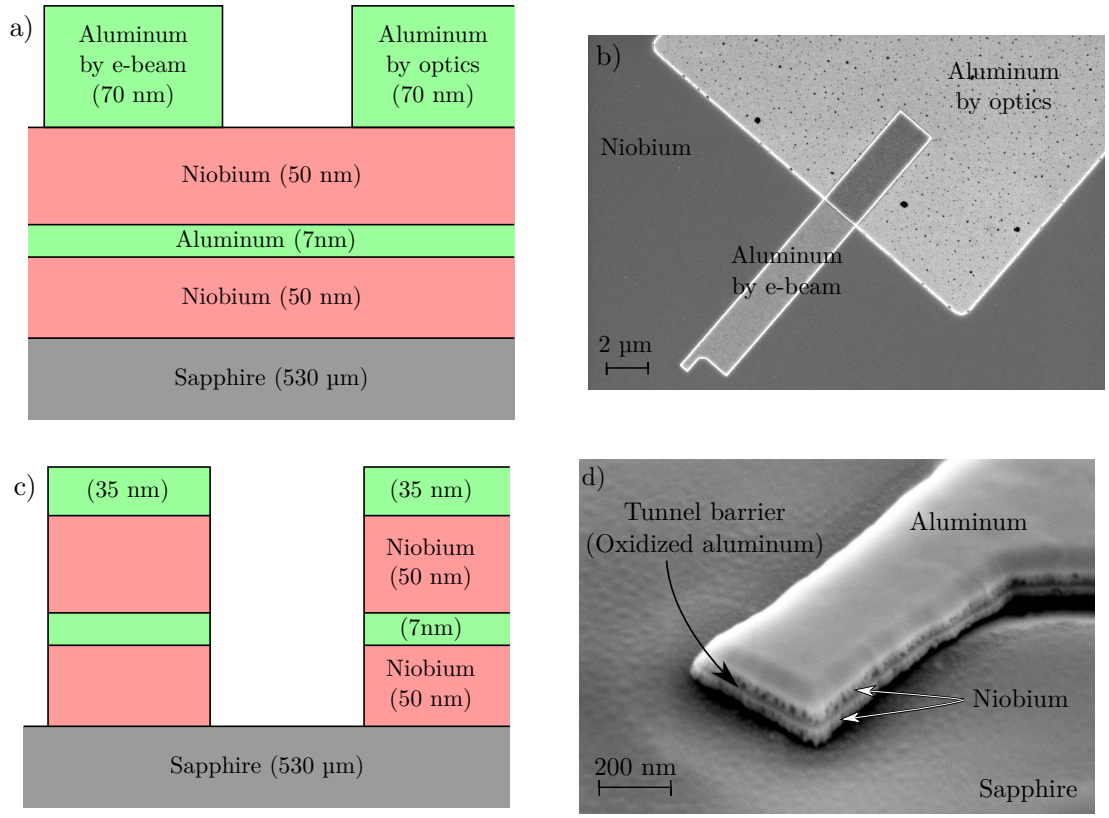

Figure 2.2: a) Schematics of the layer structure after definition of the electron beam aluminum mask. b) SEM picture showing the link between the structure defined by optical and electron beam lithography. c) Structure after etching of the trilayer, the aluminum of the mask is partialy consumed during the etching. d) SEM images of a trilayer, we can observe that the layered structure is quite vertical with a small step at the oxidized aluminum level.

plate capacitor, as we can observe in figure 2.3 d). We can remark on this figure that the silicon nitride is etched nearly everywhere on the wafer to prevent inhomogeneities due to loading during the etching.

2.2.5 Counter-electrode fabrication

We perform an argon plasma cleaning inside the vacuum chamber for 5 min in order to eliminate the niobium oxide formed because of exposition to the atmosphere. Then 270 nm of niobium is sputtered and an aluminum mask is defined using the exact same step than in part 2.2.2. The layers at this stage of the process are represented in figure 2.4 a).

The last step is to dry etch the counter-electrode in two steps. We etch the niobium using the recipe "Nb etching" in Table B.1. We exploit the laser monitoring to detect the aluminum to stop on top of the barrier. We then perform a short overetch. As the etching of the silicon nitride and the niobium is very similar, the magnesium oxide is needed to protect the silicon nitride which is not covered by the niobium. In figure 2.4 b), we observe

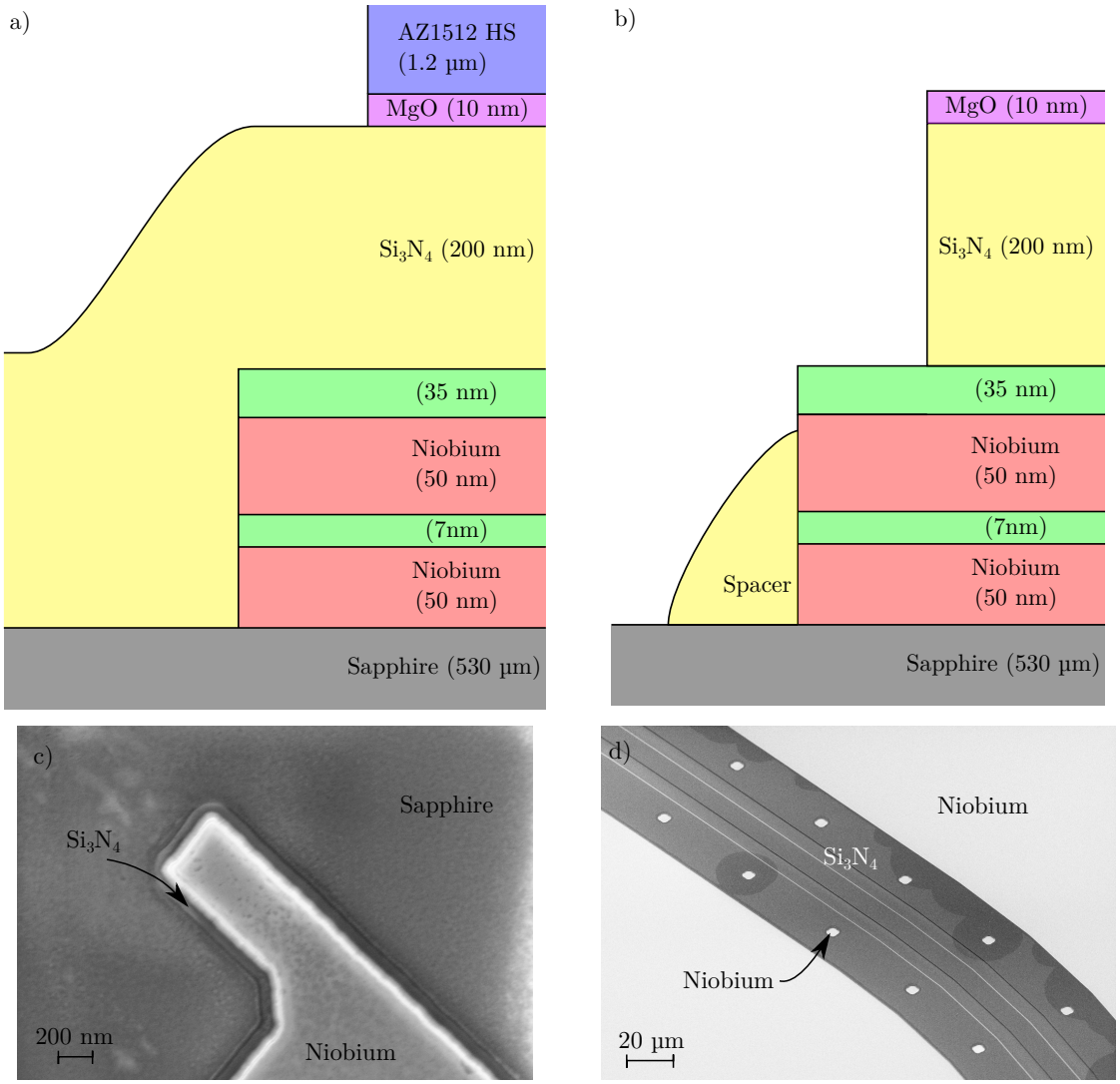

Figure 2.3: a) Representation of the wafer structures before etching of the silicon nitride and after the wet etch of the magnesium oxide. b) State of the wafer after the etching of silicon nitride. A spacer remains at the edge of the trilayer. c) SEM image of the junction area after etch of the silicon nitride and the aluminum. We observe the formation of the spacer. d) We observe the fabrication of vias in this SEM picture realized after the etch of silicon nitride and aluminum. These holes inside the silicon nitride will allow connecting the two large ground planes without connecting the small niobium line in the middle of the picture.

what schematically happens to form a junction and in figure 2.4 c), we see what it looks like in practice. At the same step, we form links between the different ground planes, as visible in figure 2.4 d), and the fabrication of planar capacitors or inductors. Moreover, we can notice in that figure that the ground plane is patterned, the goal is to keep the loading constant and uniform when the etch proceeds from counter-electrode to the upper part of the trilayer. A positive side effect is that the pattern helps to trap vortices inside the holes

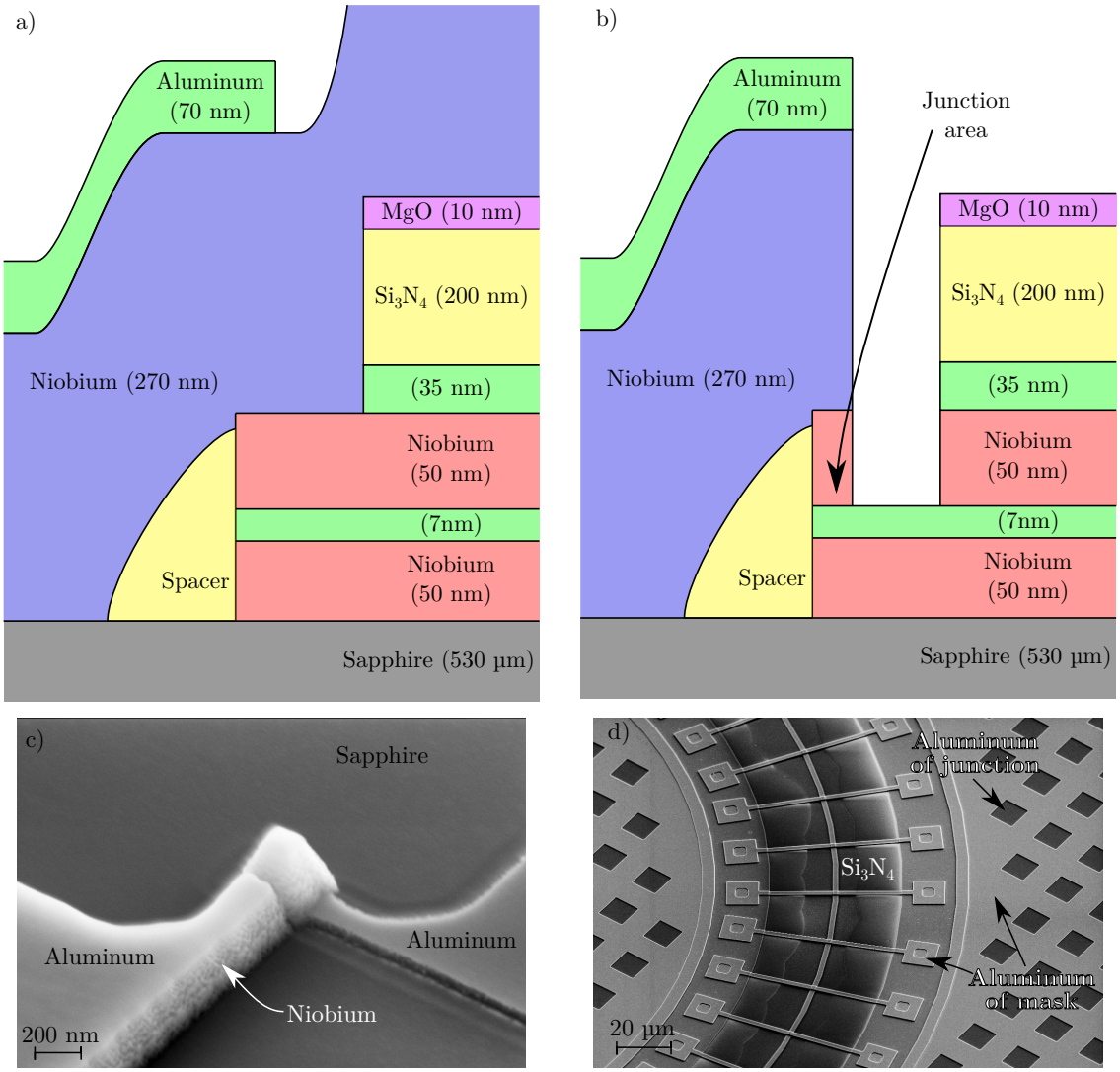

Figure 2.4: a) Sample structure after sputtering of the niobium and definition of the aluminum mask. b) Representation of the wafer after the etch of the niobium. This step defines the junction area by cutting the top layer of the trilayer and creating a conduction path through the aluminum oxide. c) SEM picture of a junction. The junction area is defined by the intersection of two lines to limit alignment problems. d) SEM image of isolated crossing lines. We observe here the connection between the two ground planes of a coplanar waveguide.

which prevents them to move near the junction or the transmission lines.

2.2.6 Process monitoring

We verify each fabrication step using scanning electron microscopy, and we measure the thickness of the layers with a Dektak profilometer. These measurements are performed only on one spot of the wafer as they are cumbersome and the exposition to the electron beam tends to degrade the exposed samples. To monitor the fabrication homogeneity through the

wafer, we insert in the middle of each 10 mm×10 mm chip the structure shown in figure 2.5 a) to measure the resistivity of layers and the characteristics of the Josephson junctions at the end of the process. The junction properties are analyzed in part 2.3.

The characterization is performed with four-wire resistance measurement, as illustrated in figure 2.5 b). In that case, we measure the resistivity of the bottom layer of the trilayer. The resistivity of the full trilayer, the counter-electrode (topwiring in figure 2.5 a)) and of the chromium are measured similarly. A test structure with 10 vias in series is used to verify that they are fully open and to check step connectivity of the counter-electrode. The 744 test structures, 62 chips with 12 test structures (see figure 2.6 a)), are measured with an automatic probe station at room temperature.

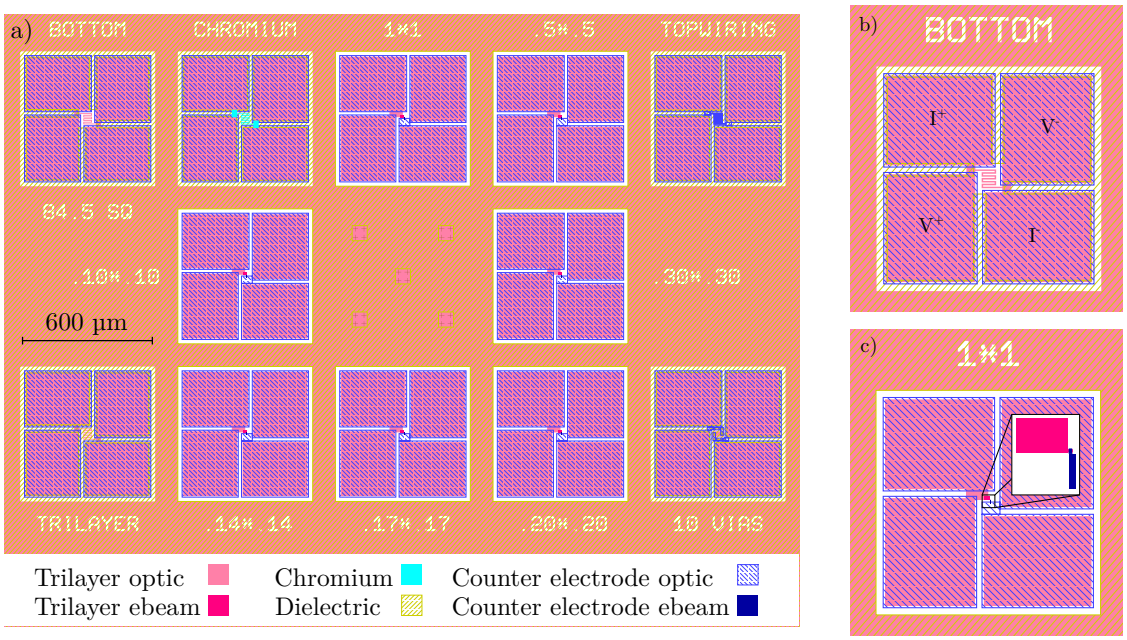

Figure 2.5: a) Layout of the central part of each chip. These structures are used to monitor process variations. b) Meander to measure the resistivity of a layer, here the sheet resistivity of the bottom layer of the trilayer. The measurement is done with a four-wire measurement as indicated with the V^+, I^+, V^- and I^-. c) Layout of a Josephson junction of size 1 µm×1 µm, the junction for SQUIDs has a similar structure, see part 2.3 for the discussion on their properties.

The resistivity of the chromium layer, figure 2.6 e), is the most straightforward to interpret as it measures the good homogeneity of chromium evaporation. As a side note, the residual-resistivity ratio is small $\rho_{300K}/\rho_{4.2K} = 1.1$ and identical through several wafers, so the measurement at room temperature gives a good estimation of the resistivity at low temperature. The resistance of the 10 vias, figure 2.6 f), indicates probably that the etching was not enough to open vias, as the etching rate is smaller near the border of the wafer. The resistivity of the bottom layer of the trilayer, figure 2.6 b), the trilayer, figure 2.6 c), and the counter electrode, figure 2.6 d), are better understood if we compare them. For example, the resistivity of the bottom layer should be 3 times the resistivity of the trilayer, because of the residual aluminum mask which conducted 5 times better than the niobium.

So we can conclude that the aluminum of the junction is not a perfect etch stop as the resistivity of the bottom layer is a bit higher than expected. In the same way, the resistivity of the counter-electrode is expected to be close to the resistivity of the trilayer which we observe experimentally, as the residual aluminum of counter-electrode mask is thinner than for the trilayer.

These measurements indicate that the fabrication is globally working as intended except for some vias, moreover they allow us to preform a first selection of chips to measure at low temperature. However, the resistivity tests do not give any information on our non-linear element, the Josephson junctions.

2.3 Vertical Josephson junction

The Josephson junctions are the key building block of our sample and their most sensitive part. We characterize them at room temperature and at low temperature by putting single junctions at the center of each chip as illustrated in figure 2.5. To minimize alignment problems, the junctions are fabricated through the crossing of two lines, as shown in figure 2.5 c), allowing for 200 nm of misalignment, enough for e-beam lithography. The same geometry is used for the junctions of the SQUIDs.

A lot of scientific publications exist about the fabrication of $Nb/Al/Al_2O_3/Nb$ junction, [50–52] describe the most important parameters to make junctions. Notice that the usual process involves the anodizing of the niobium of the trilayer to prevent short circuit between the bottom layer of the trilayer and the counter electrode. We choose to use spacer instead to reduce the parasitic capacitance of the junction as the niobium oxide possesses an anisotropic and very high dielectric constant.

2.3.1 Room temperature measurement

The junctions are measured at room temperature with the automatic probe station to rapidly estimate the characteristics of the junction. We obtain the result presented in figure 2.7 for a typical working wafer. We observe that the normal tunnel resistance is not very homogeneous with a typical factor 2 between the lowest and highest junction resistance. However, the resistance varies less compared to the previous process (with NbN/MgO/NbN junction) where the resistance changed with a factor 10 through a typical wafer.

Moreover, from the measurement of the junction resistance at room temperature, we can estimate roughly the critical current using the Ambegaokar-Barato formula [53, 54]:

$$I_c(T=0) = \frac{\pi \Delta_0}{2eR_n} \tag{2.1}$$

So the room temperature measurements gives a first indication if the critical current of SQUIDs is suited to observe the photo-multiplication process.

2.3.2 Low temperature characteristics

The room temperature measurements are not enough to fully characterize the junctions, so junctions are measured at liquid helium temperature to verify their properties. We

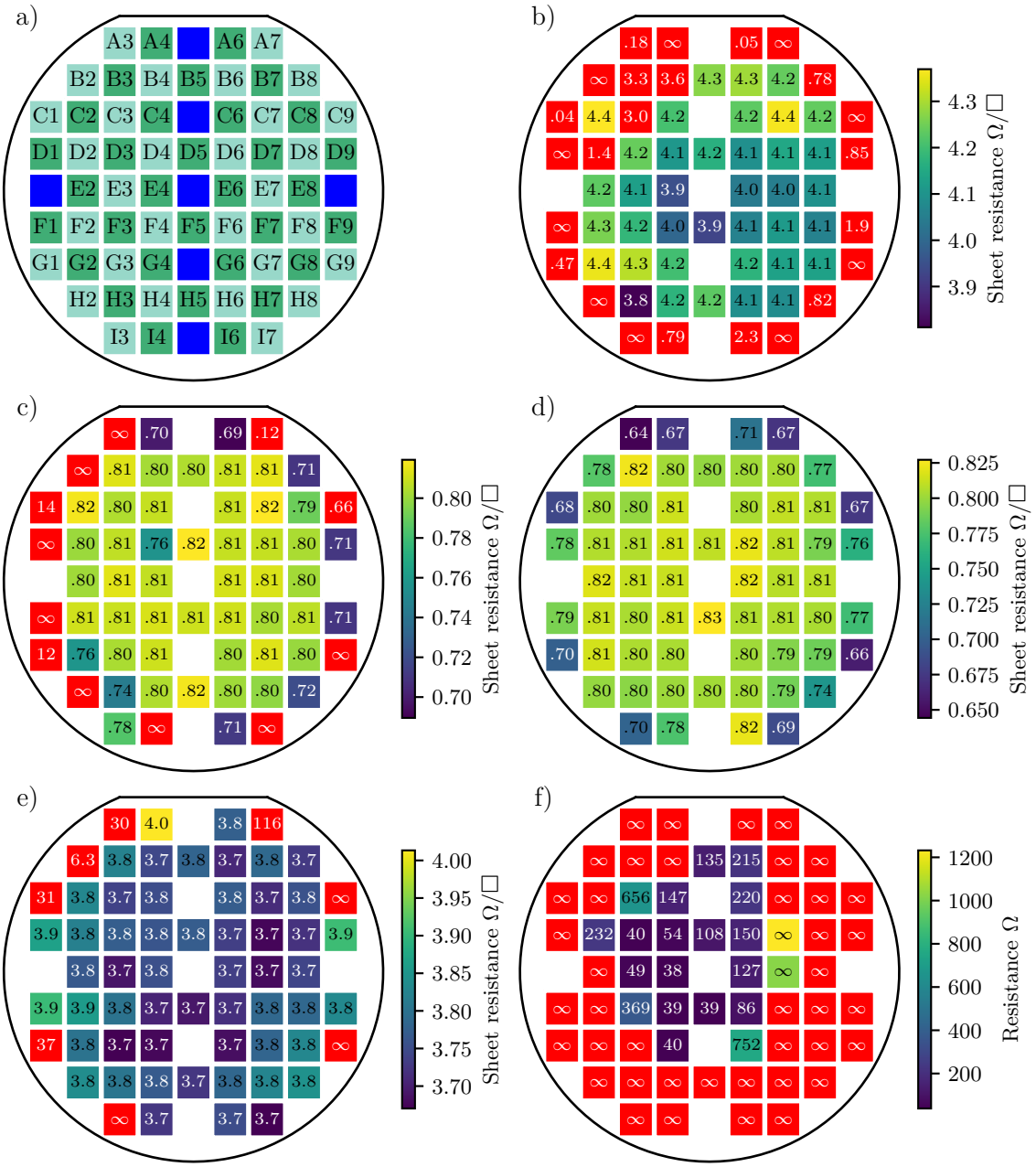

Figure 2.6: a) Structure of the wafer, the blue chips are technical chips which are used for process monitoring. They hold global alignment crosses, lithography test or target for the laser end point detection during etching. b) Sheet resistivity of the bottom layer of the trilayer. c) Sheet resistivity of the full trilayer. d) Sheet resistivity of the full counter-electrode. e) Sheet resistivity of the chromium. f) Resistance of ten vias. Notice that all the resistances are measured at room temperature.

use a Measurement computing USB-1608GX-2AO analog input-output card with home-made differential amplifiers to measure $I(V)$ characteristics of junction through four-wire measurement.

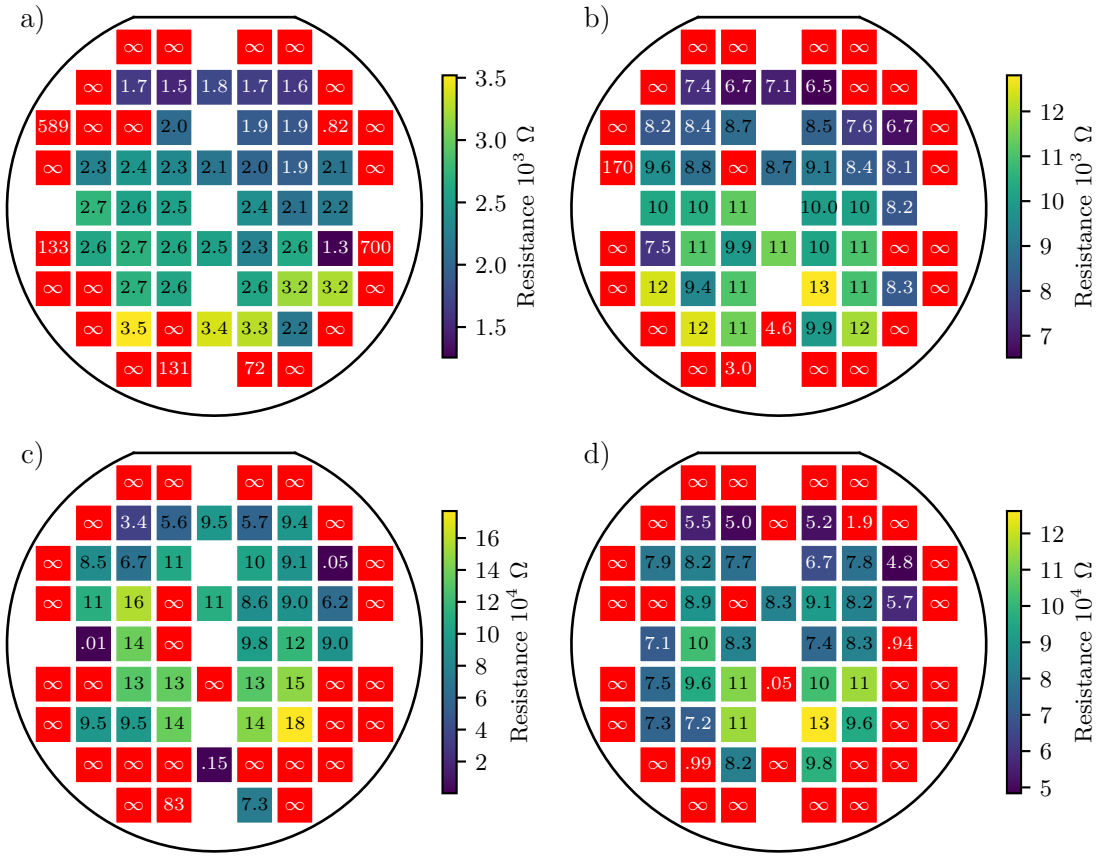

Figure 2.7: Resistance of Josephson junctions of various sizes at room temperature: a) 0.50 µm×0.50 µm b) 0.30 µm×0.30 µm c) 0.14 µm ×0.14 µm d) 0.17 µm × 0.12 µm (Trilayer×Counter-electrode).

In figure 2.8, we show the $J(V) = I(V)/S$ characteristic for the junctions of C7 chip, where S is the area of each junction. This sample comes from the wafer presented in figure 2.7 and figure 2.6. We observe that the measured critical currents are in good agreement with the estimation from room temperature resistance and the typical hysteresis of tunnel junction for the 0.5 µm×0.5 µm. However, we observe that the curves for the three junctions do not collapse. Notice here that the curves for the two smallest junction are on different scales than for the bigger one. This is probably due to the reduction of size of the smallest junction during the etching of the trilayer and of the counter electrode which distort the effective surface of the junction.

To compare with the usual critical current density of Nb/Al/Al_2O_3/Nb junction, the important element is the product of the partial pressure of oxygen p_{0_2} with the duration t of oxidation. The critical current typically scales as $1/\sqrt{p_{0_2}t}$. For the sample presented, the product $p_{0_2}t$ is 3×10^5 Pa · s and we observe a critical current density of around 5 µA · µm^{-2} for the bigger junction. This is ten times smaller than what is usually observed [56, 57]. The annealing of the junction during the silicon nitride deposition, performed at 250 °C, is the most probable reason, as it is known to reduce the critical current [52]. However,

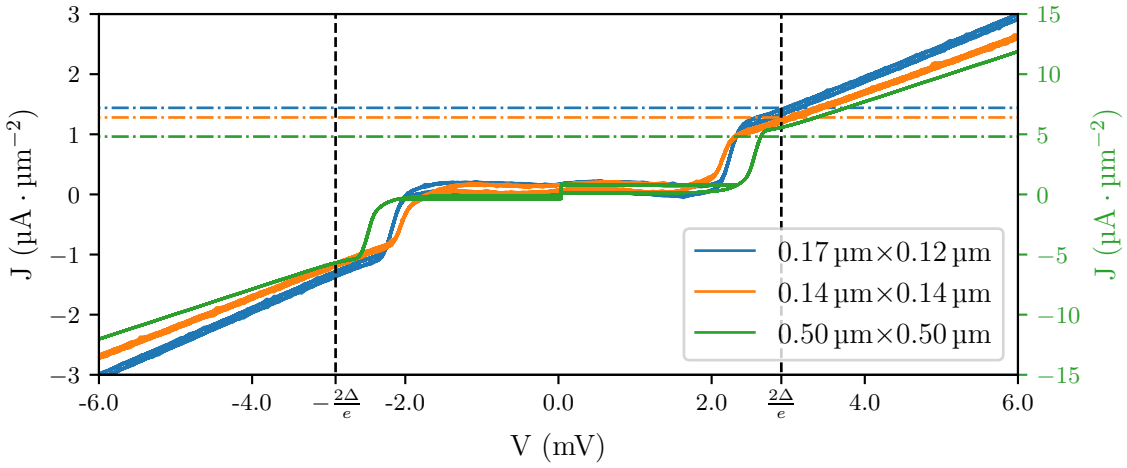

Figure 2.8: Current density J as a function of bias voltage V of single Josephson junctions. Notice that the biggest junction is on the right axis with a factor 5 compared to the left one. The black dashed lines are computed from the bulk gap of niobium [55], the dash-dotted lines are computed from the Ambegaokar-Baratoff equation 2.1.

we can note that when we fabricate wafer with an oxidation of $3 \times 10^7\,\mathrm{Pa \cdot s}$, the critical current density is around ten times lower, so the usual scaling is roughly respected.

The last important property of the junction is the parasitic capacitance of the junction. It comes from two different part, firstly a junction forms a parallel plate capacitor between the two electrode. Secondly the junction is connecting to the circuits through wires, and they couple capacitively because of their proximity. From electromagnetic simulation with Sonnet solver and parallel plate capacitor, we estimate it to be: $\mathrm{C} = 50\,\mathrm{fF \cdot \mu m^{-2}} \times \mathrm{S} + 0.6\,\mathrm{fF}$ with S the area of the junction in $\mu\mathrm{m}^2$.

We will now discuss the other elements needed to design the electromagnetic environment of the junction.

2.4 Capacitor

In order to fabricate a broadband bias-T, provide filtering or control coupling, the use of capacitors is unavoidable. The capacitance of a parallel plate capacitor formed by the trilayer and the counter electrode can be computed as $C = \frac{\varepsilon_0 \varepsilon_r S}{d}$, where S is the surface of the capacitor, d the thickness of the silicon nitride and $\varepsilon_r = 7.5$ is its dielectric constant. The capacitance per unit surface is $0.33\,\mathrm{fF \cdot \mu m^2}$. The smallest capacitors required in our designs are a few femtofarads, so we only use parallel plate capacitors in our design. We do not need inter-digital capacitors because the loss tangent of the silicon nitride is sufficiently low for our application.

It is very important to understand their resonances in order to prevent them from altering the intended behavior of the actual device. Usually, we consider only the self resonance (minimum of impedance) of a capacitor, above which the parasitic inductance starts to become dominant. For our biggest capacitor (100 pF, 560 µm×560 µm), the self resonance frequency is around 2 GHz (parasitic inductance of 60 pH) which is not a problem

for its use in filtering for the working frequencies of device (between 4 GHz and 8 GHz). At higher frequency, the capacitor suffers from $\lambda/4$ resonances of TE modes between the two plates, which results in a maximum of impedance. These resonances couple heavily with the junction and need to be kept as far as possible from the operating frequency of our device. Luckily, this resonance is presently at more than 50 GHz even for the biggest capacitors. For the coupling capacitors, the self resonance frequency are much higher as they are much smaller, so they behave mostly as perfect capacitor.

2.5 Coplanar waveguide (CPW)

Transmission line can also be used to form resonators or matching networks. We use a coplanar waveguide geometry as presented in figure 2.9 a). The straps, an addition to a classical coplanar geometry, fill several objectives. First, they prevent the apparition of slot line resonances by providing a low impedance link between ground plane. Secondly they decrease the typical characteristic impedance of the transmission by increasing the capacitance per unit length and so enable us to fabricate a wide range of characteristic impedances. Finally, they limit the discontinuities in ground plane when several transmission lines are connected at the one point. The main drawback is the resonances which appear when the distance between two straps is of the same order of magnitude of the wave length. This frequency limit to our transmission limit is above 100 GHz for our design.

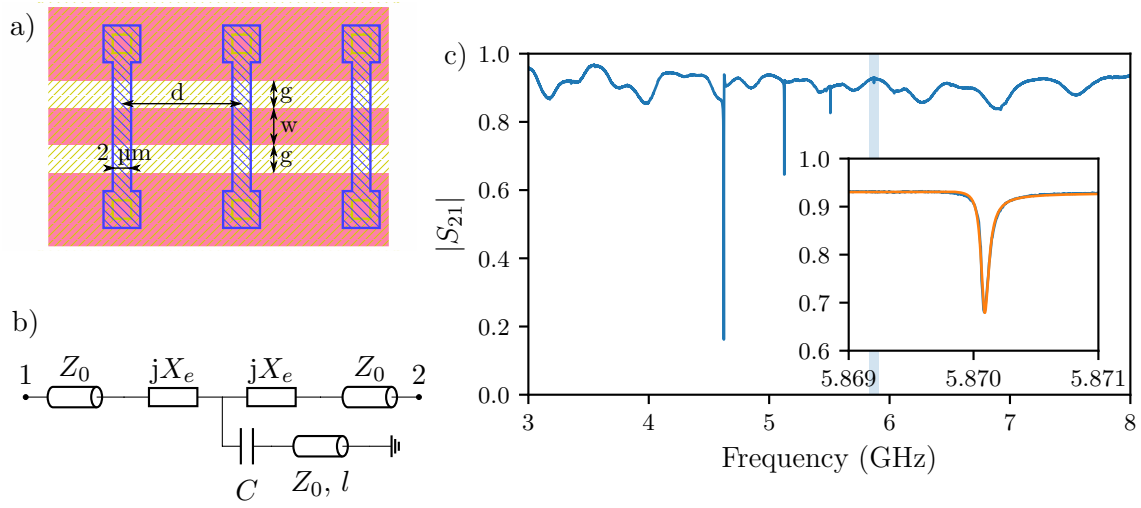

Figure 2.9: a) Layout of a typical coplanar waveguide transmission line. The color code is the same as in figure 2.5. The gap g, the width w and the distance between straps d change the characteristic impedance of the transmission line. b) Electrical schematics of a $\lambda/4$-resonator capacitively coupled to a transmission line. c) $|S_{21}|$ measurement of 4 resonators coupled to a transmission at 13 mK with an input power of -80 dBm. The measurement is normalized using a microwave transfer switch. The inset presents the fit with equation 2.2.

Using the Sonnet solver, we simulate transmission lines to extract the characteristic impedance and the propagation speed. To verify its precision, we couple capacitively four

$\lambda/4$-resonators to a transmission line, the typical schematic is presented in figure 2.9 b). The same geometry (g=7 µm, w=10 µm, d=50 µm) for the resonators and the transmission line between the port 1 and 2 is used to obtain a characteristic impedance near 50 Ω. More precisely, Sonnet simulation gives $Z_0 = 51.2\,\Omega$ and a propagation speed of $11.2 \times 10^7\,\mathrm{ms}^{-1}$.

Using the schematic, we can compute the theoretical transmission between the ports 1 and 2 [58]:

$$S_{21}(f) = \frac{1}{1+\mathrm{j}\frac{X_e}{Z_0}} \frac{1+2\mathrm{j}Q_i\frac{f-f_0}{f_0}}{1+\frac{Q_i}{Q_c}\left(1+\mathrm{j}\frac{X_e}{Z_0}\right)+2\mathrm{j}Q_i\frac{f-f_0}{f_0}} \tag{2.2}$$

This equation fits the experimental data very well, as presented in the inset of the figure 2.9 c). The extracted fit parameters are presented in table 2.3 for the four resonators. Notice that the self-resonance frequency f_r is a bit higher than the measured resonance frequency f_0 due to effect of the coupling capacitor:

$$f_r = f_0\left(1+\sqrt{\frac{2}{\pi Q_c}}\right) \tag{2.3}$$

From this frequency, we can deduce the speed of propagation: $c_p = 4lf_r$.

The reactance X_e is the origin of the asymmetry of the resonance, it comes probably from the wire bonding of the chip with the sample holder. We always use three wires of radius 25 µm which account for about 0.3 nH.

f_0 (GHz)	Q_i	Q_c	$\left\lvert\frac{X_e}{Z_0}\right\rvert$ (L_{eq})	f_r (GHz)	c_p ($10^7\,\mathrm{ms}^{-1}$)
4.623	2.9×10^4	2.6×10^3	0.41 (0.55 nH)	4.696	8.735
5.126	6.5×10^4	1.2×10^4	0.12 (0.15 nH)	5.163	8.863
5.508	1.2×10^4	1.2×10^5	0.26 (0.29 nH)	5.520	8.800
5.871	9.9×10^4	2.7×10^5	0.19 (0.20 nH)	5.879	8.748

Table 2.3: Parameters of the fit for the 4 $\lambda/4$-resonators and the data extracted from them.

We observe that the simulation and the measurement do not agree well, the average speed of propagation measured is $8.79 \times 10^7\,\mathrm{m}\cdot\mathrm{s}^{-1}$ compared with $11.2 \times 10^7\,\mathrm{m}\cdot\mathrm{s}^{-1}$ obtained with Sonnet. Moreover, we can estimate the coupling capacitance C with the parallel plate capacitor formula for the lower frequency and coupling quality factor resonator. Using this value and the parameters of the fit, we can deduce the characteristic impedance:

$$Z_0 = \frac{1}{Cf_0\sqrt{8\pi Q_c}} \tag{2.4}$$

We obtain $Z_0 = 39\,\Omega$.

The Sonnet simulations were performed by taking into account the full stack of dielectric, 200 nm of silicon nitride with 10 nm of magnesium oxide on top. If the same simulation is done with only the silicon nitride, we obtain $Z_0 = 39.1\,\Omega$ and $c_p = 8.542 \times 10^7\,\mathrm{ms}^{-1}$,

in much better agreement with experiment data. The computed capacitance per unit is nearly divided by two with the magnesium oxide ($170\,\mathrm{pF}\cdot\mathrm{m}^{-1}$ with magnesium oxyde compared to $300\,\mathrm{pF}\cdot\mathrm{m}^{-1}$ without). So, the transmission line characteristic are not the one initially intended, the discussion in the thesis is adapted to this problem. However, for the discrete element resonators which we discuss next, the simulation were made without the magnesium oxide to reduce simulation time as the geometry are complex. Therefore, these simulations do not suffer from this problem.

2.6 High impedance resonators

As we saw in Chapter 1, the coupling of the resonator with the Josephson junction is determined by the characteristic impedance of the resonator, compared to the resistance quantum for Cooper pairs $R_Q = h/4e^2 \approx 6.5\,\mathrm{k}\Omega$. Therefore, we need resonators with characteristic impedances in the $\mathrm{k}\Omega$ range to observe the photon multiplication process. This is one order of magnitude higher than usual characteristic impedance of transmission lines and $\lambda/4$-resonator made from them. Naturally, several ways exist to build such resonators, useful for various experiments, see [24, 59] for example.

Three main options exist, first we can build a transmission line where the center conductor is replaced with an array of SQUID [60, 61]. At first order, a SQUID acts as a tunable inductance much larger than the geometrical inductance of a simple wire of the same size. The main advantages of this method are the very high impedance possible and the tunability of the frequency and impedance of the resonator with the flux applied to the SQUID array. The main drawback is the complexity of the fabrication and the non-linearity of such an array. A second way is to use the kinetic inductance of a superconductor, which comes from the inertia of the carriers [62]. The kinetic inductance is important in thin films of disordered superconductors such as niobium nitride [63]. The advantage of this method is the relatively simple fabrication in theory, but the dependance of the kinetic inductance to fabrication details (for example the defects created by etching) complicate the control of its precise value and thereby the frequency of the resonator. This is one of the main reasons for using niobium instead of nitride niobium. The last method is to use the self resonance of a planar coil [1, 64]. The main advantage of this method is the relatively easy control of the resonance frequency, even if the simulation can be challenging. The problem of this method is the difficulty to go to high frequency as it is directly linked to the geometry of the coil which is limited by the fabrication process.

As we wanted to keep the fabrication simple and more reliable and because of previous difficulties of the group with niobium nitride, we choose to use niobium spiral inductor as our high impedance resonator.

2.6.1 Planar coil and microwave simulation

The use and fabrication of planar coil was studied extensively for RF applications in microelectronics [65–67]. Several forms of planar coils are commonly used and studied. We present three of them in figure 2.10. The square inductor (figure 2.10 b)) maximizes the inductance per surface and the spiral inductor (figure 2.10 a)) maximizes the internal quality factor of the inductor. The other forms, i.e. the hexagonal one (figure 2.10 c)) or

the octagonal one, are intermediates between those two aspects. The spiral inductor is the most promising geometry as a high quality factor is correlated with a high self-resonance frequency and characteristic impedance.

A spiral inductors possess different geometrical variables, such as the spiral parameters and the pads and straps necessary to connect the center of inductor to the outside. For the center pad, we choose to minimize its size with respecting the alignment tolerances of optical masks, in order to reduce capacitance to ground. We usually align the mask with a tolerance of around 1 µm, so we design a pad which tolerates a misalignment up to 3 µm. The wire width $w = 1$ µm is the minimal reproducible wire we can fabricate with optical lithography. The distance between two wires $h = 1$ µm is a compromise between the inter-winding capacitance and the size of inductor which increases capacitance to ground

To vary the characteristics of the inductor (inductance, self-resonance frequency or characteristic impedance), we vary the internal radius R and the number of turn N. We simulate these inductors with Sonnet in order to extract the important properties for our devices.

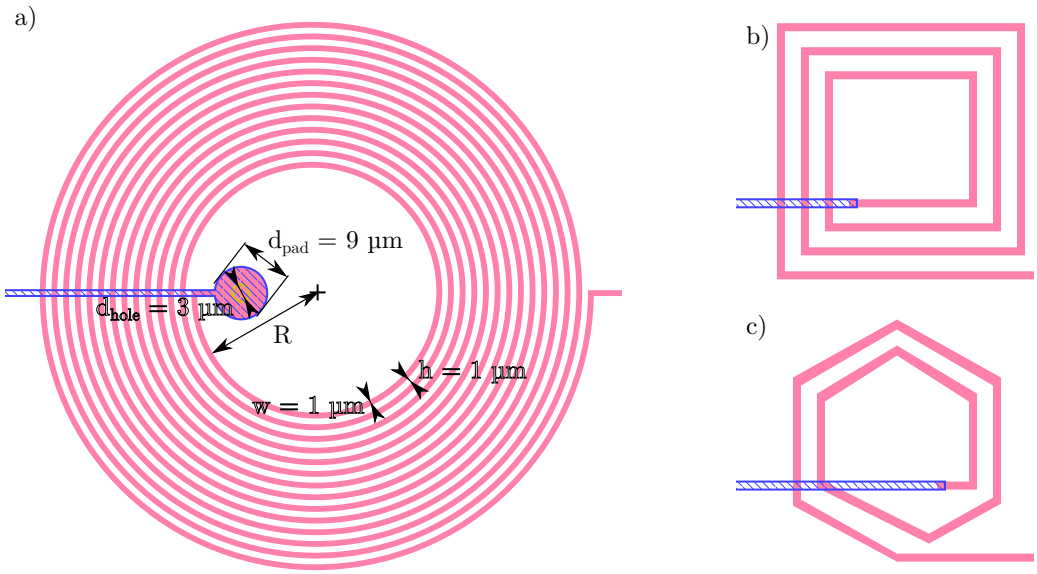

Figure 2.10: a) Layout of a spiral inductor. We only vary the internal radius R and the number of turns to change the inductance and self resonance frequency, the other geometrical parameters are fixed for every inductor. b) Square inductor. c) Hexagonal inductor. The color code is the same as in figure 2.5.

2.6.2 Compact lumped component model extraction

From Sonnet simulations, we extract the impedance matrix as presented in figure 2.11 b). The results are complicated and do not map well directly to a simple LC circuit. Therefore, I develop a simple lumped elements circuit, presented in figure 2.11 a), to better understand the behavior of the inductors. This circuit allows to model the first two modes of the inductor. The first mode will be used as the resonator for our devices and we check

that the second mode is not harmful. As we can see in figure 2.11 b), the agreement between the lumped component model and the Sonnet simulation is quite good.

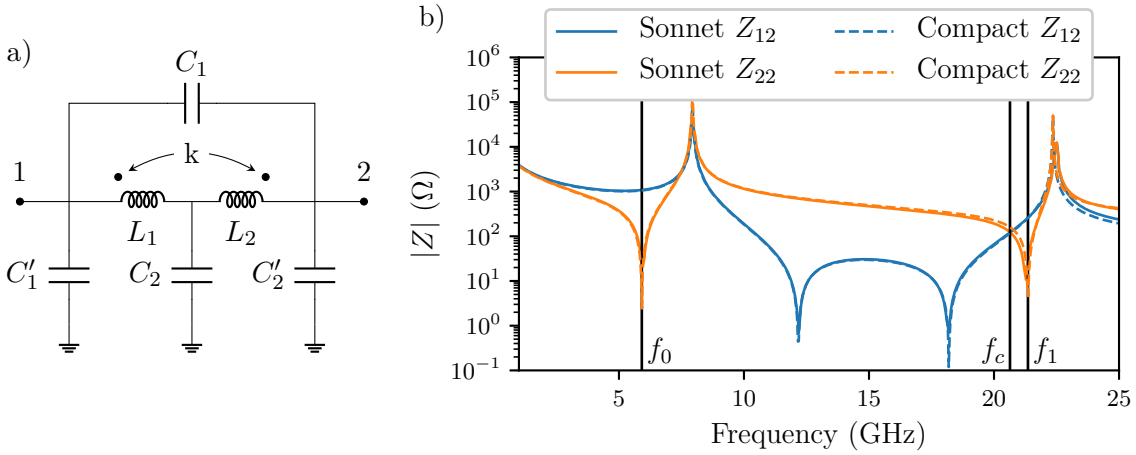

Figure 2.11: a) Lumped-elements circuit used to model the first two modes of a spiral inductor. b) The continuous line shows two terms of the impedance matrix extracted from a Sonnet simulation of a spiral inductor with internal radius R = 50 µm and N = 10.5 turns. The dashed lines shows a fit of these terms using the model in part a).

For the different variants of the photo-multiplier, we need various characteristic impedances and resonance frequencies. Therefore, we extract the component values for numerous inductors, presented in table 2.4.

# turns	R (µm)	L_1 (nH)	L_2 (nH)	k	C_1 (fF)	C_2 (fF)	C_1' (fF)	$C\prime_2$ (fF)
10.5	20	7.41	9.71	0.52	6.84	2.58	14.68	9.40
14.5	20	13.43	15.19	0.43	7.81	3.87	16.35	9.46
10.5	50	13.36	16.73	0.30	10.38	6.18	21.54	14.24

Table 2.4: Lumped component values extracted from the Sonnet simulation for two numbers of turns and two internal radius.

It is complicated to directly compare inductors from the model components, so we extract the characteristic impedance and the resonance frequency of the inductors as they are the most pertinent properties for the design of devices. In a photo-multiplication sample, the inductors are coupled to the ground between 1 GHz and 40 GHz at port 2. The impedance seen by the junction is therefore the impedance seen from the port 1 when the port 2 is grounded [68]:

$$Z(\omega) = \frac{V_{11}}{I_{11}}\bigg|_{V_{22}=0}(\omega) = \frac{1}{Y_{11}(\omega)} = \frac{Z_{11}(\omega)Z_{22}(\omega) - Z_{12}(\omega)Z_{21}(\omega)}{Z_{22}(\omega)} \tag{2.5}$$

From the lumped components model, the impedance can be factorized, see Annex C.1:

$$Z(\omega) = \frac{\mathrm{j}\omega L_{eq}\left(1 - \frac{\omega^2}{\omega_c^2}\right)}{\left(1 - \frac{\omega^2}{\omega_0^2}\right)\left(1 - \frac{\omega^2}{\omega_1^2}\right)} \tag{2.6}$$

where L_{eq} is the inductance equivalent of the two coupled inductors, ω_0 is the frequency of the first mode, ω_1 the frequency of the second mode and ω_c is a frequency at which the impedance becomes zero (which might be useful). The characteristic impedance of the first and second mode can also be extracted from this formula, as presented in table 2.5.

The characteristic impedance decreases when the frequency of first resonance increases for a given internal radius. Moreover, at constant characteristic impedance, the resonance frequency decreases when the internal radius increases. The inductors with small internal radius have smaller parasitic capacitance (higher characteristic impedance) at a given frequency of resonance. As the holes in the ground plane to host inductors are all identical, it directly reflects the fact that the smaller inductors are further away from the ground plane.

N	R (µm)	f_c (GHz)	f_0 (GHz)	$Z_{\text{eff},0}$ (Ω)	f_1 (GHz)	$Z_{\text{eff},1}$ (Ω)
10.5	20	39.35	11.65	599	40.40	10.19
14.5	20	25.34	7.82	795	26.02	14.35
10.5	50	20.64	5.91	783	21.36	16.74

Table 2.5: Resonance frequency and characteristic impedance of coils extracted from Sonnet simulation.

2.6.3 Experimental confirmation

Until now, we only presented result from electromagnetic simulation. Yet, as discussed in part 2.5, the simulations are not always accurate. Therefore, we fabricated samples with an inductor embedded in a 50 Ω transmission line and measure the transmission trough it at dilution temperature. The experimental data is displayed in figure 2.12.

Firstly, we observe that the lumped components model allows to fit well the measured transmission. However, this fit is performed with $C_1' = C_2' = 0$ because the scattering term S_{12} depends only slightly on these capacitors, so we are not able to precisely extract the characteristic impedance of the different modes. Notice that we can only measure accurately S_{12} as we did not perform a full calibration at dilution temperature, but use a transfer switch to normalize the transmission trough the sample.

Secondary, we see that the agreement between the Sonnet simulation and the experimental data is not fantastic. If we decrease the apparent thickness of the dielectric by one third in Sonnet, we obtain a very good agreement. This comes probably from the fact that the thickness of our wire (110 nm) is of the same order of magnitude than the thickness of the dielectric (200 nm), whereas we perform the simulation with 2D wires to keep computation cost reasonable. The main effect is to underestimate all parasitic capacitances.

Conclusion

As presented in this chapter, I altered the group's process in order to increase reliability while maintaining its advantages. The fabrication of the first planar coil was an important step towards a photomultiplier and the results demonstrate that they function as intended.

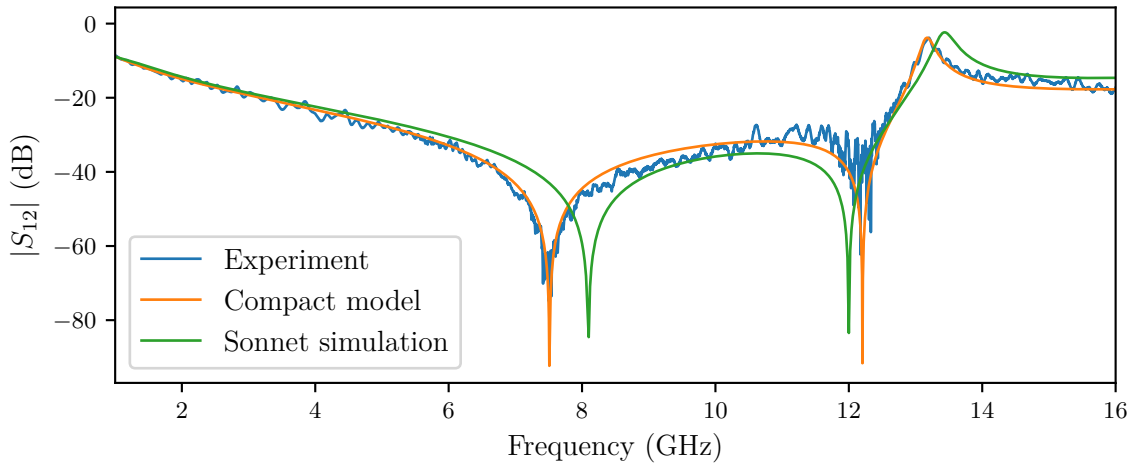

Figure 2.12: Transmission through an inductor (R = 50 µm and N = 14.5) at 13 mK with an input power of −70 dBm. The experiment is normalized using a transfer switch. The lumped element components are adjusted to fit the experiment (with $C_1' = C_2' = 0$), while the Sonnet simulation is directly performed from the geometry.

However, the reproducibility of the Josephson junctions remains to be optimized even if many of them work.

Chapter 3

Sample design

Contents

As discussed in chapter 1, the electromagnetic environment controls the photo-emission and the probability of other processes to occur. Its design and physical implementation is therefore the key element we need to master.

Two different samples will be introduced. We will first explain the conception of a simple sample for measuring the thermal broadening of the emission lines. Then we will discuss the design of a device converting one photon to multiple photons, as explained in section 1.3.

3.1 Single resonator design

The main objective of this device is to characterize the experimental setup with a simple sample. As a consequence, it must verify as much as possible the approximation used in the $P(E)$ theory, see section 1.2.4. The characteristic impedance of the fundamental mode must be relatively small. Moreover, the fabrication must be as simple as possible in order to have a good matching between the modeling and the actual device. This is why we choose to use a transmission line resonator with relatively low impedance for the high frequency part. In addition, similar devices were extensively studied [3–5, 44] and they can be used as a reference to understand defects in the experiments.

For the previous experiment in the group, the biasing voltage was provided by an external bias-T. However, the biasing circuit is naturally integrated in the chip for a photon multiplier, as describe in section 1.3. This is why, we decide to integrate the bias-T on this device too.

This two constraints lead to the device described by the electrical schematics in figure 3.1, the exact geometrical definition of the components are in table 3.1.

The resonator is made from the two transmission lines, the first $TL0$ controls its characteristic impedance Z_c (and coupling constant r) and the resonance frequency, whereas

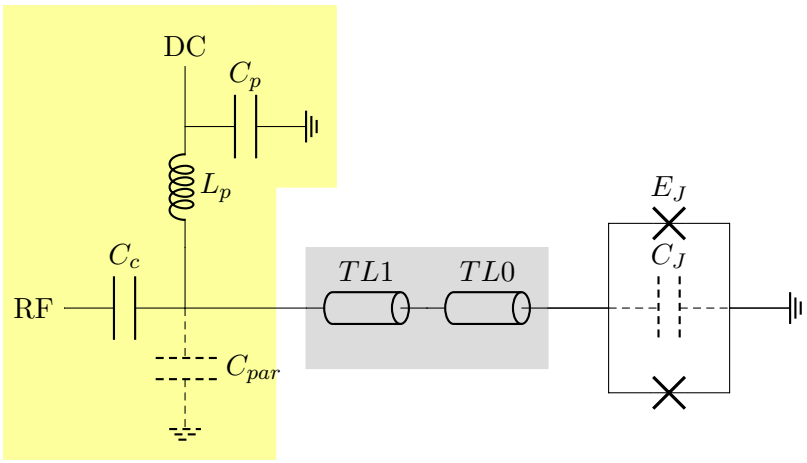

Figure 3.1: Schematics of the test sample. All the components printed in solid lines are physically present. The bias-T which separates the high frequency and low frequency is shown in yellow and the high frequency resonator is in gray. They are connected to a SQUID to be able to adjust the Josephson junction. The geometry of the components are given in table 3.1. In dashed line, we represent two main parasitics components which were taken into account, besides the parasitics components of the spiral inductor.

the second one $TL1$ adjusts its bandwidth. The bias-T is made from a capacitor C_c which couples the radiation to the radio-frequency measurement circuit (in a $50\,\Omega$ environment) while the spiral inductance L_p connect the SQUID to the biasing circuit at low frequency. The cut-off frequency of this bias-T is $\left(2\pi\sqrt{C_c L_p}\right)^{-1} \approx 300\,\text{MHz}$ to match the cut-off frequency of the biasing circuit which is constituted by C_p and the port DC. The DC port acts as a resistor $R_p = 5\,\Omega$, this gives us a cut-off frequency of $(2\pi C_p R_p)^{-1} \approx 320\,\text{MHz}$. The resonance of the coil must be at a higher frequency than the working frequency. Notice that this parasitic resonance is shunted by the capacitance C_c which explains its large value, this mitigates its potential impact.

The impedance seen from the junction is presented in figure 3.3. We observe a strong resonance at 6 GHz which was the target frequency for the resonator and a relatively smooth transition from the bias-T.

In order to accurately consider the parasitic effects in such device, we need to consider the physical implementation which causes them. We show a microscopic image of an actual die in figure 3.2 a). All chips share a symmetrical structure, 8 matched pads are distributed to connect the device to a PCB and the center consists of test structures described in section 2.2.6. Two pads are dedicated to the biasing circuit with a big capacitor C_p directly connected to them. Two testing devices are implemented on each chip, one on the top and one on the bottom of the chip. On the right, we added the same device but without the bias-T to study its impact.

We focus on one device in figure 3.2 b). Starting from the SQUID, we follow with two $\lambda/4$ transmission line resonators to reach the coupling capacitor C_c of the bias-T. One side of the capacitor is connected to a $50\,\Omega$ radio-frequency line and the other side is connected to the inductor L_p. This inductor is connected to the filtering capacitor C_p and the pad

Component	Geometry	Main characteristics
$TL0$	$l = 4343\,\mu m$, $d = 25\,\mu m$ $g = 23\,\mu m$, $w = 2\,\mu m$	$Z = 100\,\Omega$, $f_r = 6\,GHz$ ($Z = 78.5\,\Omega$, $f_r = 4.72\,GHz$)
$TL1$	$l = 3601\,\mu m$, $d = 25\,\mu m$ $g = 5\,\mu m$, $w = 38\,\mu m$	$Z = 24.9\,\Omega$, $f_r = 6\,GHz$ ($Z = 14.8\,\Omega$, $f_r = 3.51\,GHz$)
L_p	$R = 20\,\mu m$, #turns $= 10.5$	$L_{eq} = 8.2\,nH$, $f_r = 11.7\,GHz$
C_c	$S = 0.16\,mm^2$	$C = 53\,pF$
C_p	$S = 0.31\,mm^2$	$C = 104\,pF$

Table 3.1: Component geometries of the test device, described in figure 3.1. The geometrical parameters of transmission lines are defined in figure 2.9 and their lengths are noted l. The characteristics outside the parentheses give the intended value, the values inside parentheses are values expected after correcting the problem in the Sonnet simulations, see section 2.5. For the planar coil, the geometry is defined in figure 2.10 and the capacitors are made from parallel plates with a surface S (see section 2.4).

which makes the link to the voltage biasing circuit. The last part is the flux-bias of the SQUID: A small coil is placed near it to impose a magnetic flux. This coil possesses a high resonance frequency ($> 50\,GHz$) and is driven by a $50\,\Omega$ transmission line which makes it possible to rapidly change the flux if needed.

The capacitor C_c is quite large, therefore, it has a large capacitance to ground which can be modeled by an additional capacitor $C_{par} = 200\,fF$, in dashed line in figure 3.1. The parasitic capacitance of the SQUID can have a strong effect too. Its value is proportional to the surface S of each junction of the SQUID: $C_J = 100\,fF \cdot \mu m^{-2} \times S + 1.2\,fF$. For a $0.30\,\mu m \times 0.30\,\mu m$ junction, the parasitic capacitance is $C_J = 10\,nF$. In figure 3.3, we observe a reduction of the resonance frequency of around 5% due to these two parasitic capacitances.

Finally, we need to take into account the change in resonance frequency due to the problem during the simulation of the transmission lines. As described in section 2.5, the capacitance per unit length was underestimated. In figure 3.3, we show the corrected impedance with a strong reduction of the resonance frequency, as the speed of light in the transmission lines increases.

From this curve, we can extract the properties of the resonator. The resonance frequency is $4.42\,GHz$ and the characteristic impedance is $82\,\Omega$ (coupling factor $r = 0.040$). The HWFM of the resonator is $152\,MHz$. Moreover, we observe a resonance at $740\,MHz$ with a characteristic impedance of $41\,\Omega$. We will not give detailed results from this sample, but it is used in section 4.2.2 to measure properties of the voltage-biasing circuit. We will now focus our attention on the main device of this thesis.

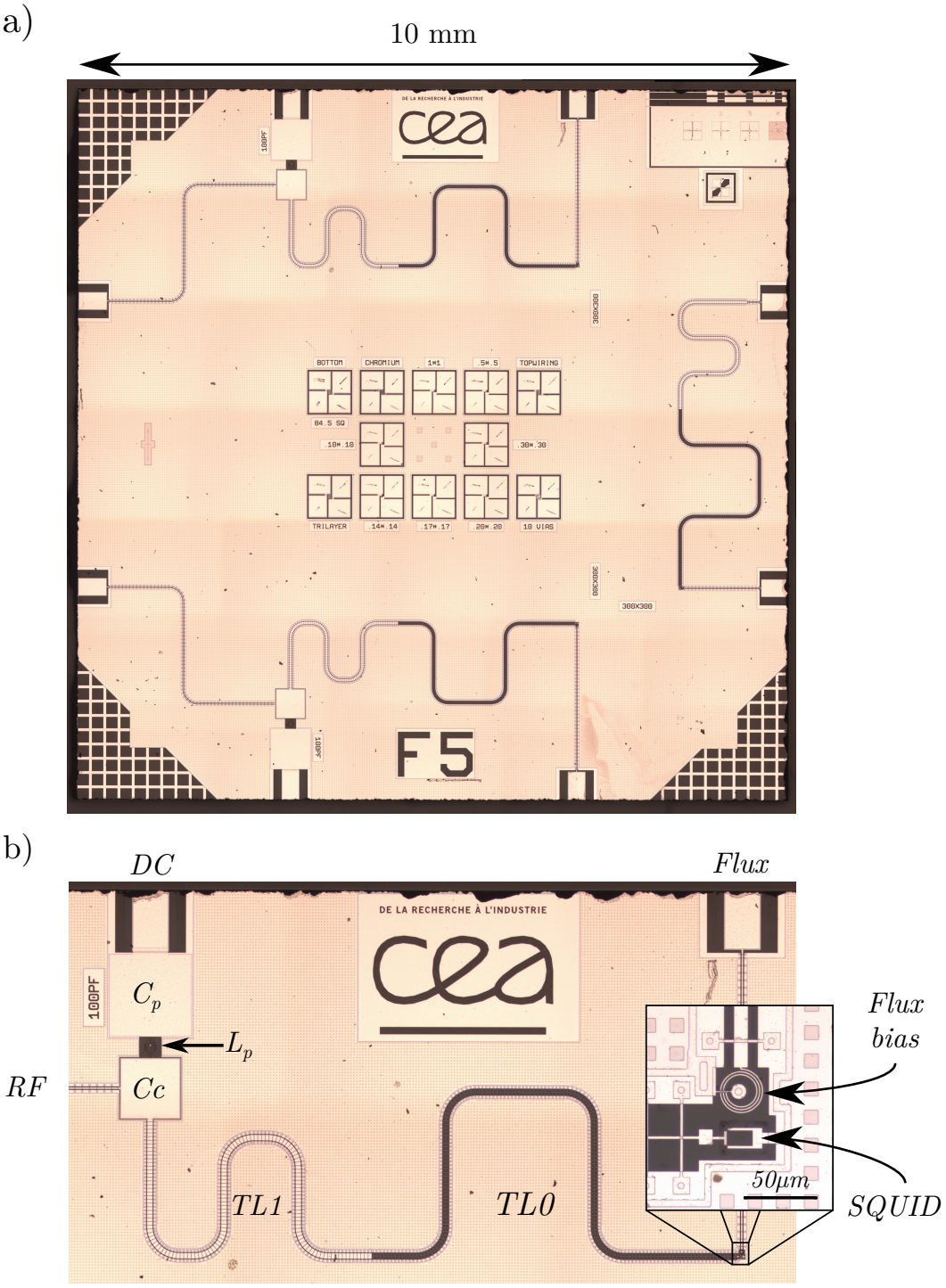

Figure 3.2: Optical microscope pictures of the test sample. a) Full die, its size is 10 mm×10 mm. b) Zoom of the electrical components of one device and of its SQUID.

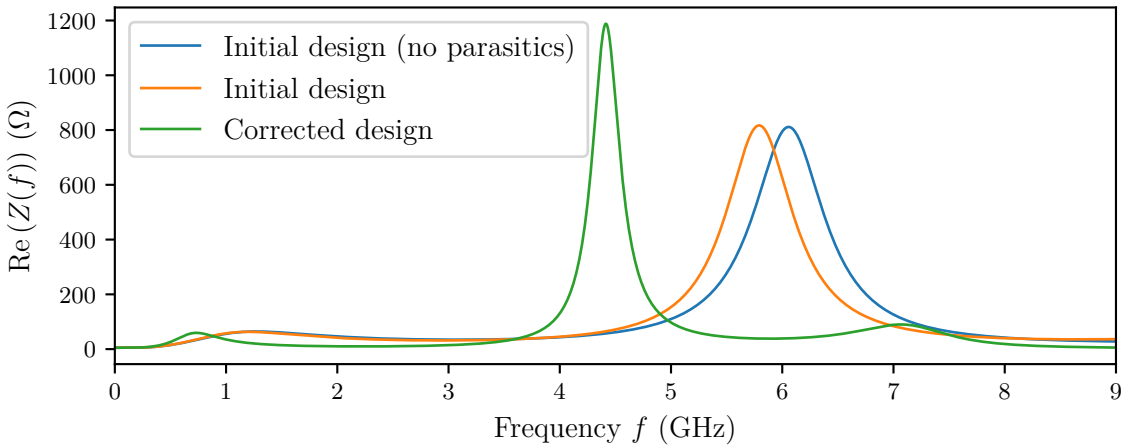

Figure 3.3: Real part of the impedance of the electromagnetic environment seen from the junction as a function of the frequency. The effect of the parasitic components, $C_{par} = 200\,\text{fF}$ and $C_J = 10\,\text{fF}$, is relatively small. However we observe a strong reduction of the resonance frequency when we correct the original simulation of the transmission line. This is expected as Sonnet underestimates the capacitance per length and so overestimates the speed of light on the first simulation (see section 2.5 for details).

3.2 Multiplication of photons

As discussed in section 1.3, the electromagnetic environment must respect several requirements. First, the resonator must be inside the frequency range of the experiment setup (C-band 4 GHz to 8 GHz, see chapter 4). Then the bias voltage of the resonant process, where one incoming photon is converted to n outgoing photons, must not enable a strong spontaneous emission-process. We will concentrate on devices where the output frequency is lower than the input frequency for this thesis. Even through I designed devices to perform an up-conversion, it is slightly easier to obtain high characteristic impedance at lower frequency and functional samples were obtained only for the down-conversion sample.

An input frequency of 7 GHz and an output frequency of 5 GHz imply a biasing voltage of 3 GHz for $n = 2$ and 8 GHz for $n = 3$. We will try to stick to these frequencies, as these biasing points are outside of the bandwidth of both resonators. Indeed, we search to obtain a bandwidth of 100 MHz, or to say it differently a HWFM γ_a and γ_b of 50 MHz. Finally, the characteristic impedance of the output resonator must be as high as possible to minimize the Josephson energy required in order to reach the matching condition and decrease the spontaneous emission of the system. To maximize the dynamical range, the characteristic impedance of the input resonator must relatively small, 250 Ω seems to be a good comprise.

To match theory as closely as possible, we choose to directly stick to the theoretical electrical schematics. This gives us the schematic in figure 3.4. As in the previous part, the physical components are drawn in solid lines (with their geometrical characteristics in table 3.2) and the important parasitic capacitances in dashed lines. A photo-multiplier consists of the following parts. The input resonator and output resonator are formed with capacitively coupled planar coils. Their exact configuration will be described first. The

SQUID, couples the two resonators, and we will discuss its constraints second. Finally, we will discuss the effect of the other parasitic capacitances, notably their impact on the resonance properties.

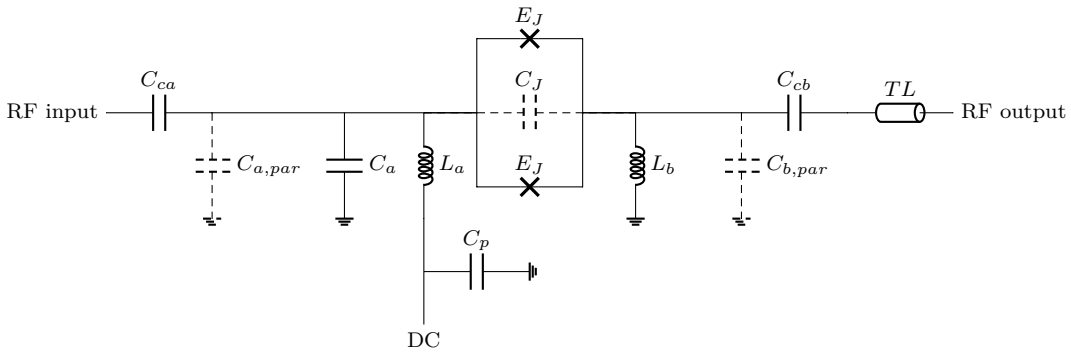

Figure 3.4: Schematic of a photo-multiplier device. As for the previous device, the electrical model of the spiral inductors is not represented but is taken into account for the simulation. The other parasitic capacitances are shown in dashed lines. The geometries and values of all components are given in table 3.2 for a down-converting photo-multiplier.

3.2.1 Input/Output resonators and impedance matching

All capacitances added to the resonators decrease their characteristic impedances and their resonance frequencies. As a consequence, the planar coils were chosen to present higher frequencies of resonance than their targets, see table 3.2. The input and output resonators are treated slightly differently as their characteristic impedances must be different.

For the input resonator, we add a capacitor in parallel with the planar coil to decrease simultaneously its resonance frequency and characteristic impedance. Then the coupling capacitor is chosen to obtain the wanted bandwidth.

For the output resonator, we want to obtain a characteristic impedance as high as possible. Therefore, we need to minimize the coupling capacitor, but this coupling capacitor controls the bandwidth too. To combine this two opposing effects, we add a $\lambda/4$ transmission line transformer. The impedance seen from the coupling capacitor Z_{eff} can be written as a function of the impedance of the $\lambda/4$ transformer Z_c and the output transmission line $Z_0 = 50\,\Omega$ [68]:

$$Z_{\text{eff}} = \frac{Z_c^2}{Z_0} \tag{3.1}$$

We obtain $Z_{\text{eff}} = 228\,\Omega$ ($169\,\Omega$ after correction due to the underestimation of capacitances, see section 2.5) at the resonance, which increases significantly the coupling compared to a $50\,\Omega$ environment. Notice that the working frequency (5 GHz) of this $\lambda/4$ transformer is significantly lower than the resonance frequency of the output resonator (5.7 GHz). The input resonator has a higher resonance frequency (7.2 GHz) than the target too. Indeed, additional parasitic capacitances are always present and decrease the resonance frequencies of the resonator. We will now discuss their impact on our design in the next two parts.

Component	Geometry	Main characteristics
TL	$l = 5583\,\mu m$, $d = 50\,\mu m$ $g = 23\,\mu m$, $w = 2\,\mu m$	$Z = 107\,\Omega$, $f_r = 5\,GHz$ ($Z = 91.9\,\Omega$, $f_r = 4.29\,GHz$)
L_a	$R = 50\,\mu m$, #turns $= 6.5$	$L_{eq} = 7.95\,nH$, $f_r = 10.0\,GHz$
L_b	$R = 50\,\mu m$, #turns $= 10.5$	$L_{eq} = 20.8\,nH$, $f_r = 5.91\,GHz$
C_a	$S = 32\,\mu m^2$	$C = 10.6\,fF$
C_{ca}	$S = 64\,\mu m^2$	$C = 21.3\,fF$
C_{cb}	$S = 35.2\,\mu m^2$	$C = 11.7\,fF$
C_p	$S = 0.31\,mm^2$	$C = 104\,pF$

Table 3.2: Component properties for the down-converting photo-multiplier with the schematic in figure 3.4. Their geometrical parameters are defined in figure 2.9 for the transmission line (in parentheses the value corrected for Sonnet simulation errors), and in figure 2.10 for the planar coil, with S is the surface for the parallel plate capacitors.

3.2.2 Impact of SQUID parasitic capacitance

As discussed in section 3.1, the SQUID possesses a parasitic capacitance C_J. For a SQUID with $0.17\,\mu m \times 0.17\,\mu m$ Josephson junctions, the parasitic capacitance is 4 fF. The effect on the impedance is shown in figure 3.5. We observe a significant decrease of the resonance frequencies as this capacitance re-normalize the capacitance of the resonator (similarly to the coupling capacitor C_{ca}, C_{cb}.). Another effect is the loss of the isolation between the two sides of the device. For a perfect sample, the only way to transmit power from one side to the other side is through a photon multiplication. With the parasitic capacitance, part of the power can go through it without being converted. It can be large depending on the capacitance, up to 12% of power is transmitted in figure 3.5.

It is important to note that the impact of the capacitance of the junction is more important than in previously studied devices in our group for two reasons: First, we are using high characteristic impedance resonators which make use of low capacitances, the relative impact of the SQUID capacitance is therefore higher than before. Secondly, the junction was usually connected to the ground which does not leak signal.

As this parasitic capacitance is unavoidable, we consider it from the beginning and estimate the properties of the resonators before drawing the actual circuit. They are presented in table 3.3, they match our requirements. Using equation (1.61), the Josephson energy to achieve a photo multiplication by a factor $n = 2$ is 29.4 µeV (or $I_c = 14.3\,nA$) and by a factor $n = 3$ is 154 µeV (or $I_c = 75\,nA$). As these values were acceptable and can be achieved with $0.17\,\mu m \times 0.17\,\mu m$ Josephson junctions, we will focus now on the physical implementation of such a device.

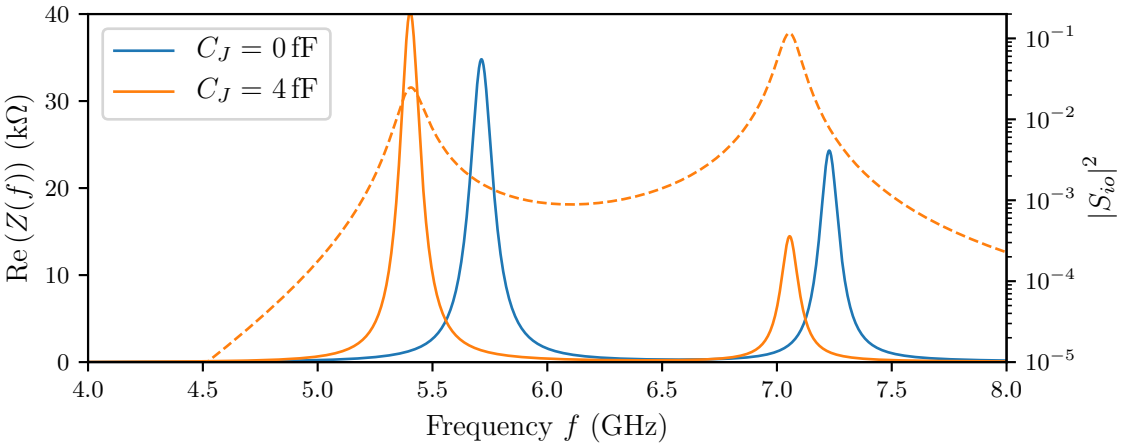

Figure 3.5: In full lines, we represent the real part of the impedance with and without taking into account the parasitic capacitance of the SQUID (here $C_J = 4\,\mathrm{fF}$. In dashed lines, we plot the power transmitted from input to output port due to this capacitance. For this case, we observe a transmission of 12% of the input power. The parameters of the transmission line for this simulation are not corrected for Sonnet simulation errors to illustrate the initial design.

Resonator	Frequency	HWHM $\gamma/(2\pi)$	Impedance characteristic
Input a	7.06 GHz	49 MHz	201 Ω
Output a	5.40 GHz	56 MHz	832 Ω

Table 3.3: Properties of the input and output resonators with the parasitic capacitance of the SQUID C_J =4 fF.

3.2.3 Physical implementation

In order to correctly consider the other parasitic capacitances, we need to focus on the physical implementation of the electrical schematic. We show a sample in figure 3.6 which illustrates the organization and makes it possible to estimate additional parasitic capacitances $C_{a,\mathrm{par}}$ and $C_{b,\mathrm{par}}$.

We recognize the same organization as for the previous sample, two photo-multipliers are present on each chip, one on top and one at the bottom. The radio frequency input line is capacitively coupled to the input resonator made from the spiral coil L_a and the capacitors C_a and C_{ca}. This resonator is coupled to the output resonator with the SQUID. The output resonator, made from the spiral coil L_b and the capacitor C_{cb}, is capacitively coupled to the transmission TL which is used as an impedance transformer. This transmission line is directly connected to the output transmission line.

The wire between the SQUID and the spiral coil L_b is quite long (100 µm) and not very far from the ground plane. Therefore, it possesses an important capacitance to ground which we can estimate to be $C_{b,par} = 17\,\mathrm{fF}$ (including the capacitance to ground of the

SQUID). Notice that this capacitance is far from negligible if we compare it to the parasitc capacitance 24 fF of the spiral coil alone. We can perform the same estimation for the input resonator, the parasitic capacitance is $C_{a,par} = 6\,\text{fF}$.

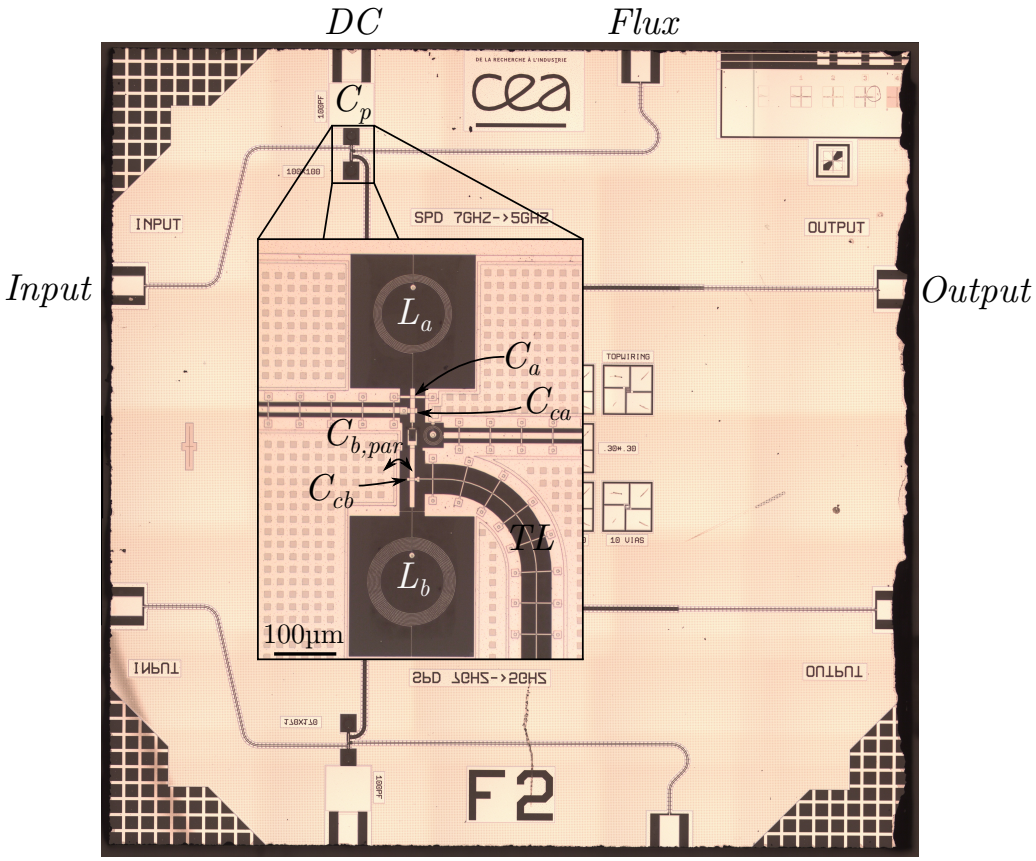

Figure 3.6: Optical microscope picture of a photo multiplier. For the scale, the full chip is 10 mm×10 mm. We represent the designed component and one parasitic capacitance $C_{b,par}$. A similar parasitic capacitance is present for the input resonator.

3.2.4 Impact of parasitic effects

The effect of these parasitic capacitances can be observed in figure 3.7 a), the characteristics of the resonators are given in table 3.4. We observe a strong reduction of the resonance frequency for both resonators and of the bandwidth of the output resonator. Notice that this reduction of the bandwidth decrease the efficiency of the photon multiplication effect, indeed the probability of the reflection of an incoming photon (resonant with a photon multiplication by a factor n) due to low frequency noise in the voltage bias can be written [41]:

$$R \approx \frac{\gamma_T}{\gamma_T + n\gamma_b} \tag{3.2}$$

In our experiment: $\gamma_T = 5.6\,\text{MHz}$ (see section 1.2.2 for its definition and section 4.2.2 for its experimental measure). For a photon multiplication by a factor $n = 2$, the voltage noise leads to 11% of reflection.

The characteristic impedance of the output mode is reduced by 24%. It can be surprising than the characteristic impedance of the input resonator increases. This is due to the growing difference of resonance frequencies which tends to decouple the input and output resonators which limits the impact of the SQUID capacitance. The decrease in the transmitted power through the SQUID capacitance shares the same origin.

From these characteristic, the Josephson energy needed for a photon multiplication with a factor $n = 2$ is 21.0 µeV (or $I_c = 10.2\,\text{nA}$). For a factor $n = 3$, it is 141 µeV (or $I_c = 69\,\text{nA}$). We can note that the diminution of the characteristic impedance is counterbalance with the decrease of resonator bandwidths.

Resonator	Frequency	HWHM $\gamma/(2\pi)$	Impedance characteristic
Input a	6.73 GHz	40 MHz	252 Ω
Output a	4.56 GHz	22 MHz	651 Ω

Table 3.4: Characteristics of the input and output resonators with the parasitic capacitances: $C_J = 4\,\text{fF}$, $C_{a,par} = 6\,\text{fF}$ and $C_{b,par} = 17\,\text{fF}$.

A last potential issue is the higher frequency mode of resonance which can create competing process with the photon-multiplication. Another common way to create high characteristic impedance resonator is to use $\lambda/4$ resonator made from high kinetic inductance materials as described before. However, such resonator possess a resonance for each odd harmonic. Therefore, the conversion of a photon at 7 GHz to three photons at 5 GHz is directly competing with the conversion to one photon at 15 GHz.

This problem was one motive to use LC resonator as they do not possess a third harmonic resonance, nevertheless they also present other resonances. In figure 3.7, we show the first resonance at higher frequency. With its frequency of 21 GHz, it will not create parasitic effects at the working points.

3.2.5 Sample variation

We have presented here a model for a down-conversion device. Up-conversion samples were designed but no working sample was measured. Indeed, the devices measured presented either shunted junctions, shorted transmission lines or asymmetric SQUID preventing to match the Josephson energy for an efficient conversion. Therefore, we will not present this design here. Another important information is that the capacitance C_a, C_{ca} and C_{cb} are fabricated with E-beam lithography. It makes possible to change them in order to modify the properties of the samples without having to fabricate new optical masks.

Conclusion

We first have presented the design and physical implementation of a test sample. It will be used to characterize the experimental setups. We have then presented the design of a photo-multiplier sample and described the impact of the parasitic capacitances extracted

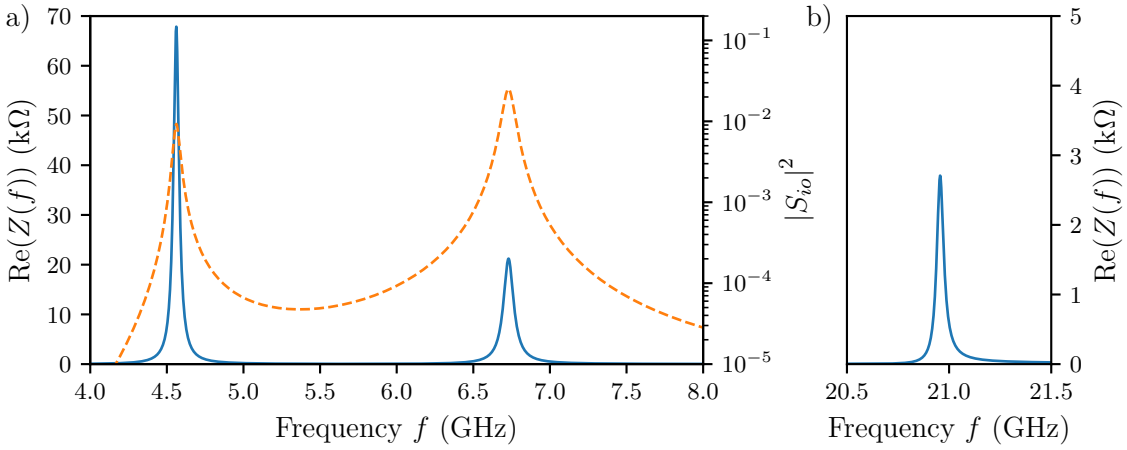

Figure 3.7: a) Impedance and power transmission through a photo-multiplier with parasitic capacitance $C_J = 4\,\mathrm{fF}$, $C_{a,par} = 6\,\mathrm{fF}$ and $C_{b,par} = 17\,\mathrm{fF}$. At the maximum, 2.5% of the power is transmitted through the capacitance of the SQUID. b) Second mode of the output resonator at high frequency. The transmission line is simulated with corrected parameters.

from its actual layout. We have notably highlighted the impact of the unavoidable SQUID capacitance and estimate the Josephson critical current needed to observe photon multiplication processes.

Chapter 4

Experimental setup

Contents

As all modern experiments, the setup can be divided in two parts, the physical implementation with all the electrical components and the software. Only their combination makes it possible to measure a device.

The physical setup is schematically described in figure 4.1. A part of these components are fixed inside a CryoConcept HD200 dry dilution refrigerator with a base temperature of 12 mK. They are shared between the mixing chamber and the second stage of the pulse tube with a temperature of 4 K. All elements are attached with copper bands to thermalize them. The full measurement scheme can be divided in two parts depending on their working frequency. We will begin by describing the high frequency measurement scheme in section 4.1, then the low frequency control of the sample will be discussed in section 4.2.

The other part of the experiment is the software, we can distinguish three main roles:

Experiment control It carries out the hypercube measurement spanned by the controllable parameters (voltage-bias of the junction, frequency of excitation...), collects the results of the measurements and stores them in a structured way.

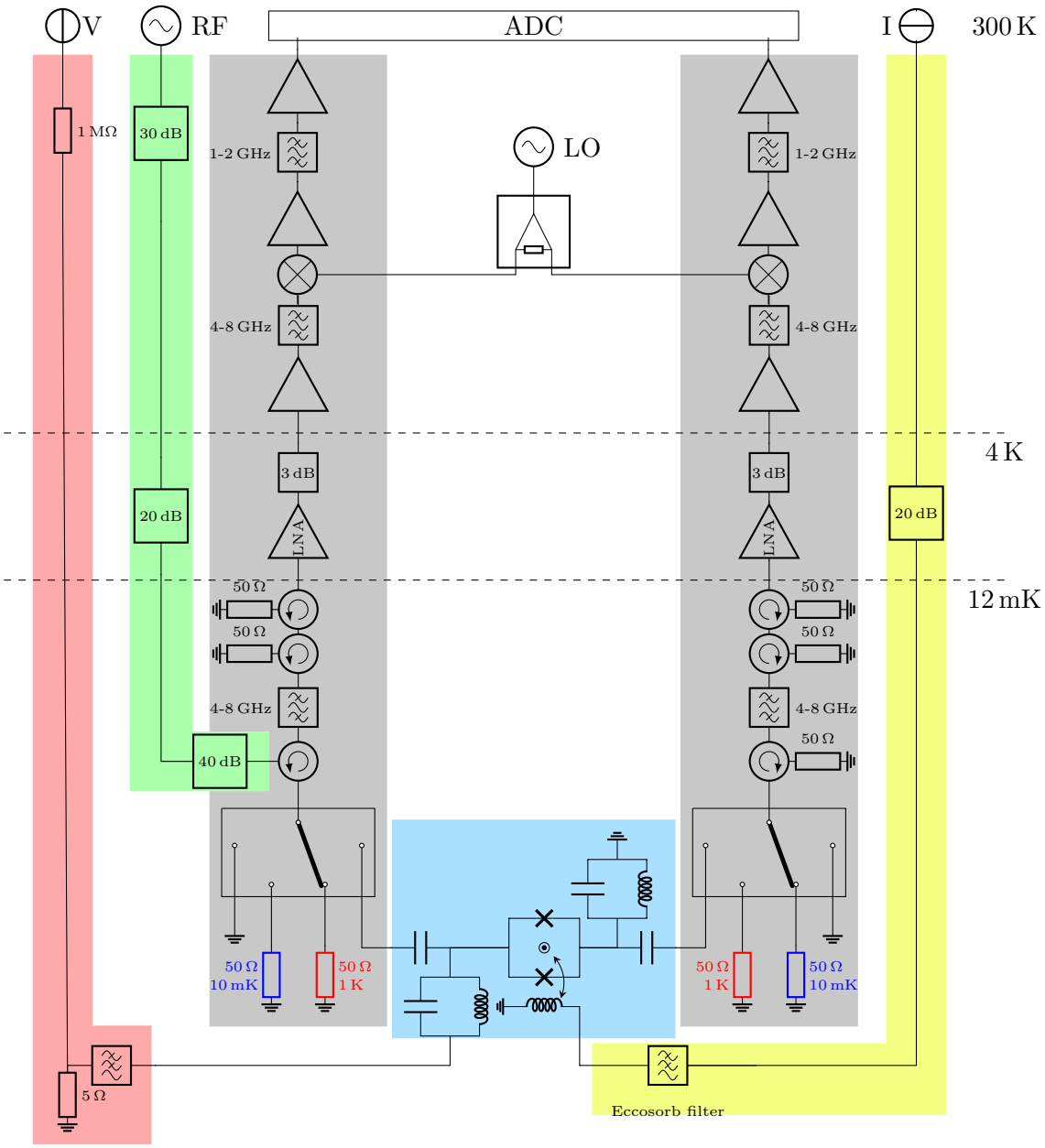

Figure 4.1: Full physical setup. We can distinguish several parts, the first part is the microwave measurement chain in gray. This measurement chain is doubled to measure signal emitted from both sides of the sample in blue. One chain is connected to a microwave input line in green. The microwave setup is discussed in section 4.1. Secondly, the sample is connected to low frequency wiring. The voltage-biasing of the Josephson junctions is represented in red and the flux-biasing of the SQUID is represented in yellow. This low frequency biasing is described in section 4.2.

Real-time analysis As we can see in figure 4.1, the data are acquired through a fast analog to digital converter (ADC). The ADC board is an Alazartech ATS9373 with an acquisition rate of $4\,\mathrm{GS}\cdot\mathrm{s}^{-1}$ which constitutes an impossible amount of data to store. Therefore, the data stream is analyzed through a real time C++ code to extract various information which reduces amount of data by several orders of magnitude. In this thesis, we will focus on the measurement of power spectral densities (PSD). It will be explained in more detail in section 4.1.2.

Offline data analysis In order to observe our data, we need to perform several steps of reconstruction (calibration, averaging...). A dedicated software was developed in the group to perform this task and to project or slice the measurement hypercube for 1d or 2d visualizations.

The control and cold analysis software was developed mainly by Florian Blanchet in python and is described in its PhD thesis [69]. I will not precisely describe this software, however it works similarly to QcoDeS [70].

4.1 Radio-frequency setup

We start by describing the components used for the radio-frequency measurement of our devices, we will then explain how we perform them and how we calibrate the measurement.

4.1.1 Amplification chain

To describe the components used, we follow the measurement chain from the sample to the ADC board. This is the gray area in figure 4.1. The measurement chain is designed to work in the C-band (4 GHz to 8 GHz). The first element is a 6 port latching switch from Radiall (R591-763-600) which makes possible to connect several samples for a single cooldown (up to 3 photo-multipliers) and to perform microwave calibration (see section 4.1.3 and section 4.1.5). The common port of the switch is connected to a Raditek cryogenic circulator (RADC-4.0-8.0-Cryo-S21-qWR-M2-b) which can be used to shine signal to the sample for one channel. This circulator, in conjunction with a 4-8 GHz pass-band filter from Microtronics (BPC50403) and two circulators (identical to the first), prevents amplifier noise from reaching the device. This isolation stage is connected to an amplifier from Low Noise Factory (LNF-LNC4_8C) at the 4 K stage through niobium-titanium coaxial cable from Coax Co. (SC-219/50-NbTi-NbTi). Then a 3 dB cryogenic attenuator from XMA is added to prevent stationary wave to occur between the 4 K and room temperature amplifiers.

We reach the room temperature electronics with cupronickel coaxial cables from Coax Co. (SC-219/50-CN-CN). The first element is a low noise amplifier from Miteq (AMF-5F-04000800-07-10P) and the signal is then filtered by a custom 4.25-7.75 GHz pass-band filter from Microtronics. The signal is then down-mixed with a mixer from Marki (MM1-0312S) with a local oscillator coming from a Rohde Schwarz source (SMF100A with high power output option) which is divided through an AA-MCS power splitter (AAMCS-PWD-2W-2G-18G-10W-Sf) to supply both measurement chains. The down-converted signal is amplified with a 0.95-2.15 GHz amplifier from Minicircuits (ZRL-2150+) then the signal is

filtered with a custom 1.1-1.9 GHz pass-band filter from Microtronics. Finally, the signal go through two amplifiers from Minicircuits (ZX60-V62+) and is digitized by an Alazartech (ATS9373) analog to digital converter board. We will now discuss the treatment of the digitized data to extract the relevant measurements.

4.1.2 Power spectral density measurement

It is important to note that the signal is hidden in the amplifier noise, indeed the signal-to-noise ratio is between $-10\,\mathrm{dB}$ and $-30\,\mathrm{dB}$ depending on measurements. Therefore, all of them are made in two steps, we first repeatedly turn on and off the signal (from 1 s to days) with a period around 1 s, secondly we average the difference of these measurements to extract the part of the signal coming from the sample from the amplifier noise. Most spectrum analyzers possess limited real time bandwidth for real time averaging which makes them useless for this measurement task.

We are using an ADC board with a sampling rate of $4\,\mathrm{GS}\cdot\mathrm{s}^{-1}$ or $2\,\mathrm{GS}\cdot\mathrm{s}^{-1}$ on 2 channels, therefore we are not able to directly measure the power spectral density through the full measurement range 4 GHz to 8 GHz. That is why, we down-convert a 1 GHz slice of this frequency band to the second Nyquist zone of the ADC with the mixer and the 1.1 GHz to 1.9 GHz pass-band filter. By varying the local oscillator (LO) frequency over several measurements, we can reconstruct the signal in the C-band.

The local oscillator frequency (f_{LO}) must be careful chosen, indeed three situations are possible (see figure 4.2 for a visual explanation):

- LO frequency 3-5 GHz: the band of measurement is 4-7 GHz.
- LO frequency 5-7 GHz: the low frequency and high frequency part of the 4-8 GHz measurement band overlap. Therefore, these LO frequencies cannot be used.
- LO frequency 7-9 GHz: the band of measurement is 5-8 GHz.

The transition between the stop band and the pass band of the filter are not perfectly sharp. Therefore, to prevent aliasing, the local oscillator frequency is chosen in the ranges 3-4.5 GHz and 7.5-9 GHz.

After this down-conversion scheme, the signal arrives in the ADC board which discretizes it over 12-bits. This ADC board is configured through our python control software but it cannot directly absorb the $6\,\mathrm{GB}\cdot\mathrm{s}^{-1}$ of generated data.

We will now describe how the real-time C++ analysis schematically works. The board streams the data in real time to the computer memory through buffers of fixed length. The data are continuous in each buffer and the buffers are received in the order of measurement. They can be treated independently of each other, so they are divided over a pool of threads to analyze them on all cores of the host computer in parallel.

The first operation of each thread is to convert the data from their binary representation to an array of 32-bits floats for both channel (S_1 and S_2). Then we correct the crosstalk of the ADC board with a finite impulse response (FIR) filter:

$$S_1[k] = S_1[k] - \mathrm{FIR}_1(S_2)[k] \tag{4.1}$$

where the FIR filter possesses 16 coefficients (taps) for each channel. This correction reduces the crosstalk by a factor 10 in amplitude, or 20 dB in the power spectral densities. The next step is to estimate the power spectra, this is done with the Bartlett's method

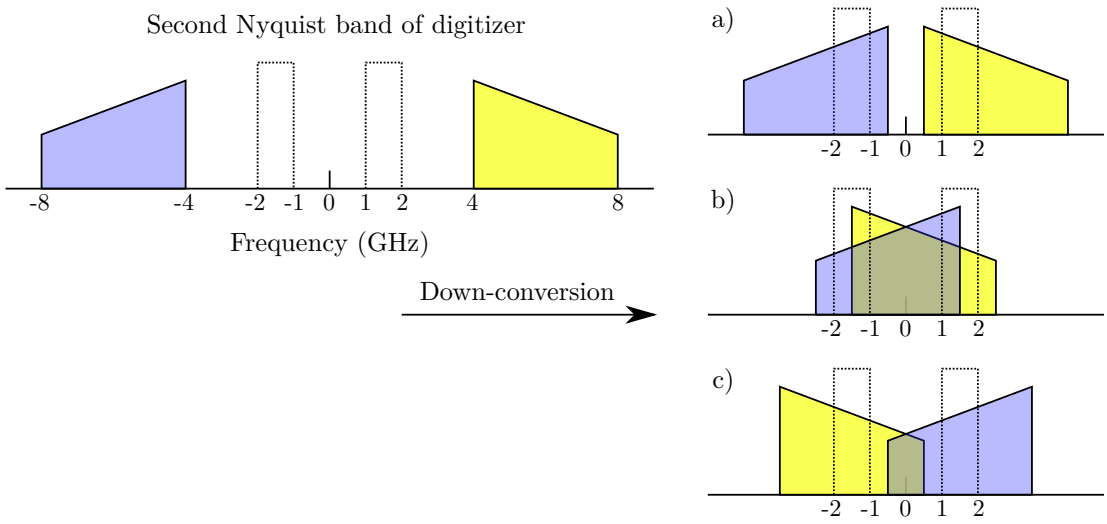

Figure 4.2: Effect of the down-conversion of the 4-8 GHz signal to the band of measurement. Depending on the local oscillator frequency, the measured frequencies change. The insets a) (f_{LO}=3.5 GHz) and c) (f_{LO}=7.5 GHz) show the operating principle of the down-conversion scheme. The inset b) (f_{LO}=5.5 GHz) illustrates the effect of a badly chosen local oscillator frequency: two different frequencies of the signal are converted to the same frequency in the base band of our measurement scheme.

[71]. The buffers are then divided in segments from which a periodogram is computed. The periodograms are added up by each thread. At the end of the acquisition, the accumulators of all threads are gather together and send back to the python code, which normalizes them by the number of points used.

To measure the power spectral density over the full measurement range, we measure the PSD with 6 different LO frequencies. The measurement bands are overlapping which allows us to throw away the border of each measurement which are affected by aliasing. Finally, we join the different measurements, however the stitching is only smooth if the gain of the full acquisition chain is identical for all signal frequencies and LO frequencies. So to reconstruct the full signal, we need to calibrate the amplification chain.

4.1.3 Calibration of the amplification chain

As presented in the figure 4.1, the first element of the amplification chain is a microwave switch. To calibrate the noise and gain of the amplification, we apply the standard Y-factor method [68]. To do so the switch is connected two 50 Ω loads which are thermalized at two different temperatures. The first one is anchored to the mixing chamber and the second one is attached with a copper bands to the still at 900 mK. The difference between the emission of the two loads allows us to extract the gain and the noise of the amplification chain. Indeed, the noise power density of a match load at a temperature T is given by [72, 73]:

$$S_{P,e}(T, f) = \frac{hf}{2} \coth\left(\frac{hf}{2k_B T}\right) \tag{4.2}$$

Notice that it can be inferred using the Caldeira-Legett [36] or the input/output theory [38].

An amplifier is characterized by it gain $G(f)$ and noise temperature $T_N(f)$. The measurement $S_{P,m}$ of the power spectral density emitted by a load at a temperature T after an amplifier is given by:

$$S_{P,m}(T,f) = G(f)[S_{P,e}(T,f) + k_B T_N(f)] \tag{4.3}$$

From the measurements of two loads at different temperatures, we can deduce the gain and the noise temperature of the amplification chain:

$$G(f) = \frac{S_{P,m}(T_{Still},f) - S_{P,m}(T_{MC},f)}{S_{P,e}(T_{Still},f) - S_{P,e}(T_{MC},f)} \tag{4.4}$$

$$T_N(f) = \frac{1}{k_B}\frac{S_{P,e}(T_{Still},f)S_{P,m}(T_{MC},f) - S_{P,e}(T_{MC},f)S_{P,m}(T_{Still},f)}{S_{P,m}(T_{Still},f) - S_{P,m}(T_{MC},f)} \tag{4.5}$$

In figure 4.3, we show the typical gain and the noise of the full amplification chain. This calibration is performed at each cooldown of the experiment. From the specification of the amplification, and the attenuation added to prevent stationary waves, we expect a gain of 100 dB. The measured gain is a bit lower due to loss in the coaxial cables. The strong discontinuities at the change of local oscillator frequencies can be a bit surprising, they come mainly from the If bandpass filter and amplifiers of which the gain decreases with frequency (for f_{LO} >7.5 GHz the frequency band is inverted, hence the symmetrical form from f_{LO} <4.5 GHz).

These discontinuities are not visible in the noise temperature, which is primarily fixed by the noise of the first amplifier. However, the specified noise temperature of it is below 3 K, so the measured noise is significantly higher than the specification. This increase in noise comes first from the attenuation before the first amplification, due to the three circulators, the band pass filter, the microwave switch and the microwave cables. They have an insertion loss of at least 3 dB. This increases the noise temperature for a factor 2 [68]. The noise from the others amplifiers can be held for the remaining difference.

4.1.4 Calibration drift

In order to verify the accuracy of the calibration, we repeat the calibration after several weeks to account for the variation of the microwave components with time. We show in figure 4.4, the gains and noises of the full measurements chain which were measured at an interval of three weeks.

These calibrations are clearly similar. However, the noise is much more stable than the gain of the chain. The logarithmic scale of the gain axis is misleading when we compare the changes between these measurements. Indeed, the gain changes by 6% in average, whereas the input added noise changes by 0.7% only.

As we already explained, we measure the power spectral density of our device with the bias voltage turned on and off, and we record these two measurements. The off-measurements are directly linked to the noise of the amplification chain at the moment of the measurement. Therefore, by using these off-measurements and the calibration of the

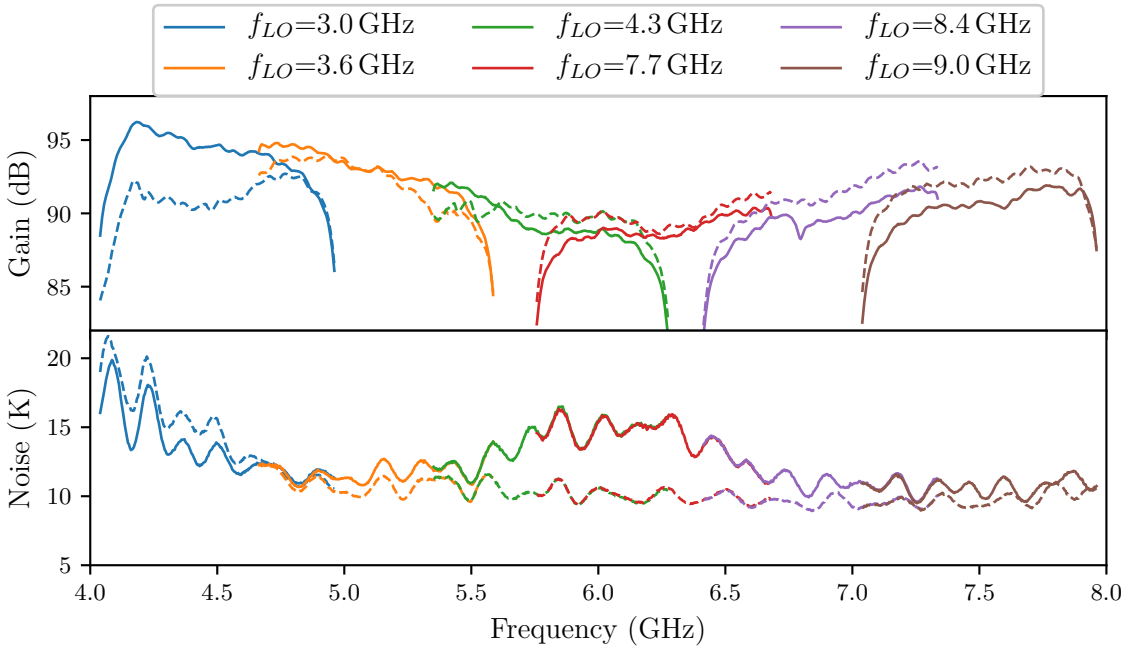

Figure 4.3: Gain and noise of the amplification chains for six local oscillator frequencies. The dashed line is the calibration for the right amplification chain in figure 4.1, while the filled line is the calibration for the other chain (connected to the input RF line).

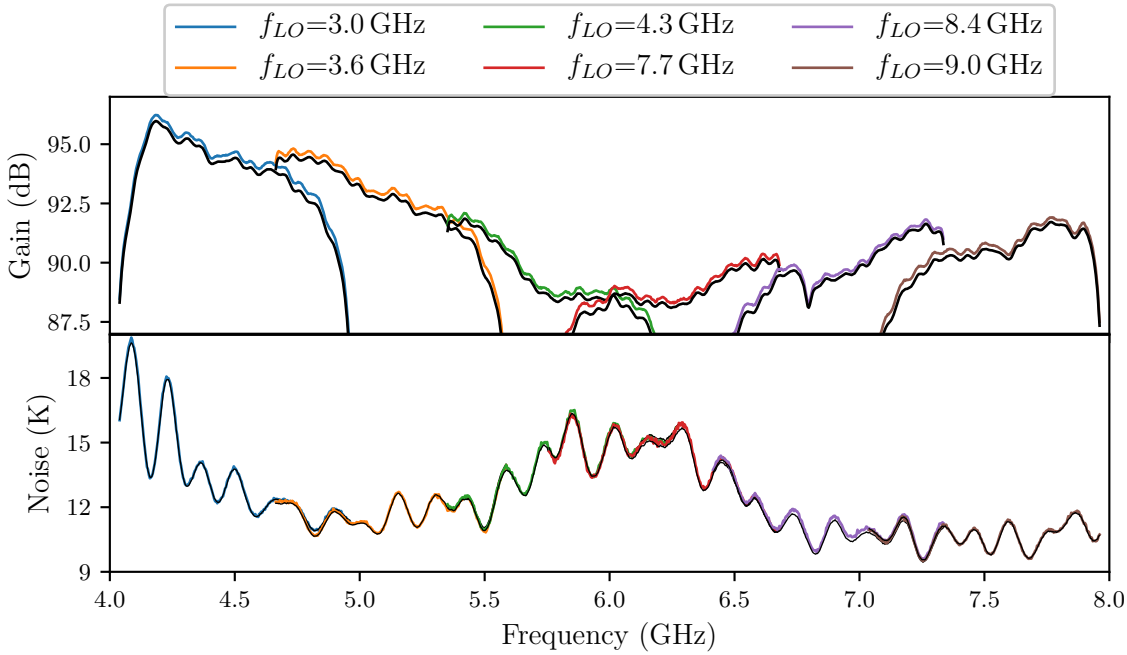

Figure 4.4: Gain and noise of the amplification chains for six local oscillator frequencies, the colored calibrations are performed three weeks before the black calibration.

noise of the amplification chain, we can extract the gain and apply it to calibrate the power spectral density of our devices, as the input added noise of the amplification chain is nearly constant.

In figure 4.5, we show the off-measurement of a device as a function of time and temperature of the first radiation shield. We observe that these two measurements are strongly correlated. The variation of the amplification chain is therefore mainly due to the change of the ambient temperature. These gain variations are coherent with the specifications of the amplifiers used.

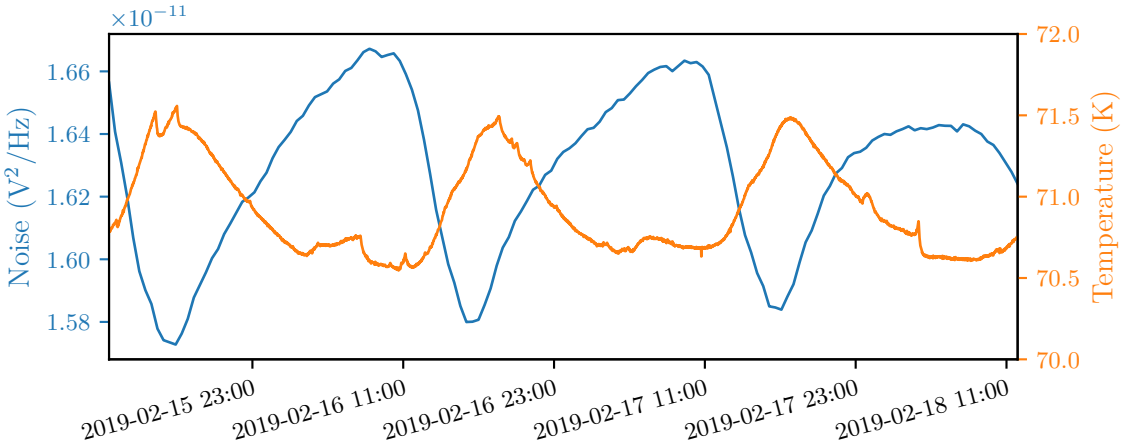

Figure 4.5: Power spectral density at 4.8 GHz at the output of the measurement chain measured with an inactive sample (zero bias voltage) as function of time. On the right, we show the temperature of the first radiation shield which is anchored to the first stage of the pulse tube. This temperature is strongly correlated with the ambient temperature through thermal radiation. Note that the laboratory is facing west and takes the sun in the afternoon.

Using this calibration of the amplification chain, we will now be able to calibrate the attenuation of the input line and thereby complete the calibration of the radio-frequency setup.

4.1.5 Calibration of the drive lines

The radio-frequency input line (in green in figure 4.3) is made of Coax Co. cupronickel coaxial cable (SC-219/50-CN-CN) and cryogenic attenuators from XMA (2082-6418-dB-CRYO series). This line is driven by a microwave source from Keysight (E8257D). We place the cryogenic attenuators at different temperature stages in order to thermalize the input field to low temperature and so to prevent thermal radiation to interact with the sample [74]. Notice that this thermalization is limited by the use of attenuators not designed for millikelvin temperatures [75–77].

To calibrate the input radio frequency line, we connect the switch to the microwave short. We send microwave radiation with the RF source and measure the output power with the ADC board. Therefore, we can easily deduce the input attenuation with the calibration of the amplification chain. The result is presented in blue in figure 4.6. We measure an

attenuation of −100 dB which is good agreement with the −90 dB from the attenuator and −10 dB coming from the cable. Notice that this attenuation is not extremely precise as the level accuracy of the microwave source is given to ±0.9 dBm for the C-band of frequency.

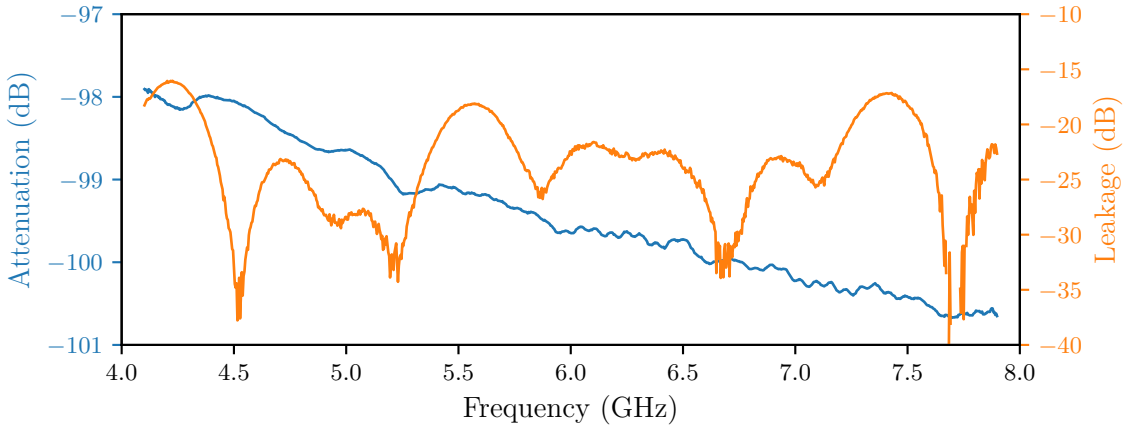

Figure 4.6: Attenuation of the input line in blue (on the left) as a function of the measurement frequency. It is measured with the switch connected to the short. On the right, we plot the leakage from the input line to amplification chain in orange. For this measurement, the switch is connected to the cold load.

By connecting the switch to the cold load and measuring the reflection from the input RF line, we can measure the direct leakage from the input line to the amplification chain. We show the measure in orange in the figure 4.6. The leakage is below −15 dB for all frequencies and −20 dB for most of them. This is coherent with the isolation specified for the cryogenic circulator (−18 dB). Therefore, it gives us a limitation on the input return loss we can measure for our samples.

The reference plane of this calibration is the output port of the switch, we have verified that all output port to be equal within measurement accuracy. However, the loss between the switch and the sample cannot be calibrated with this method. To estimate the loss to the sample itself, we can use its reflection properties. Indeed, the sample reflects nearly all power outside of the bandwidth of the input resonator. In figure 4.7, we observe that the reflection suffers an attenuation of −0.6 dB which is coherent with the attenuation of a 25 cm coaxial cable (the microwave crosses it two times).

Both methods are interesting as the calibration to the switch characterizes the performance of the system as an ensemble, while the calibration to the sample allows us to characterize the efficiency of the process occurring in the sample.

4.1.6 Sample holder

The last part of the radio-frequency experiment is the sample holder. Indeed, we need to couple the sapphire chip to the measurement coaxial line. We present the sample holder in figure 4.8, the coupling is done in two steps. First, the SMA connectors (from Southwest Microwave) are connected to a pin which is soldered to a grounded coplanar waveguide. Then these lines and the ground are connected to the sapphire chip through a dense array

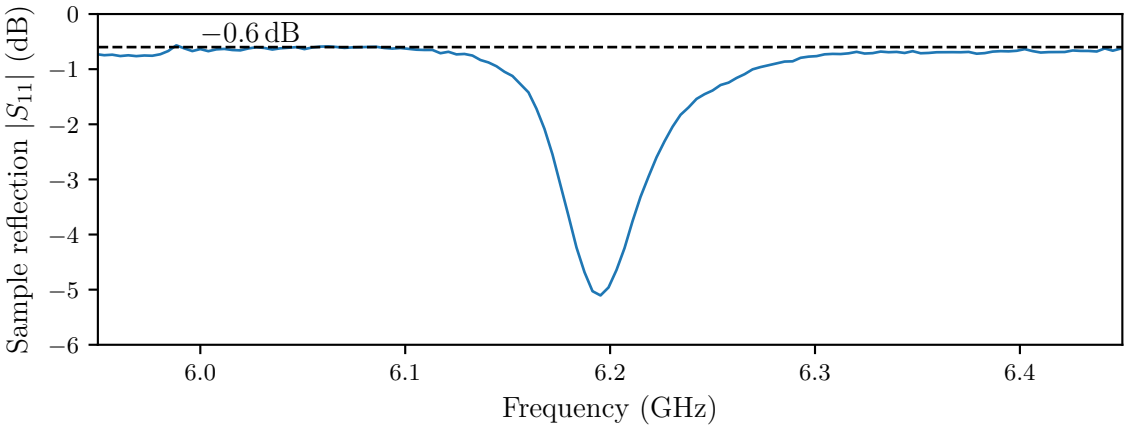

Figure 4.7: Input return loss of the sample as a function of frequency. The reflection outside of the resonator bandwidth is flat, and the loss corresponds mainly to the attenuation in the cable between the sample and the microwave switch.

of wedge wire bounds. A hole exists under the sample to limit slot line modes between the groundplane of the sample and the box.

Note that two electronic components are soldered inside the sample holder. These components are part of the biasing circuit which we will now discuss.

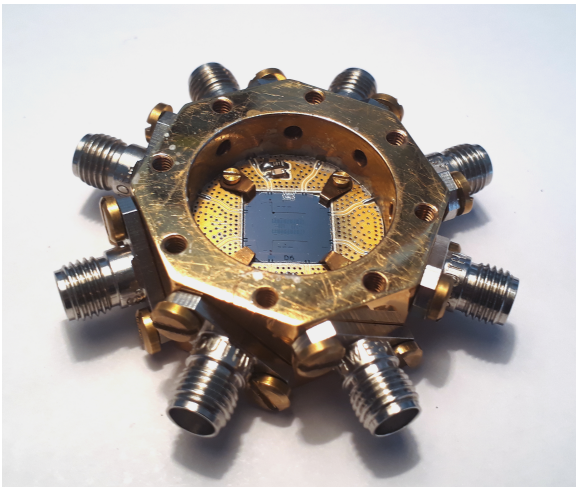

Figure 4.8: Picture of the sample holder used in this thesis. Inside of it, we can recognize a photo-multiplier sample.

4.2 Biasing of the SQUID

As we explain in the chapter 1 and chapter 3, our sample needs to be biased with two low frequency lines. First, we need to impose a flux through the SQUID to adjust its Josephson energy. Secondly, we need to voltage-bias the SQUID itself to provide the energy vital to the emission of radiation.

4.2.1 Flux biasing

The flux-biasing of the SQUID is performed with the yellow part of figure 4.1. A source measurement unit of Keysight (B2962A) supplies the current to a −20 dB cryogenic attenuator at 4 K, so a tenth of this current is supplied to the sample through an Eccosorb low-pass filter. We need to supply a current of 500 µA through the flux biasing loop to put a flux quantum in the loop of the SQUID. This current is not negligible at dilution temperature and prevent us from adding more attenuation in the flux-line because of the dissipated power. The use of a radio-frequency attenuator is not ideal for a flux line, as it possesses a high current noise due to its low impedance. However, we prefer to keep the possibilities to drive fast flux pulse which are useful for some experiments of the group [2].

Nevertheless, we need a relatively low flux-noise, that why we added a low-pass frequency filter. Due to the high current, low dissipation at DC is required, as it is thermalized with the mixing chamber. Lots of cryogenics filters were studied [78, 79], notably to explore mesoscopic devices where high frequencies heat electrons. The Eccosorb filters were chosen for their relatively simple fabrication and good RF performance.

The Eccosorb filter are made from RG-402 copper cable (coaxial cable with an outer diameter of 3.6 mm) from which the center conductor and the insulating materials are removed. We replace the center conductor with a copper wire of diameter 0.5 mm and the insulating materials with Eccosorb CRS124 PTA. The Eccosorb is a silicone rubber loaded with small particles of iron which absorbs microwave radiation. The last step is to solder the connector. To adjust the cut-off frequency, we only need to change the length of the filter. For a 100 mm filter, the typical radio-frequency performance is plotted in figure 4.9. The −3 dB point is around 400 MHz and we reach the ground floor of the Vector Network Analyzer (E5071C from Keysight) for frequency higher than 3 GHz. One big advantage of this filter is their reflection properties as the return loss stays under −10 dB up to 20 GHz.

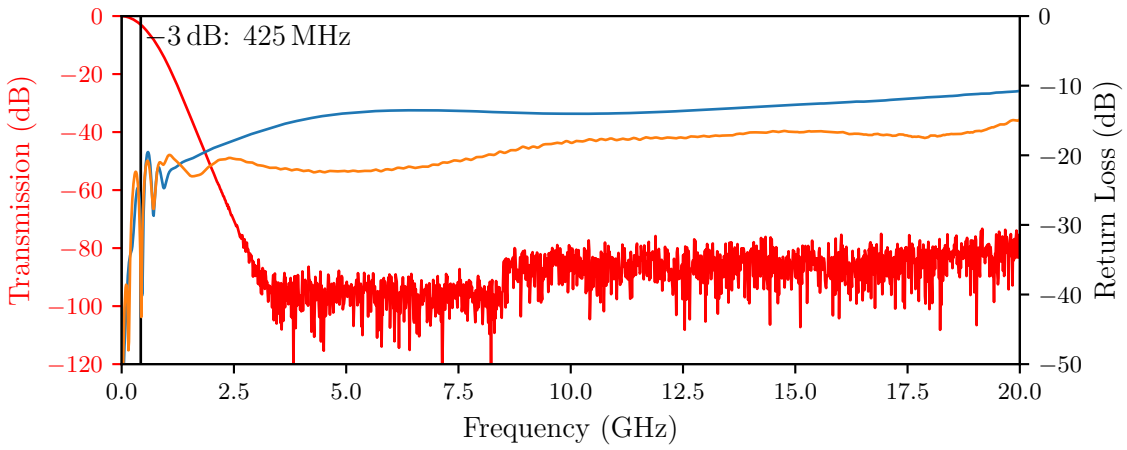

Figure 4.9: On the left in red, the attenuation of a 100 mm Eccosorb filter as a function of the frequency. On the right, the return loss from the two sides of the filter (in blue and orange). The maximum input return loss of the filter is around −10 dB at 20 GHz.

The simplicity and the radio-frequency performance are a big advantage compared to other filters using Eccosorb [80, 81].

4.2.2 Voltage biasing

The voltage-biasing circuit is one of the most sensitive parts of the experiment, indeed it is very strongly coupled to the SQUID and any noise modifies the emission properties of the device. In figure 4.1, the biasing circuit is represented in red. The first element is a source measure unit from Keysight (B2962A) which polarizes a voltage divider with a high valued resistor (1 MΩ) at room temperature and a small one (5 Ω) at low temperature through a low noise cable. It is a triaxial cable with graphite between the conductors and the insulating materials to limit the apparition of triboelectric noise from the pulse tube vibration [82].

To filter the noise which couple through the voltage divider or which can be generated by itself, a low-pass filter is inserted after the polarization resistor at low temperature. Because of the high impedance of the wiring, the sample only sees the impedance of the polarization resistor and the low-pass filter. Therefore, we will concentrate ourself on these elements.

4.2.2.1 Constraints on the biasing circuit

As the biasing circuit is strongly coupled to the sample, the first requirement is the absence of resonance. These low-frequency resonances easily possess high characteristic impedances, therefore they can have a strong impact on the sample, as the emission of high-frequency photons will be associated with low-frequency photons. In other words, these resonances will create replicates of the main photon emission lines.

Secondly, as explained in the chapter 1, the impedance at low frequency broadens the emission lines, mainly due to its Johnson-Nyquist noise. As a reminder the photon emission rate can be written for the first emission line:

$$PSD(V, \omega \approx \omega_0) = r\mathcal{L}[\omega, \omega_0, \gamma] \frac{E_J^2 e^{-r}}{\hbar^2 \omega} \frac{2\gamma_T}{\gamma_T^2 + \left(\pi \frac{2eV}{\hbar}\right)^2} \tag{4.6}$$

If we measure the PSD at a fixed pulsation ω and vary the voltage, we observe a Lorentzian with a full-width at half maximum (FWHM) of $2\gamma_T$ ($\gamma_T = \pi\rho k_B T/\hbar$). As we discuss in the chapter 3, the FWHM must stay small compared to the bandwidth of the input and output resonator to not decrease the conversion efficiency of the photo-multiplier.

Finally, the impedance at zero frequency can create instabilities when the current through the junction increases. This effect is not described in the $P(E)$ theory as the treatment is pertubative, but the photo-multiplier operates outside of this limit. These instabilities were observed several times with polarization circuits of impedance 50 Ω and 25 Ω in the group.

4.2.2.2 Previous biasing circuits

We can take advantage of equation (4.6) to measure indirectly γ_T without additional perturbation, as we do not need to modify the setup. Moreover, this method has a very high sensitivity allowing to easily measure nanovolt noise. The previous work inside the group [5, 44, 45] measured voltage fluctuation of 100 $\mathrm{nV_{RMS}}$ corresponding to 100 MHz FWHM.

This is intolerable for the measurement of the photo-multiplier as the bandwidth of the input and output resonator is of the same order of magnitude.

Moreover, these measurements highlight significant higher environmental temperature than the base temperature of the dilution temperature (or additional voltage noise). This shows that the filtering of parasitic signal and the cooling of the resistors inside the filter were imperfect. Notice that it is very complicated to cool the electrons of the resistor as the coupling between the phonon and the electron decreases rapidly at very low temperature. The last issue was the presence of additional resonances, which we hope to reduce by including the bias-T directly on the chip.

4.2.2.3 Global structure

The schematic of the filter is presented in figure 4.10, notice that the colors split the schematic as a function of their place in the experiment. To explain its operation, we start with the input of the biasing circuit, I+ and I-. The biasing current goes through a common mode choke before the I- is connected to the ground, this prevents ground loops and limits common mode noise. Then the current I+ goes through a 5 Ω resistor to be converted into a voltage. This voltage crosses a silver-epoxy filter which absorbs frequency higher than 10 MHz and thermalizes the wire (the 5 Ω resistor becomes hot for high bias voltage), more details are given in next part. We add a discrete components filter which fulfills two goals. First, it stops frequency higher than 10 kHz, secondly it presents a relatively flat impedance of 5 Ω from the sample side up to 320 MHz where it goes smoothly to zero up to tens of gigahertz. The details are given in a subsequent part.

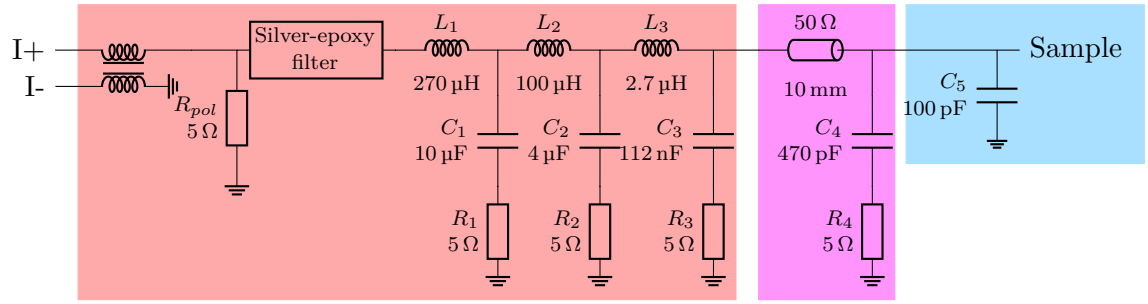

Figure 4.10: Schematic of the biasing circuit, this circuit is fixed to the mixing stage. It is divide in three parts, the first in red is put inside a copper box and links to the sample holder through an SMA connector. The part in purple is put inside the sample holder and the capacitor in the blue part is put directly on the chip of the device.

4.2.2.4 Silver-epoxy filter

The silver-epoxy filter [83] absorbs high frequency noise and limits the heating of the matching resistor (R_1, R_2...). The high frequency noise comes from two sources, first the noise which arrive through the wiring and secondly, the self emission from the polarization resistor, as the electron temperature increases to several hundreds of millikelvin due to the biasing-current [84]. Therefore, its radiation needs to be absorbed to thermalize the

electromagnetic field at the base temperature, otherwise the broadening of radiation will be at least one order of magnitude bigger.

Filters made from discrete elements always suffer from their parasitic characteristics. Typically, the rejection of a low-pass filter decreases at high frequency due to parasitic coupling. This prevents us to use them as the spontaneous emission of the polarization resistor extends to tens of gigahertz. A silver-epoxy filter is made from a long thin wiring which is surrounded with a conductive medium (silver-epoxy). When an ac-current goes through the wire, Eddy currents are created inside the silver epoxy which dissipate the energy of ac-current. The attenuation is globally proportional to f^2 and does not decrease at high frequency. This filter, as the Eccosorb, works by absorbing the energy of high frequency radiation.

In practice, 12 m of a superconducting wire (niobium-titanium wire with a shell of cupronickel) with a diameter of 0.15 mm is wound onto four coils. It is important to note that we want to keep the resistance of this wire negligible compared to the polarization resistor, hence the superconducting wire. During the winding, the silver-epoxy (Epo-Tek E4110) is continuously deposited on the varnish of the wire. Therefore, the wire is fully embedded in the conductive epoxy. The four bobbins are coiled with alternative directions to prevent low frequency field (typically 50 Hz) to magnetically couple to the biasing circuit. Finally, these coils are cast in silver epoxy in a cavity between the polarization-resistor and the discrete elements filter to prevent all radiation to directly leak from one to the other. The result can be seen in figure 4.11.

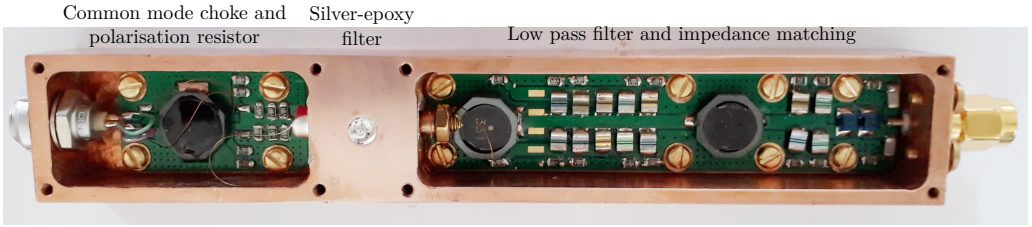

Figure 4.11: Physical implementation of the voltage-biasing circuit in a copper box. We observe three parts, the cavity on the left receives the polarization resistor and the cavity on the right receives the discrete filter and matching circuit. Between them, the silver-epoxy filter is embedded in a hole which is filled with silver epoxy. A copper lid with an indium seal is added to prevent noise from leaking from the input cavity to the output cavity.

These filters were not tested individually, however from the original proposition [83] of silver-epoxy filter, we can estimate that their cut-off frequency is of the order of tens of megahertz. To stop frequency lower than that, we use a filter made from discrete components.

4.2.2.5 Low frequency filtering and impedance matching

The realization of discrete elements filter at dilution temperature is complicated, as the properties of electrical components change with temperature. Several studies of their low-temperature behavior exist [85–89]. We can deduce general guideline from them:

Resistor Thin film resistors made of nichrome are very stable. We do not use tantalum nitride resistors as they become superconducting at low temperature.

Capacitor NP0 or C0G are very stable but only available for capacitance below 100 nF. Acrylic film capacitors are relatively stable and available up to 22 µF.

Inductor Several magnetic materials are stable at low temperature but they are not very easily available. Several ferrite power inductors are relatively stable but need testing. For small values, air coils are very stable as their values are fixed by the geometry.

The components used in figure 4.10 are described in table 4.1. The variation of their values between 300 K and 4 K is given where we have measured it ourself, the other components are chosen because of the stability of the technology used for their fabrication. Notice that the filter and matching network are divided in several stages because the parasitics of the components. For example, the 1 µF capacitor used for the filter adopts an inductive behavior for frequency above 10 MHz.

Component	Technology	Reference	Change at 4 K in %
R_{pol}, R_1, R_2, R_3	Nichrome thin film	RR1220 (Susumu)	1
R_4	Nichrome thin film	CPF0603B4R99E1 (TE Connectivity)	Not measured
C_1, C_2	Acrylic film[1]	FCA1210C105M-G2 (Cornell Dubilier)	-15
C_3	C0G	GCM31M5C1H563JA16 (muRata)	Not measured
C_4	C0G	VJ0603A471JNAAO (Vishay)	Not measured
C_5	On chip		Not measured
L_1, L_2	Ferrite power inductor	744066331, 744065121 (WE)	-18
L_3	Air coil	1008CS-272XJLB (Coilcraft)	Not measured

Table 4.1: Components used for the fabrication of the discrete-components filter described in figure 4.10.

[1] Similar capacitors from Rubycon (PMLCAP) were tested by Hugo Therrien in the University of Sherbrooke. The stability is similar but are available up to 22 µF.

4.2.2.6 PSD broadening results

The best way to test the biasing circuit is to use it with an actual sample. To do so, we have designed a device, described in section 3.1, to test it independently of the photo-multiplier device. In figure 4.12, we plot the power spectral density at a fixed measurement frequency as function of the bias voltage.

The top measurement measures the broadening of the emission line due to voltage fluctuations. From previous measurements, we know that the pulse tube induces a lot of voltage-noise. So first we concentrate on the curve with the pulse tube turned off. The emission has a near perfect Lorentzian shape with a HWHM of $\gamma_T = 2.23\,\mathrm{MHz}$ which corresponds to an electronic temperature of the biasing circuit $T_e = 22\,\mathrm{mK}$. This temperature is near the temperature 13 mK of the fridge during this measurement, the difference comes probably from the not perfectly thermalized resistors. The second measurement was done with the pulse tube working, therefore it better represents the performance of the biasing circuits in actual experiments. The measured electronic temperature $T_e = 55\,\mathrm{mK}$ ($\gamma_T = 5.55\,\mathrm{MHz}$) is significantly higher than the fridge temperature and the previous measurement. Moreover, we observe that the curve is not a perfect Lorentzian. We can attribute these effect to a voltage noise induced by the vibration of the pulse tube which is imperfectly filtered, as this voltage noise is probably not Lorentzian but as a similar spectrum than the fridge vibration.

The bottom measurement is done over a larger sweep of the biasing voltage and plotted on logarithmic scale. We observe the same peak as before and two additional peaks. They come from low frequency (100 MHz) resonance which couples with the system. It is probably a small resonance in the biasing circuit, but we cannot be perfectly sure from this measurement alone.

Conclusion

With the experimental setup described here, we have all we need to accurately measure the photo-multiplier as described in the next chapter. These results will be mainly constituted of PSD measurements which are calibrated with the methods presented in this chapter. Moreover, we know that the voltage-fluctuations from the biasing circuits are not problematic as their amplitude is much smaller than the bandwidth of the resonators. The previous version of the biasing-circuits would have been unusable due to its excessive voltage noise.

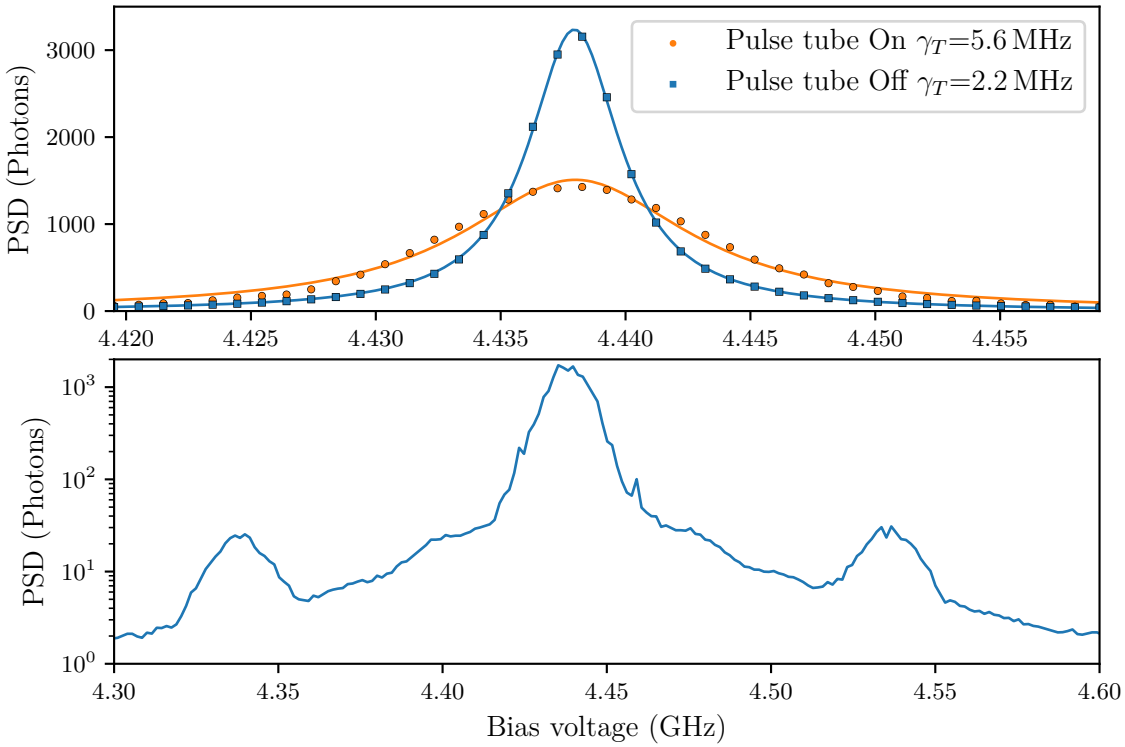

Figure 4.12: Power spectral density as a function of bias voltage at a frequency of 4.438 GHz. The sample is described in section 3.1. In the top pannel, we observe the broadening of the main peak due to bias-voltage fluctuation. The full lines are fits of Lorentzian with half width at half maximum γ_T whereas the points are the measurements. In the bottom panel, we observe the main peak of emission, as well as two side lobes of emission due to a resonance at 100 MHz. The pulse tube was continuously working for this measurement.

Chapter 5

Experimental results

Contents

We will now discuss the experimental results obtained from the sample presented in section 3.2. We first measure the spontaneous emission, from which we can deduce much about the characteristics of the sample. Secondly, we apply microwave radiation in order to evaluate its scattering properties, more precisely the photo-multiplication effect. This sample is the first and only fully functional device and was measured at the beginning of 2019, its critical current is 6 nA at 4 K.

5.1 Spontaneous emission

To limit the number of variables, we will start by extracting as much information as possible from the spontaneous emission of our device. We will measure first its behavior at low Josephson energy where the $P(E)$ theory is valid and extract important parameters. Then we will discuss the impact of the flux in section 5.1.2. Finally we will work with the emission at high Josephson energy, we will notably observe new phenomena as simultaneous tunneling of several Cooper pairs.

5.1.1 Emission at low Josephson energy

We start by describing the power spectral density emitted by our sample, then we estimate the parameters of our system, resonance frequencies, resonator bandwidths and characteristic impedances. We will see that several methods can be used for this estimation with advantages and drawbacks for each one.

5.1.1.1 Power spectral density

The power spectral density is the fundamental measurement of our experiment. All other curves are extracted from it and contain less information. In figure 5.1, we show the power spectral density for both sides of the sample (input and output) as a function of the bias voltage and the frequency of emission (or measurement). Notice the logarithmic scale, it is cut for low emission rate as we arrive at the noise floor of this measurement for a power spectral density lower than 0.01 Photon. The typical duration of these measurements is a few days.

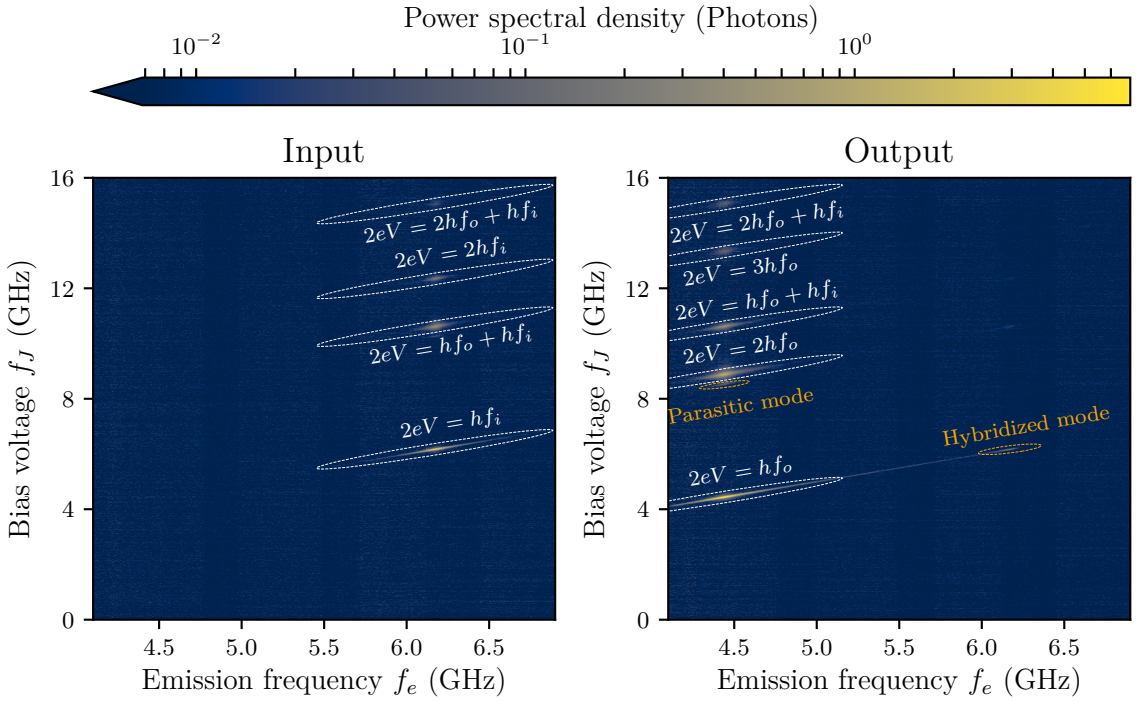

Figure 5.1: Power spectral density as a function of the frequency of emission and of the bias voltage. On the left, we show the measurement from the input side and on the right, the measurement from the output side. For each emission peak, we indicate to which process it corresponds in white. In orange, we indicate parasitic effects.

We can identify several processes in this measurement. First we observe strong emission for the fundamental modes of emission where the tunneling of a Cooper pair gives rise to one photon inside the input or output resonator. Secondly, we can identify the other emission lines with higher order, where one Cooper pair gives rise to two or more photons inside the resonators. Finally, we observe a simultaneous emission on both resonators from the

tunneling of one Cooper pair. All emission lines have a slope of 1 which indicates that the emission is due to the tunneling of one Cooper pair for every process.

The simultaneous emission process can present non-classical correlation between the photons emitted on each side [21]. We did not measure their cross-correlation function, as their measurement requires a long time to achieve a good signal over noise ratio (second-order correlation function measurement). Moreover, the physical and software setups need slight modifications to perform it.

Other unwanted phenomena can be observed in figure 5.1 and are highlighted in orange. First, a peak of emission on the output side is measured at the input resonance frequency of emission and biasing. This spectral line comes from the hybridization of the input and output mode due to the parasitic capacitance of the SQUID, or to say it otherwise, part of the photon emitted in the input resonator leaks to the output side as described in section 3.2.2.

Secondly, we observe a small peak below the 2 output-photon process with a bias voltage detuning of 380 MHz. This emission comes from a resonance which can be at 380 MHz or at 4.06 GHz. As we do not observe replicas of main emission peaks (first order processes), the thermal population of this mode is low. Therefore, the most probable explanation is the presence of a parasitic resonance at 4.06 GHz. Its measurement is too close to the low frequency limit of our experimental scheme to be directly measured.

5.1.1.2 Analysis using the approximated solution for *P(E)*

The approximated computation of the $P(E)$ function, presented in section 1.2, makes it possible to extract the resonator characteristics from our measurements. This approximation is easily extended to two resonators to compute the simultaneous emission in both resonators.

The integrated emitted power is peaked when the bias voltage matches the resonance frequencies of the resonators. The emitted power extracted from the power spectral density is shown in figure 5.2 with an input resonance frequency of $f_i = 6.17\,\text{GHz}$ and an output resonance frequency of $f_o = 4.44\,\text{GHz}$. With the $P(E)$ theory, we know that the ratio between the first order process and the second order process is linked to the characteristic impedance (see section 1.2.3). This indicates an input characteristic impedance of $323\,\Omega$ ($g_i = 0.40$) and an output characteristic impedance of $947\,\Omega$ ($g_o = 0.68$).

To estimate the accuracy of the characteristic impedances, we need at least to verify that our curves match the prediction from the $P(E)$ theory. To do so, we focus on cuts of the power spectral density at the resonance frequencies of both resonators. This measurement is presented in figure 5.3. In the same figure, we present the best adjustment of Lorentzian curves, as described from the $P(E)$ theory, with the experimental data.

The Lorentzian does not exactly fit the measurement for the 1-photon peaks (curve a) and b) in figure 5.3). Moreover, the bandwidth of the Lorentzian are $\gamma/(2\pi) \approx 17\,\text{MHz}$ which is 3 times higher than what was measured in section 4.2.2.6. Therefore, we can conclude that we do not verify the hypothesis of the $P(E)$ for the first photon peaks. The wider apparent bandwidths are due to a phenomenon of compression of the emission lines. The saturation of the emission rate for resonant bias voltages decreases the amplitude of the emission peak whereas the emission rate is less affected for bias voltage further away

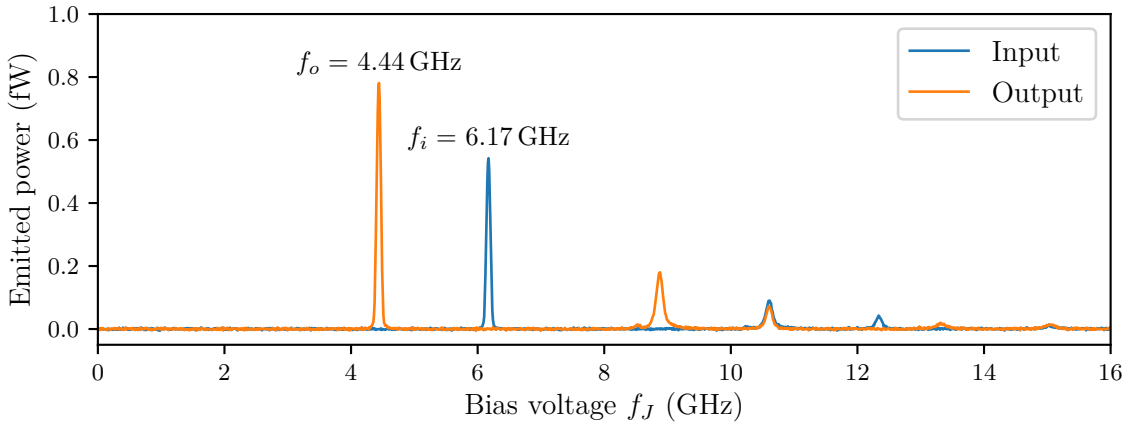

Figure 5.2: Emitted power for both sides integrated over 100 MHz around their resonance frequencies as a function of the dc-bias voltage.

from resonance. This increases the apparent bandwidths of the emission peaks.

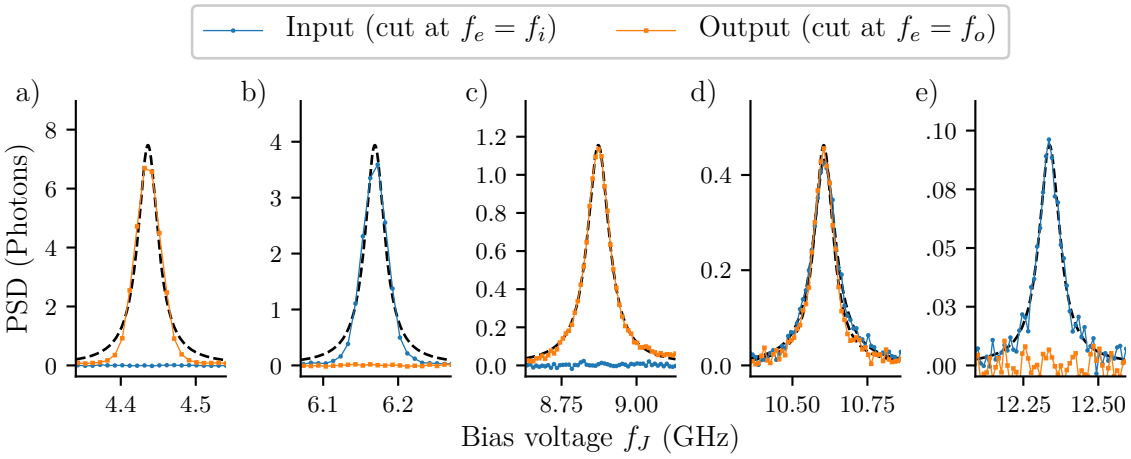

Figure 5.3: Cut of the power spectral at the resonance frequency of each resonator as function of the bias voltage. We show the emission peaks for processes where one Cooper pair gives rise to: a) 1 output photon, b) 1 input photon, c) 2 output photons, d) 1 input photon and 1 output photon, e) 2 input photons. In dashed lines, we show a fit with of the peak with a Lorentzian as predicted from the $P(E)$ theory.

However, we observe that the multi-photons peaks are well fitted with Lorentzian. From these adjustments, we can estimate the bandwidth of the resonators. Indeed, the width of a second order process is approximately the bandwidth of the resonator. We obtain an input bandwidth of approximately 35 MHz and an output bandwidth of approximately 40 MHz.

To be more precise, we fit the multi-photons emission lines with the predictions from section 1.2, with all resonator characteristics as free parameters for this adjustment. The result of this adjustment is presented in table 5.1 and the agreement between the experimental data and the fit can be observed in figure 5.4. The agreement is not perfect, but it is important to notice that the scale is logarithmic which increases the visibility of the

imperfect fit.

The measured resonance frequencies are lower than expected (see section 3.2), 560 MHz for the input resonator and 120 Hz for the output resonator. The parasitic capacitances are higher than estimated. The input resonator bandwidth is in good agreement with the prediction. The output resonator bandwidth is two times higher than expected, because the decrease in resonance frequency brings it closer to the working frequency of the $\lambda/4$ impedance transformer which increase its energy decay rate. Finally, the characteristic impedance is higher than expected.

Resonator	Frequency	HWHM $\gamma/(2\pi)$	Impedance characteristic
Input	6.17 GHz	41 MHz	292 Ω ($g_i = 0.38$)
Output	4.44 GHz	44 MHz	777 Ω ($g_o = 0.62$)

Table 5.1: Characteristics of the input and output resonators obtained by fitting the multi-photon peaks with the approximation presented in section 1.2.

However, this approach does not fully take into account the impact of the SQUID capacitance. Indeed, this capacitance has several effects on the emission lines. First, it affects the resonance frequency, bandwidth and impedance of both modes, as it acts as an additional capacitance in first approximation. As we did not make any hypothesis on the mode properties, this impact is correctly considered in this approach. Secondly, the junction capacitance couple the input and output resonator, this make it possible for the energy emitted in a resonator to leak to both sides. This effect is not take into account in this approach, and we need to describe its to verify that the capacitance junction as no dramatic effect on the resonator properties.

5.1.1.3 Power spectral density with the full impedance

In order to solve these limitations, we need to describe how the spontaneous emission leaks from the actual device. To do so, we consider the electrical schematics in figure 5.5. From it, we can define the transinductance:

$$Z_i[\omega] = \frac{V_i[\omega]}{I[\omega]} \quad \text{and} \quad Z_o[\omega] = \frac{V_o[\omega]}{I[\omega]} \tag{5.1}$$

The emission in the input port (and similarly for the output port) can be written with the current-current correlation $S_{II}(V, \omega)$ function induced by the Josephson junction:

$$\gamma_i(V, \omega) = \frac{1}{\hbar\omega} \frac{2|Z_i[\omega]|^2}{Z_0} S_{II}(V, \omega) \tag{5.2}$$

Therefore, the power spectral density can be computed in two steps. First, we compute $S_{II}(V, \omega)$ with the impedance seen from the junction and the $P(E)$ theory, then we compute the distribution of power between both sides with this equation.

To estimate the value of the electrical components of figure 5.5 by fitting the experimental data, we need to fix several parameters to obtain meaningful results. The fixed

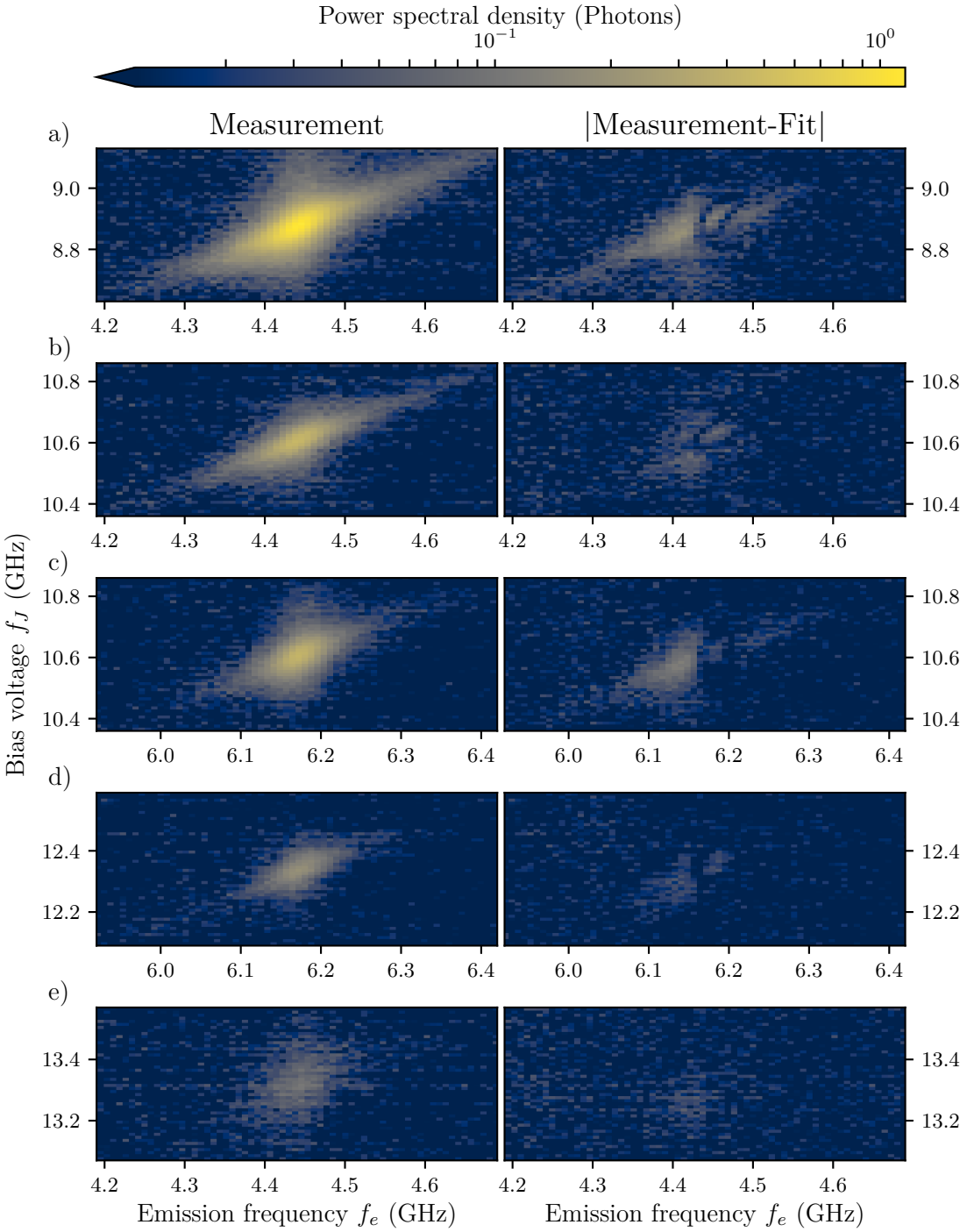

Figure 5.4: On the left, we plot the power spectral density as a function of the emission frequency and the dc-bias voltage for different processes: a) 2 output photons, b) and c) 1 input photon and 1 output photon, d) 2 input photons, e) 3 output photons. On the right, we show the difference between a fit with the emission rate deduced from the approximated $P(E)$ function (see section 1.2) and the experimental data. Notice the logarithmic scale for the power spectral density. The fit parameters are shown in table 5.1.

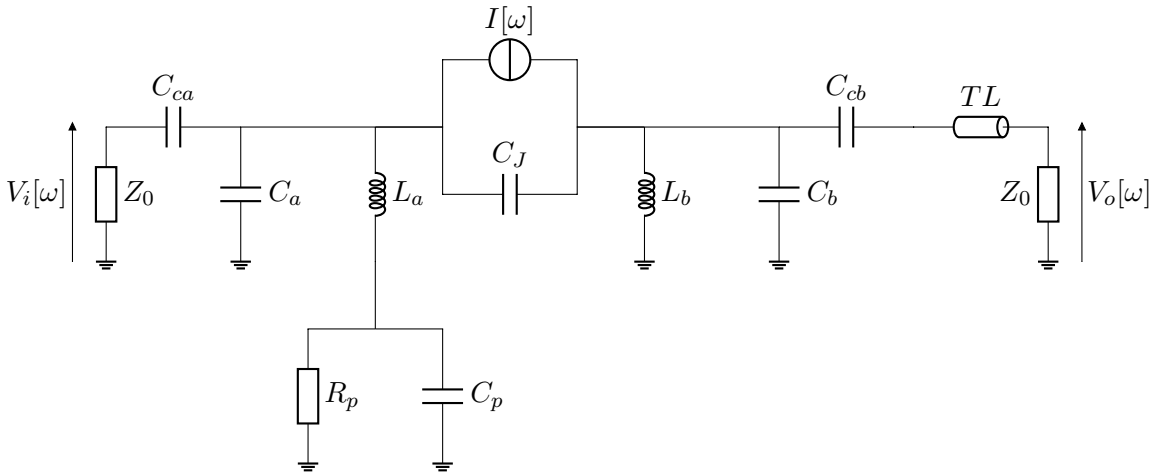

Figure 5.5: Equivalent electrical schematics of a photon-multiplication devices. The junction is modeled with a current source, this current source induces voltage on the input and output transmission lines which allows us to define the transinductance.

parameters are presented in table 5.2. The biasing components are fixed to their design values. We are confident in the simulated value of the inductance, as they were independently measured and match the results of the Sonnet simulation. The same is true for the transmission line after the correction of the Sonnet simulation. The temperature of the environment is set to match the result of the test sample. Finally, we fix the parasitic capacitance of the SQUID to our previous estimation, because the signal over noise ratio of these measurements is too low to correctly characterize it. However, we try to fit the data with different SQUID capacitance, and we observe that its quality degrades for capacitance outside of the 3.5 fF to 4.5 fF range.

With these fixed parameters, we fit the mutli-photon emission peaks using the full impedance (computed with the spice simulator) and a full computation of the $P(E)$ function. The parameters extracted are presented in table 5.2 and the result of the fit is presented in figure 5.6. We observe that the fit appears to be a bit better than the previous.

The resonator characteristics are comparable with the results obtained before. The resonance frequencies are the same, but the energy decay rates are smaller and the characteristic impedances too. These results are closer to our estimations in section 3.2.

The comparison between the two approaches is complex, as they do not rely on the same hypothesis. The first approach make fewer assumptions than the second one which relies on our knowledge of the device, we notably assume here that our fabrication process is stable enough to directly compare measurements on different wafer.

However, we see that the approximation of $P(E)$ possesses asymmetric error in figure 5.4. This error is a direct indication of the impact of the capacitance junction, as it arises from the asymmetric behavior of $Z_i[\omega]$ and $Z_o[\omega]$ due to the capacitive coupling of both resonator. You can notice that this error are much more symmetric for the components approach in figure 5.6. This asymmetry leads to an increase of the apparent bandwidth of

R_p	C_p	L_a	L_b	Z_{TL}	f_{TL}	T	C_J
5 Ω	100 pF	7.95 nH	20.8 nH	92 Ω	4.3 GHz	55 mK	4 fF

C_a	C_b	C_{ca}	C_{cb}
59.1 fF	42.7 fF	20.9 fF	15.1 fF

Resonator	Frequency	HWHM $\gamma/(2\pi)$	Impedance characteristic
Input	6.17 GHz	33 MHz	229 Ω ($g_i = 0.33$)
Output	4.44 GHz	38 MHz	648 Ω ($g_o = 0.56$)

Table 5.2: On the top, the fit parameters of the experimental data with the $P(E)$ theory. Below, we present the component values for the fit presented in figure 5.6. Finally, we present the resonator characteristics calculated from them.

both resonators which explains the difference between the two approach.

Finally, we will see in section 5.2 that the parasitic capacitance of the SQUID has a strong impact on the behavior of our device. Therefore, I consider that this second approach (with resonator properties in table 5.2) describes better the presented device. Moreover, we will use the component values for other simulations which bring complementary information to understand its operation.

5.1.2 Effect of the flux

To continue further the study of this sample, we need to explore the dependency on Josephson energy. To tune it, we can change the current which goes through the small coil near the SQUID and change the flux through it. We measure the emitted power as a function of this current for the first output emission peak in figure 5.7.

We observe a strong quasi-periodic modulation of the power with the current. For the $P(E)$ theory, the emission is proportional to E_J^2 which gives us a $\cos^2(2\pi I/I_0)$ dependency. This is not observed in our measurement which is not surprising as we already observe that the power spectral density at low Josephson energy (described in previous part and indicated by the point in green in the figure 5.7) is not correctly described by this theory for the first photon peaks.

Another peculiar effect is the non-periodicity observed in the emitted power. To understand it, we extract the frequency at which the maximum of emission occurs. In principle, this frequency is fixed as the bias voltage does not change during this measurement. However, we observe in figure 5.7 that it decreases when the current increases, which corresponds to a transinductance of 70 µΩ. The origin of this transinductance is not well understood for the moment. It is probably due to the fact that the flux and voltage bias share the same ground, therefore part of the flux bias return current can circulate trough the return line for the bias voltage.

As the effective biasing voltage change due to this, the biasing voltage gets closer to the

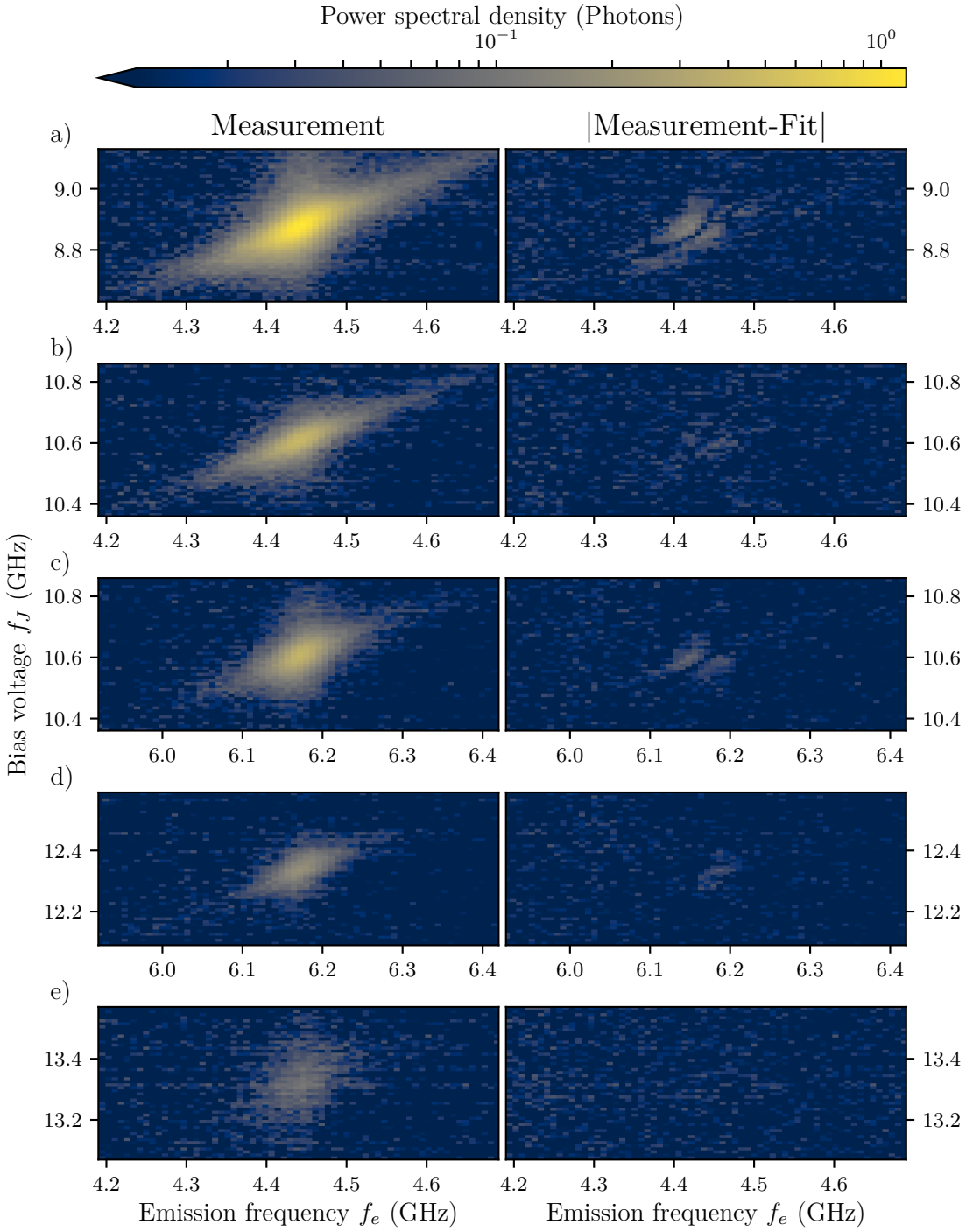

Figure 5.6: On the left, we plot the power spectral density as a function of emission frequency and dc-bias voltage for different processes: a) 2 output photons, b) and c) 1 input photon and 1 output photon, d) 2 input photons, e) 3 output photons. On the right, we represent the difference between the experimental data and the fit using the impedance described in figure 5.5, the fit parameters are shown in table 5.2.

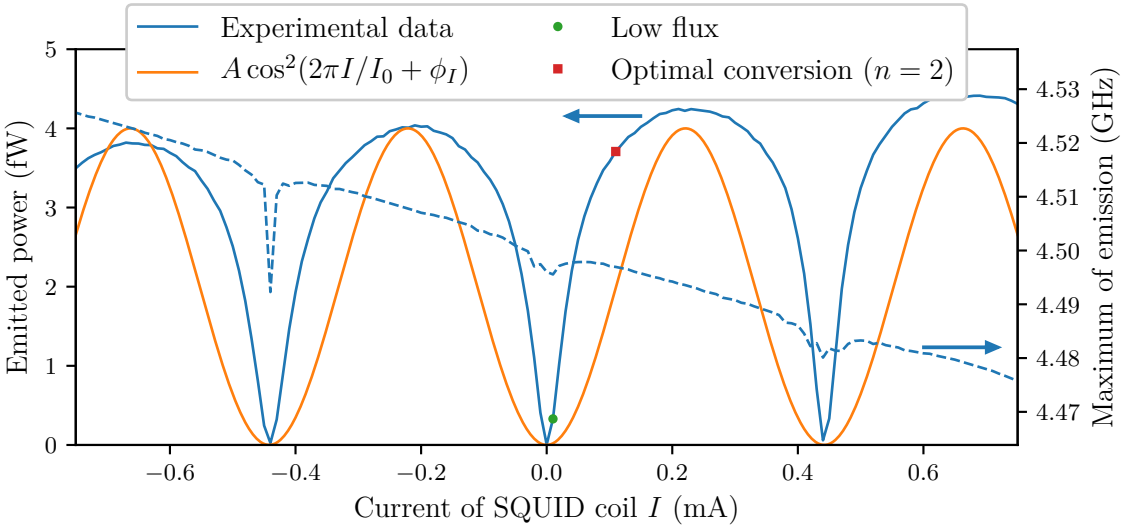

Figure 5.7: Power emitted for the one output photon emission peak as a function of the flux through the SQUID. The bias voltage is fixed at 4.5 GHz and the power is integrated over the frequency range 4.2-4.7 GHz. We plot an E_J^2 dependency with $A = 4\,\text{fW}$, $I_0 = 2.21\,\text{mA}$ and $\phi_I = \pi/2$ as a guideline for the eyes. We add the point at which we measure the PSD for the previous part (low flux) and the point at which we will study the photon multiplication (at a different bias voltage). In dashed line, we plot the frequency at which the maximum of emission is measured as a function of the current.

resonance and the emission power increase. We will now focus on what appends at higher Josephson energy, and we will focus on the point $n = 2$. The change of bias voltage at this current is 3 MHz which will not impact strongly our measurements.

5.1.3 Emission at high Josephson energy

The emission at high Josephson energy differs significantly from its properties at low Josephson energy. Lots of theoretical work [90–94] has focused on understanding the properties of the emitted field, notably its intensity and statistics. They show that the Cooper tunneling, incoherent at low Josephson energy (in the $P(E)$ theory), becomes coherent when the Josephson energy increases. This effect can lead to saturation of the emission rate and other effects such as squeezing.

As the properties of the emitted radiation are not the focus of this thesis, we will only describe the emission properties of our system and not focus on these theoretical elements.

5.1.3.1 Power spectral density and emitted power

The power spectral density is represented in figure 5.8. The main observation is the presence of a much higher number of photon emission processes with additional emission lines appearing between the main ones. Moreover, we can note that the emission lines for multi-photon processes are deformed near their resonance, they adopt a slope higher than 1 which is expected for the tunneling of one Cooper pair. Their exact shape has yet to be

exhaustively studied.

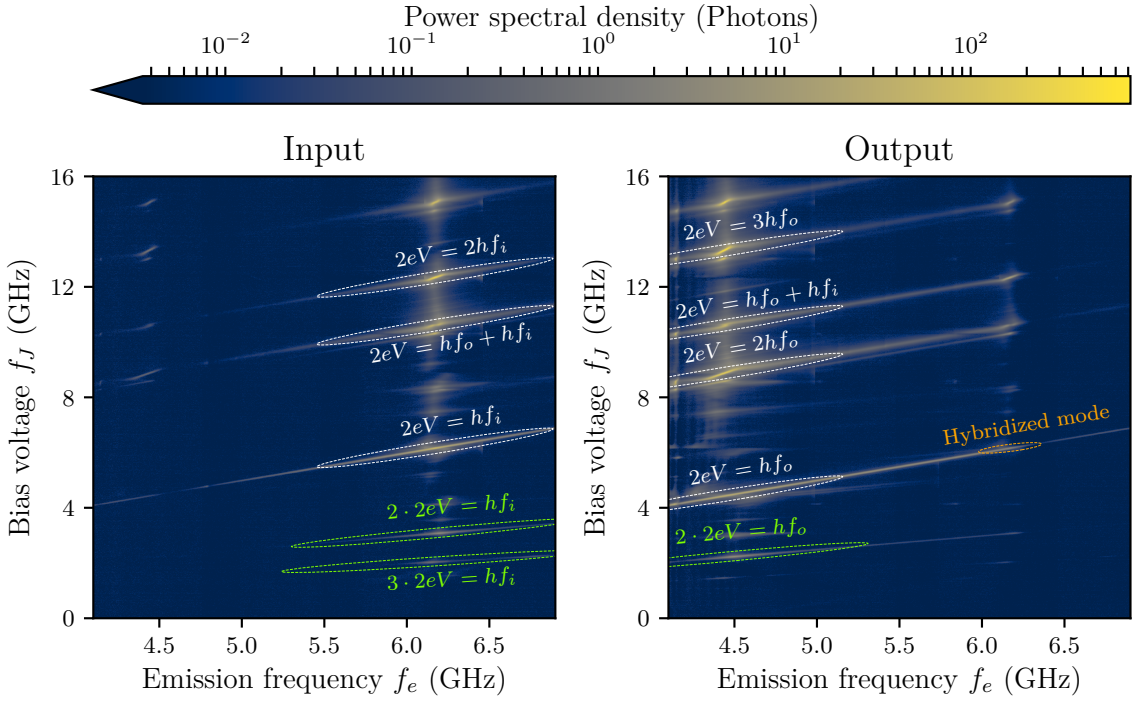

Figure 5.8: Power spectral density as a function of the frequency of emission and of the bias voltage for maximal Josephson energy. On the left we show the measurement from the input side, and on the left the measurement from the output side. The processes discussed before are indicated in white and orange. In green, we indicate other modes of emission for bias voltages lower than the fundamental emission line. They will be discussed in section 5.1.3.2.

Due to the higher emission rate, we observe more clearly the effect of the hybridization of the modes. At 4.6 GHz, we observe a cancellation of the coupling of the hybridized modes to the input lines and at 6.4 GHz to the output lines. This is in good agreement with the cancellation of $Z_i[\omega]$ (and $Z_o[\omega]$ for the output side) in equation (5.2).

To compare the amplitude of the different processes, it is easier to extract the integrated power, which is represented in figure 5.9. It is important to note that the power emitted into the input and output side is different even for the process where one photon is emitted in each resonator for the tunneling of a Cooper pair. Indeed, the energy of the two photons are different due to their different frequencies.

For the one photon emission peaks, we observe that the low impedance side (input) emits more power than the high impedance side (output). This effect comes from a faster saturation of the output side due to its higher non-linearity. Secondly, we observe that the higher order mode can emit significantly more power than the fundamental emission line. These two effects can be understood with a semi-classical approach [90]. It notably shows the apparition of fixed points due to the non-linearity when the Josephson energy increases. The behavior of these fixed points agrees with our two observations.

The parasitic peaks, as for a frequency slightly higher than 10 GHz, come from the

parasitic mode at 4.06 GHz which creates an additional mode of dissipation. Moreover, these peaks become proportionally more important as the main peaks of emission saturate at this Josephson energy.

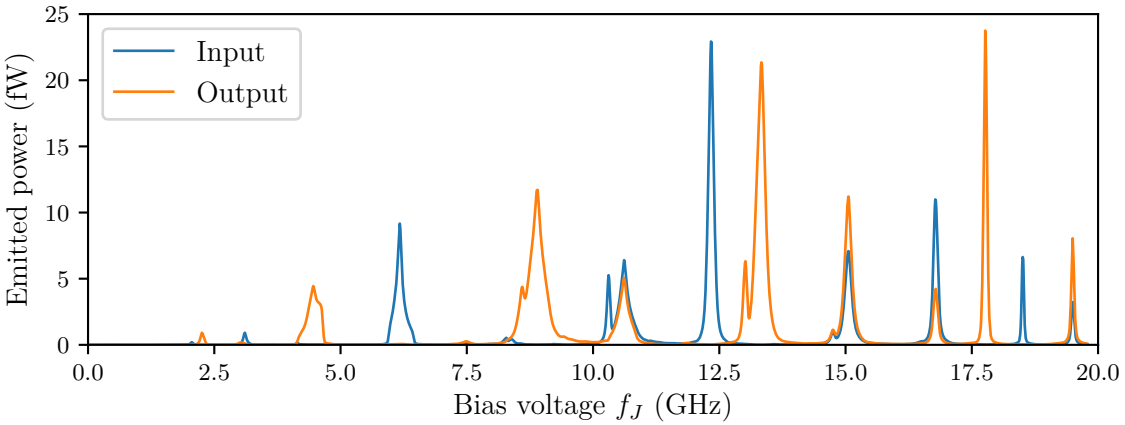

Figure 5.9: Integrated power over the full bandwidth of the input and output resonators as a function of the bias voltage. Notice that multi-photon processes emit significantly more power than the one-photon processes at maximal Josephson energy.

To conclude this part, the emission rate saturation with the increasing Josephson junction energy is beneficial for the measurement of a photo-multiplication effect. Indeed, the presence of strong emission line can lead to the apparition of instabilities due to the finite impedance of the bias circuit. The limitation of the intensity of the emission lines allows the system to stay stable.

5.1.3.2 Simultaneous tunneling of Cooper pair

We focus on the emission for bias voltage lower than the one photon emission line. These emission lines are especially interesting as they imply the simultaneous tunneling of several Cooper pairs. We show in figure 5.10, a zoom of the spectral density over these emission lines. Depending on the slope of the emission line, and the energy conservation relation, we can determine the number of Cooper pairs which tunnel for each of them.

A very recent theoretical work [95] was published on the light emitted by simultaneous tunneling of two Cooper pairs and it will be interesting to compare their predictions with our measurements on later devices. It notably shows that the emission from this process are anti-bunched for lower characteristic impedances than for the tunneling of one Cooper pair. Another recent article [96] shows that superconducting Qubits can be protected with two-Cooper-pair tunneling.

Notice that the radiation of these processes can create problems for the observation of the photon conversion of one photon to two photons, because, the bias voltage for such process is near 2.7 GHz. The photon multiplication takes place between the $2 \cdot 2eV = \hbar f_o$ and $3 \cdot 2eV = 2\hbar f_o$ processes.

During this detailed description of the spontaneous emission, we show that our description of the electromagnetic environment in section 3.2 and the extracted values from

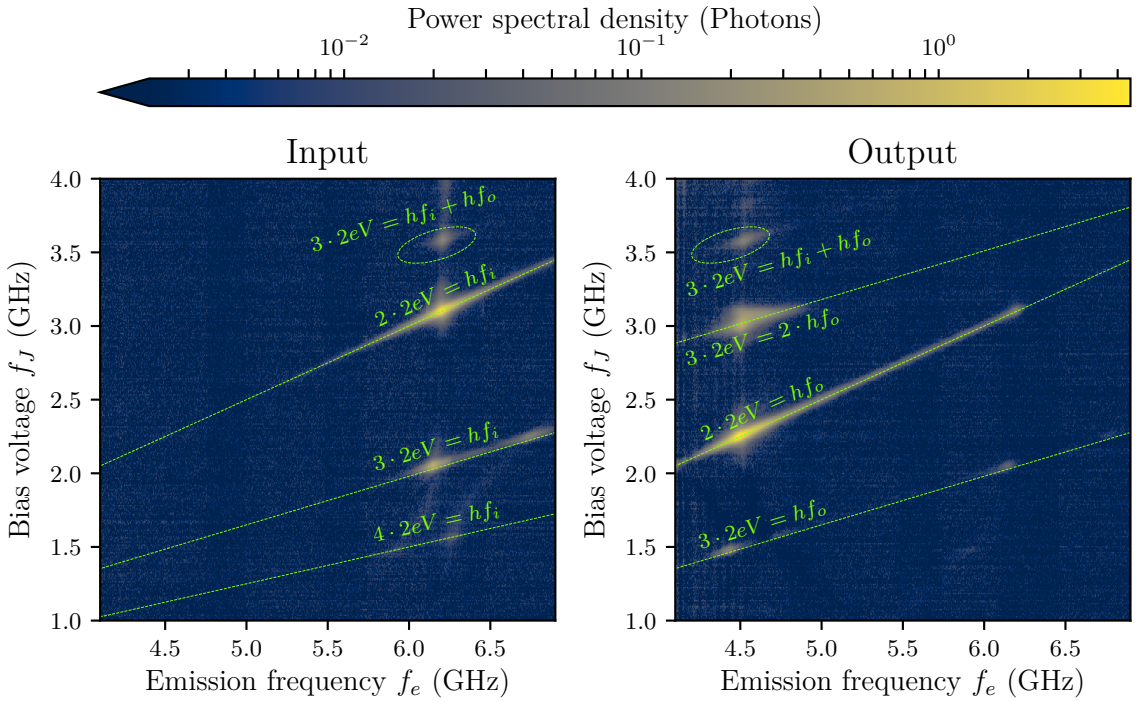

Figure 5.10: Power spectral density as a function of the emission frequency and bias voltage. We indicate several processes involving simultaneous tunneling of several Cooper pairs. The slope of the line for tunneling of n Cooper pair is 1/n, no adjustments to the data are preformed.

the low Josephson energy measurements are in a satisfactory agreement. Moreover, the measurements at a higher Josephson energy show a low spontaneous emission for several bias voltage ranges which are necessary to measure the conversion processes. Using this knowledge, we can now start confidently the discussion of the conversion measurements, first from one photon to two photons and secondly to three photons.

5.2 Conversion of one photon to two photons

The conversion of one incoming photon to several outgoing photons depends on several experimental parameters, the SQUID flux, the bias voltage and the applied microwave frequency. Moreover, the impact of each variable cannot be fully separated as they are all linked together through the equation (1.59).

We will first describe the impact of the flux on the conversion of one photon to two photons for fixed bias voltage. Then we will present the impact of the bias voltage for fixed SQUID flux. We will notably observe the main conversion process as well as other parasitic effects. Moreover, we will compare qualitatively the experimental results with theory. The effect of the power of the applied microwave field will be discussed last. Indeed, this experimental variable is less interlaced with the others.

5.2.1 Input matching with Josephson energy

As discussed in section 1.3.5, it is possible to obtain a perfect conversion for a specific Josephson energy. In order to characterize this phenomenon, we need to extract the probabilities of a photon to be reflected, transmitted or converted.

These measurements require several steps. First, we measure the PSD of the spontaneous emission of the device at the bias point (SQUID flux and bias voltage) of interest. Then, we measure the PSD at the same bias point in presence of a microwave coherent field with a given frequency and power. From these two measurements, we can extract the PSD due to the scattering of the incoming radiation. The last step is to extract the photon rate from these power spectral density measurements by integrating the PSD over specific frequency ranges. Indeed, we extract the reflected and transmitted photon rate by integrating the PSD for frequency near the applied microwave frequency whereas the converted photon rate is extracted by integrating over the output resonator frequency. From these photon rates, we can easily deduce the probability of reflection, transmission and conversion for a photon.

Notice that the bandwidth of integration for the reflected and transmitted photon rate is very similar to the IF bandwidth of a vector network analyzer, which can be used in principle to measure them. However, we cannot use it to measure the conversion photon rate.

In figure 5.11, we show the reflection, transmission and conversion probabilities as function of the microwave frequency at a fixed bias voltage and microwave power. Due to the frequency dependent attenuation of the input line, the microwave power at the input of the sample is not exactly constant but changes by 0.4 dB over the 5.9 GHz to 6.4 GHz frequency range. Notice that the bias voltage is not optimal. Indeed, for the conversion of a photon at 6.17 GHz to two photons at 4.44 GHz, the bias voltage is theoretically 2.71 GHz. We will focus on the impact of the bias voltage in section 5.2.3.

At low Josephson energy, most of the signal is reflected. When the Josephson energy increases, the photons which were initially reflected start to be converted until an optimal point is reached, the conversion efficiency decreases slightly after this point. Due to the periodic dependency of the Josephson energy with the SQUID flux, the SQUID fluxes between -0.5Φ_0 and 0 make it possible to characterize fully the dependency of the conversion process as a function of the Josephson energy.

For this measurement, the maximum conversion efficiency is 80%, the photons are reflected with a probability of 5.5% and transmitted through the sample without conversion with a probability 3.2%. This maximum of conversion is reached for an input frequency of 6.19 GHz due to the high bias voltage of 2.79 GHz.

Moreover, we observe that the probability for a photon to be transmitted through the device without conversion decreases when the probability of conversion increases with the Josephson energy. This can be explained by the fact that the conversion process depletes the photon population inside the input resonator and therefore decrease the transmission through the linear coupling between both resonators.

A last import verification is energy conservation. Within our description, a photon must be either reflected, transmitted or converted as we did not include any other dissipation. Therefore, the sum of the conversion, reflection and transmission probabilities must be

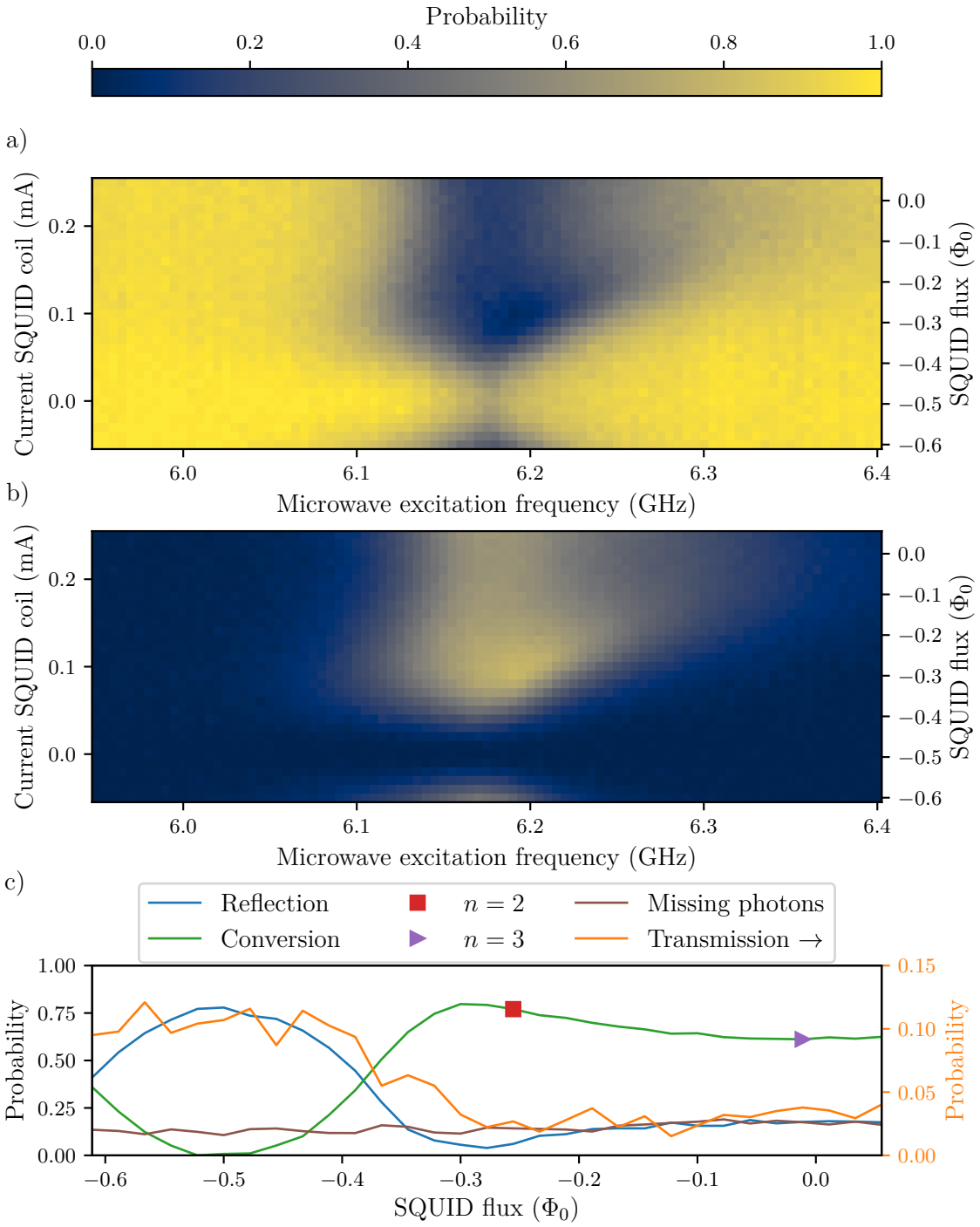

Figure 5.11: a) Probability of reflection of a coherent field as a function of its frequency and the SQUID flux. b) Probability of conversion for a multiplication factor $n = 2$ as a function of the excitation frequency and SQUID flux. c) Reflection, transmission and conversion probability for a coherent field with a frequency 6.19 GHz. The transmission scale is on the right axis to be able to observe its reduction with the SQUID flux. The points $n = 2$ and $n = 3$ indicate the flux at which we will study the $n = 2$ and $n = 3$. Finally, we added an indication of the missing photons from the energy conservation. All these curves are measured with a fixed bias voltage of 2.79 GHz and an input power of -120.9 ± 0.2 dBm.

1. In figure 5.11, we plot the difference between the sum and 1 with the label "Missing photons". For this measurement, nearly 15% of the photons vanish, we do not observe a significant impact of the conversion efficiency as for the leakage measurement.

The measurements show a maximal efficiency conversion of 80% which is in itself a very important result. However, they show that part of the power is lost and the conversion is observed for a higher bias voltage than expected.

5.2.2 Missing power

To characterize better the transmission and missing power, we plot in figure 5.12 their experimental measurements as a function of the microwave frequency when the conversion is negligible (low Josephson energy). The transmission is maximal at the resonance frequency. Moreover, the experimental measurement is nearly three times larger than the expected value from the model described in section 5.1.1.3. The origin of this disagreement is not clear, it can be an underestimation of the output resonator bandwidth or the SQUID parasitic capacitance. However, the necessary changes are not compatible with the spontaneous emission measurements.

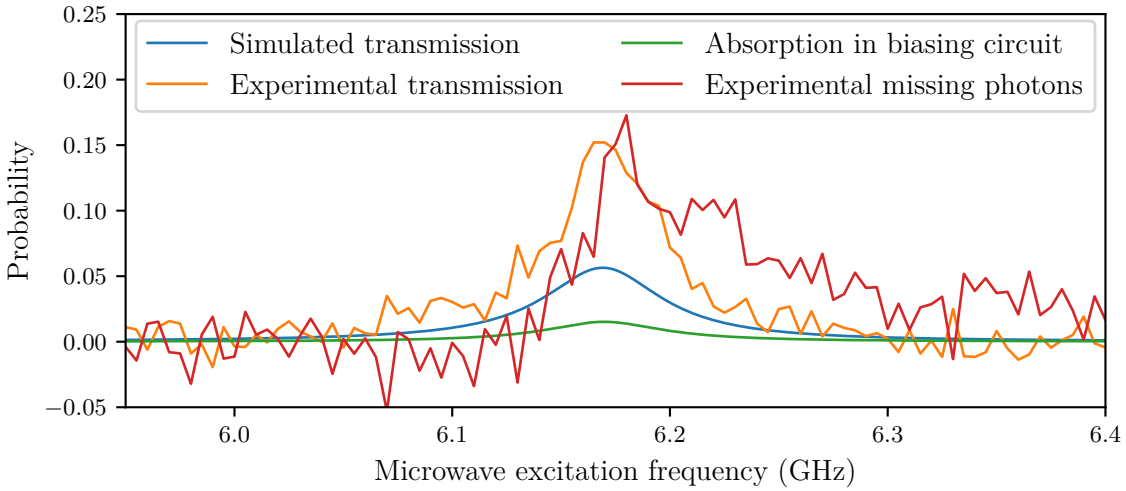

Figure 5.12: Transmission and missing energy as a function of the microwave excitation frequency. We add the result from a spice simulation with the component values determined in the previous part (table 5.2) for the transmission and absorption in the bias circuit. The experimental curves are measured for the minimal Josephson energy, i.e. the conversion process is negligible. The bias voltage is 2.79 GHz and the input power is -120.9 ± 0.2 dBm.

The behavior of the missing photons is relatively similar with a maximum of absorption at a slightly higher frequency than that resonance frequency. A simple hypothesis to explain this loss of power is to remember we cannot measure photons which are absorbed in the bias circuit. Using the spice circuit (see section 5.1.1.3), we can estimate the power which leaks to the biasing resistor. The maximum of absorption is 2% which is ten times lower that what is experimentally observed. Notice that we consider the parasitic inductance of the polarization capacitor in the simulation, otherwise, the absorption is well below 1%.

This energy loss comes probably from the microwave absorption in the circuit, mainly

dielectric loss as the loss in superconductors is negligible at these frequencies. As discussed in section 2.5, the internal quality factor is of the order of 10^4 at relatively high power which indicates that significant microwave loss is present. Moreover, in parallel plate capacitors all the electrical field is in the amorphous dielectric whereas in coplanar waveguides most of it is in the sapphire substrate. Therefore, part of the missing photons are simply absorbed by the materials used. The magnesium oxide is probably the main culprit, it rapidly adsorbs moisture which causes strong microwave absorption.

5.2.3 Photo-multiplier bandwidth and bias voltage

In order to obtain an efficient conversion, the bias voltage needs to match the energy difference between the incoming photon and the two outgoing photons. This gives a theoretical optimal bias voltage of 2.71 GHz. To characterize its effect, we show in figure 5.13, the reflection probability and conversion probability as a function of the microwave excitation frequency and bias voltage. The flux bias is fixed at -0.26Φ_0 (SQUID coil current of 0.11 mA). The bandwidth of integration is 10 MHz around the excitation frequency for the reflected and transmitted measurements, whereas the conversion power is integrated between 4.3 GHz and 4.6 GHz. In panel c), we focus on a bias voltage of 2.76 GHz where we observe the highest conversion efficiency.

We observe that the reflection probability is quite small and reaches around 1%. This is equivalent to an input return loss of -20 dB which is near the minimum we can measure (see figure 4.6). At the same time, we measure a conversion efficiency near 80% with a relatively wide bandwidth, as the half of the input photon are converted over 90 MHz.

To verify the conversation of the energy, we chose to plot it differently than before. We represent the theoretical conversion probability $C(V,\omega)$ considering the transmission $T(V,\omega)$ and reflection $R(V,\omega)$ probability:

$$C(V,\omega) = 1 - T(V,\omega) - R(V,\omega) \tag{5.3}$$

The deduced conversion efficiency is significantly higher than the experimental measurement. The difference corresponds roughly to the 15% of missing photon, we already observed. However, we will see in the next section that part of this missing energy can be accounted for by looking closely to the power spectral density of the reflected field.

It is important to note that the bias voltage used for these measurements are higher than the theoretical resonant bias voltage of 2.71 GHz. Indeed, an efficient conversion is observed for a wide bias voltage of 2.75 GHz to 2.85 GHz, the excitation frequency for the maximum conversion changing from 6.17 GHz to 6.20 GHz.

To compare more finely the theory and the experiment, we represent the conversion probability measurement and theoretical expression (equation (1.59)) in figure 5.14. The theoretical conversion probability is plotted for an optimal bias flux $\varepsilon_2 = 1$ and resonator properties deduced from the spontaneous emission measurement at low Josephson energy (see table 5.2). Notice that the bias voltage is shifted by 100 MHz for the theoretical curve, which is necessary to better observe the main features. Finally, the presence of bias voltage noise with a HWFM 5.7 MHz is taken into account. These voltage fluctuations have a narrow frequency spectrum, and we consider that they adiabatically change the conversion efficiency.

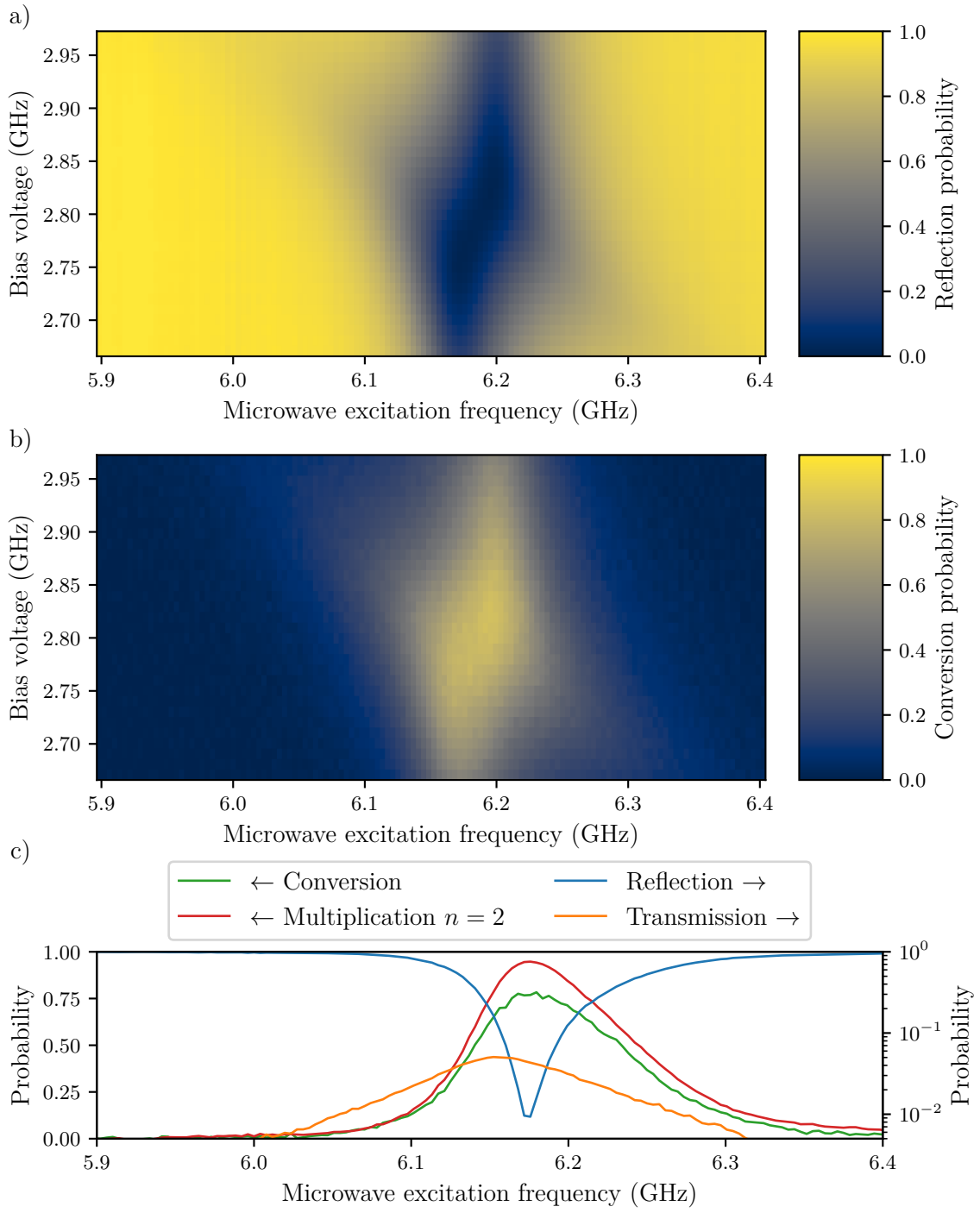

Figure 5.13: a) Probability of reflection of a coherent field as a function of its frequency and the bias voltage. b) Probability of conversion for a multiplication factor $n = 2$ as a function of the excitation frequency and bias voltage. c) On the right axis, we represent the measured reflection and transmission probability as a function of the microwave excitation frequency for a fixed biasing voltage of 2.76 GHz. On the left axis, we show the measured conversion probability and the conversion probability deduced from the transmission and reflection measurement. All curves are measured with an input power of -126.1 ± 0.2 dBm and a flux bias of -0.26Φ_0 (SQUID coil current of 0.11 mA).

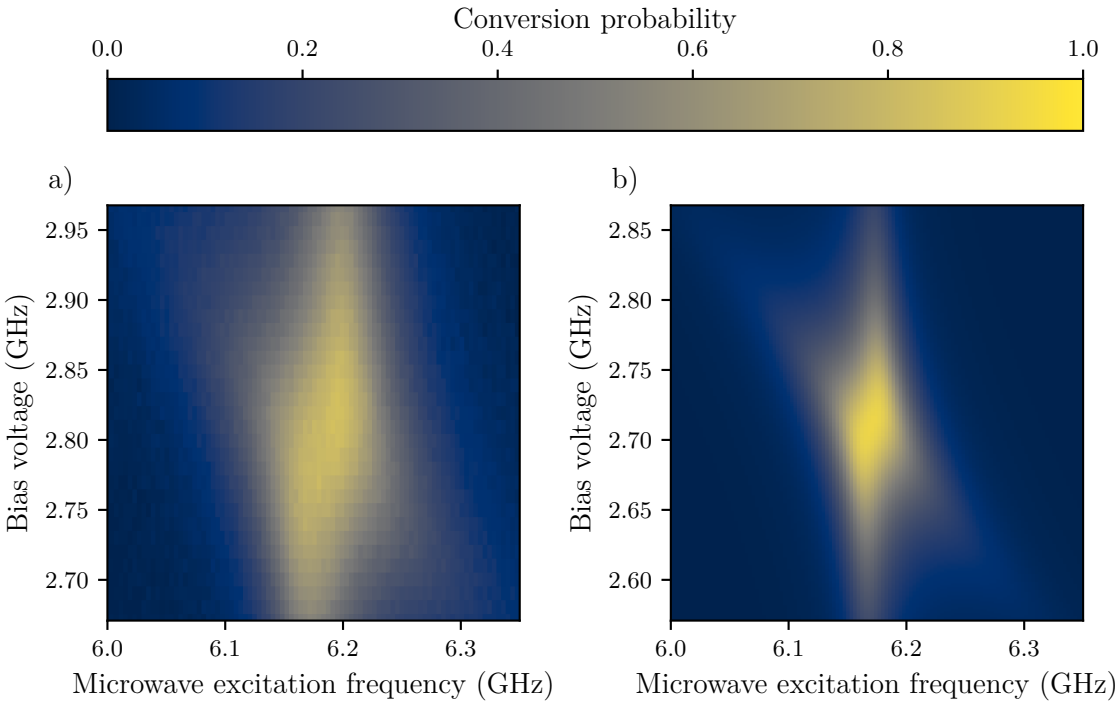

Figure 5.14: a) Experimental conversion probability as a function of the microwave excitation frequency and bias voltage. b) Theoretical conversion probability computed from equation (1.59) with the resonator parameters described in table 5.2 for an optimal flux $\varepsilon_2 = 1$ and a bias voltage noise of 5.7 MHz. Notice that the bias voltage is shifted by 100 MHz between the two plots.

Even if their general form are similar, the bias voltages are significantly different. Indeed, for unknown reasons, the frequencies of converted photons (experimentally centered at 4.48 GHz) are higher than the resonance frequency 4.44 GHz of the output resonator. For instance, the device seems to work as if the resonant frequency shifted for the conversion process. Moreover, the bandwidth of the conversion process is significantly higher than expected.

To summarize, we observe an efficient conversion over a wide range of bias voltage and a relatively wide bandwidth, even if our device possesses a limited energy decay rate for the output resonator. The differences between theory and experiments result are not completely understood. However, we focused on the extracted probabilities from the power spectral density. The precise shape of the power spectral density can also be of great interest in order to verify that the behavior of our device match our theoretical description.

5.2.4 Inelastic reflection

As we are not using a vector network analyzer, we can measure the full power spectral density of the reflected field on the input side, which allows us to track much more precisely the scattering of the input photons. In figure 5.15 a), we plot the PSD of the reflected microwave field on the input side as a function of the difference between the frequency of

measurement f_m and excitation f_e. For this first measurement, we apply no bias voltage and the SQUID flux is the same as previous measurements.

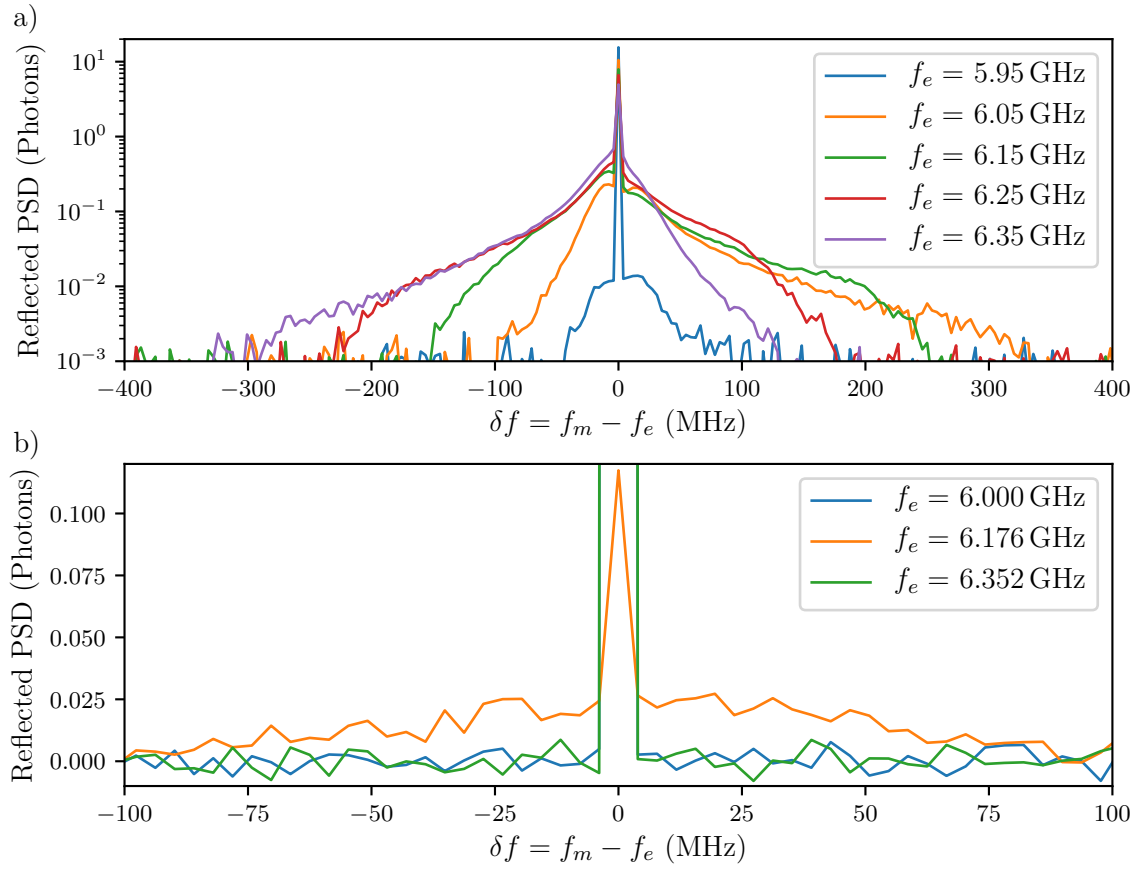

Figure 5.15: Power spectral density of the reflected microwave field as a function of the difference between the frequency f_m of measurement of the PSD and the frequency f_e of the applied microwave radiation. These measurements are performed with a SQUID flux of -0.26Φ_0 and microwave excitation power of -126.1 ± 0.2 dBm. a) The bias voltage is zero. b) The bias voltage is 2.76 GHz. Notice the different scales for the two curves. Due to the higher noise for curve b), we use a linear scale because a logarithmic scale tends to compress the structures which makes them hard to distinguish from the noise floor of this measurement.

For an excitation lower than the resonance frequency, we observe that most of the signal is elastically scattered whereas near the resonance, a significant part of the input power is scattered at a different frequency than the input frequency. Moreover, we observe that for frequency higher than the resonance frequency (outside of the bandwidth of the input resonator) a strong inelastic scattering still occurs. We attribute this effect to a change of the resonator shape due to inductive behavior of the SQUID in its superconducting state.

The polarization circuit has an impedance of 5 Ω up to 300 MHz. This low impedance brings strong current fluctuations. This is not a problem when the SQUID is polarized with a dc-bias voltage as these fluctuations are suppressed by the SQUID. However, without a bias voltage, these fluctuations directly couple to the system which make it possible

to observe additional processes. For example, a photon at the excitation frequency can be absorbed, simultaneously quanta of the current fluctuation can be either absorbed or emitted, to create a photon a different frequency. The shape in frequency of the converted photons depends on the excitation frequency and the resonator shape.

This explication is only satisfactory in the case of a SQUID in its superconducting state. The case with a bias voltage applied is slightly different. In figure 5.15 b), we show the power spectral density of the reflected field for a bias voltage of 2.76 GHz. For frequencies inside the resonator bandwidth, we observe the presence of inelastic scattering. The mixing with voltage fluctuations instead of current fluctuations is the most likely explanation.

This inelastic scattering inside the input resonator modifies the reflection probability of our device. Indeed, we only consider the photons which were elastically reflected as the reflected power was integrated over 10 MHz around the excitation frequency. In order to take into account the broadening of the excitation field, we repeat the analysis with a bandwidth of integration of 200 MHz. We plot these result in figure 5.16. We observe that it increases significantly the measured reflected probability near the resonance frequency and therefore fewer photons are unaccounted for.

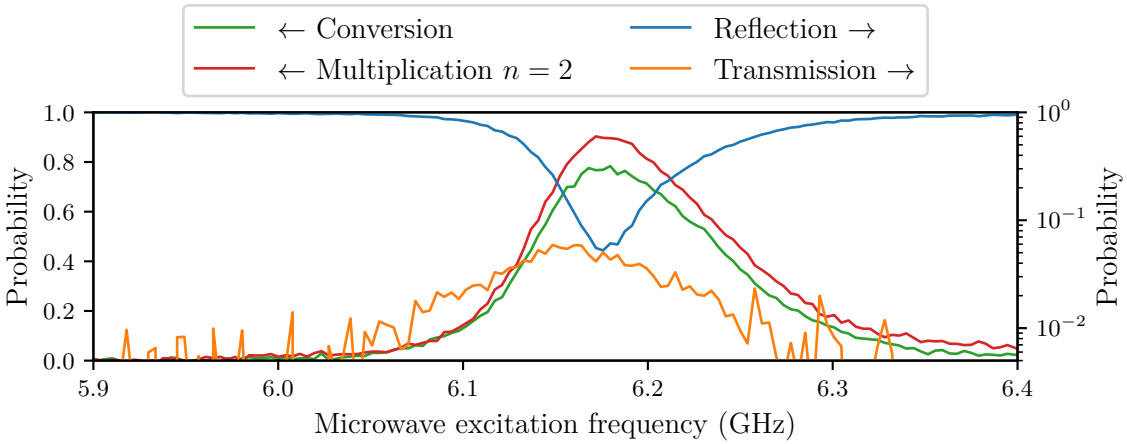

Figure 5.16: On the right axis, we represent the measured reflection and transmission probability as a function of the microwave excitation frequency for a fixed biasing voltage of 2.76 GHz. On the left axis, we show the measured conversion probability and the conversion probability deduced from the transmission and reflection measurement. These curves are measured with an input power of -126.1 ± 0.2 dBm and a flux bias of -0.26Φ_0. The bandwidth of integration was increased from 10 MHz (figure 5.14) to 200 MHz.

We show in figure 5.17 the reflected PSD for a fixed microwave excitation frequency and zero bias voltage as function of the SQUID flux. The inelastic scattering is minimal for the minimal Josephson energy, then it increases rapidly before decreasing and saturating for the highest Josephson energies. The maximum of scattering is probably linked to a matching of frequency of the resonator with excitation frequency due to the change in the SQUID inductance.

It is important to note that this inelastic scattering of the reflected signal is not taken into account in our theoretical description. Indeed, we consider that the voltage fluctuations are pushing the system out of its optimal bias point (we suppose adiabatic change of the

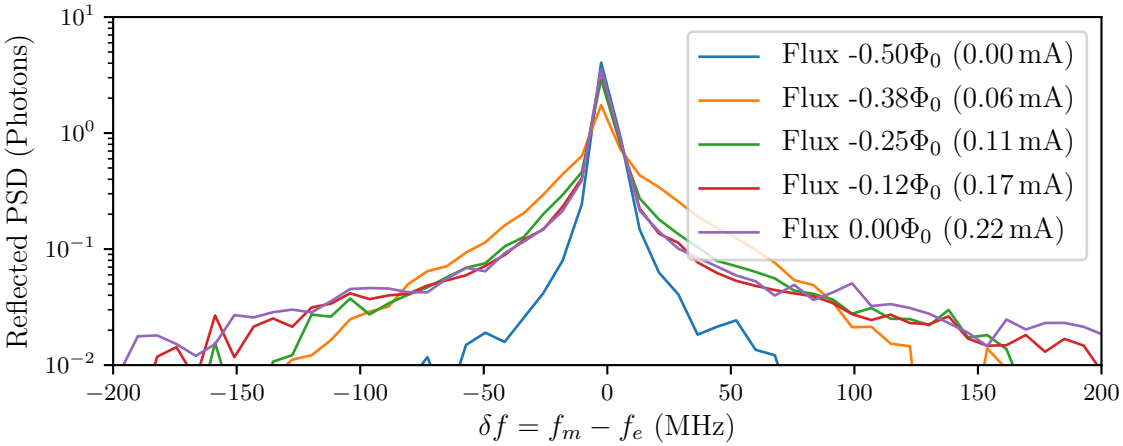

Figure 5.17: Power spectral density of the reflected microwave field as a function of the difference between the frequency f_m of measurement of the PSD and the frequency $f_e = 6.19\,\text{GHz}$ of the applied microwave radiation. The microwave excitation power is $-126.1(2)\,\text{dBm}$ and the bias voltage is zero.

bias voltage), but we do not consider the apparition of additional processes inside the input resonator.

5.2.5 Dynamical range

As a final characterization of the conversion process of our device, we measure its dynamical range. This measurement is very important to confirm that the conversion probability is not limited by the saturation of the device. We show the conversion probability as a function of the applied microwave frequency and power in figure 5.18.

For low incident power, up to 1 photon in average inside the input resonator, we observe a symmetrical shape which does not depend on the input power. This is why we place ourself in this situation for the previous measurements, except for the flux characterization with 7 photons in average in the input resonator. When this power increase, we observe that the conversion stays efficient up to 10 photons in the input resonator but the shape becomes asymmetric and the frequency of maximal conversion shifts to higher frequency. Beyond that input power, the conversion efficiency decreases rapidly with the apparition of a minimum at the resonance frequency.

This relatively high dynamical range is important as it opens the possibility to cascade such a device in order to multiply further a single microwave photon and detect it more easily. A high dynamical range is also a requirement to be able to distinguish a one-photon from a two-photon state, as the device must be able to process these two states with a high probability in order to measure them. Finally, the dynamic range can be extended further by decreasing even more the input characteristic impedance of the input mode, at least in principle (see section 1.3.6).

This concludes the characterization of the conversion of one incoming photon to two outgoing photons, as the impact of all experimental variables, bias voltage and flux, microwave frequency and power, was studied in this part.

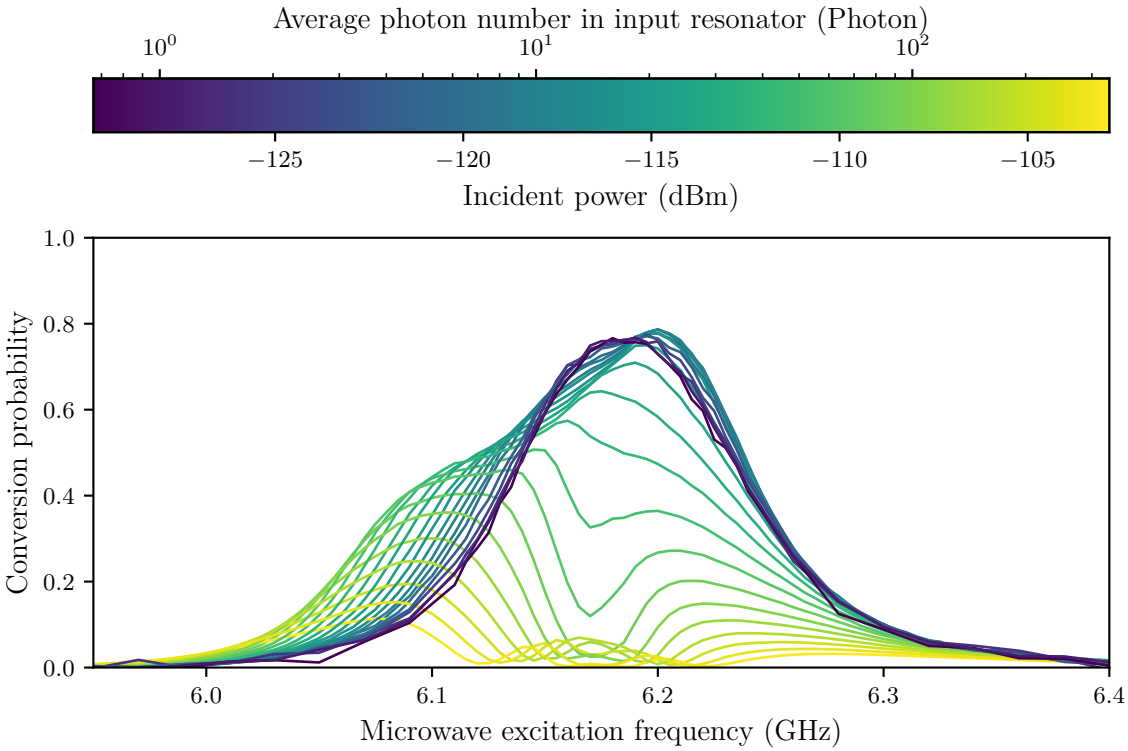

Figure 5.18: Conversion probability as a function of the microwave excitation frequency and applied microwave power. The bias voltage is 2.79 GHz and the SQUID flux is -0.26Φ_0.

5.3 Conversion of one photon to three photons

The optimal Josephson energy for the multiplication by a factor $n = 2$ is 60% of the maximum Josephson energy of the SQUID. When we have described the sample in section 3.2.4, we have shown that the conversion by a factor $n = 3$ necessitates a significantly higher Josephson energy to achieve a highly efficient conversion. Experimentally, we observe that the conversion efficiency increases up to the maximum Josephson energy achievable.

We choose here to only show in figure 5.19 the bias point at which the maximum conversion occurs. Notice that if the bias voltage was higher than expected for the tripling of a photon, the measured optimal bias voltage appends for a bias voltage 90 MHz below the expected value (7.15 GHz).

We observe a photo-multiplication by a factor 3 with an efficiency of 60% which is still interesting. The probability of transmission is quite high (10%) whereas the power loss seems to be smaller. This high transmission compared to before is probably due to the high photon population photon inside the input resonator because of the lower photon conversion. The power conservation is better respected than for previous measurements.

Conclusion

In this chapter, we have characterized our device with PSD measurements. We have found that the resonator properties are not far away from our design. We have demonstrated

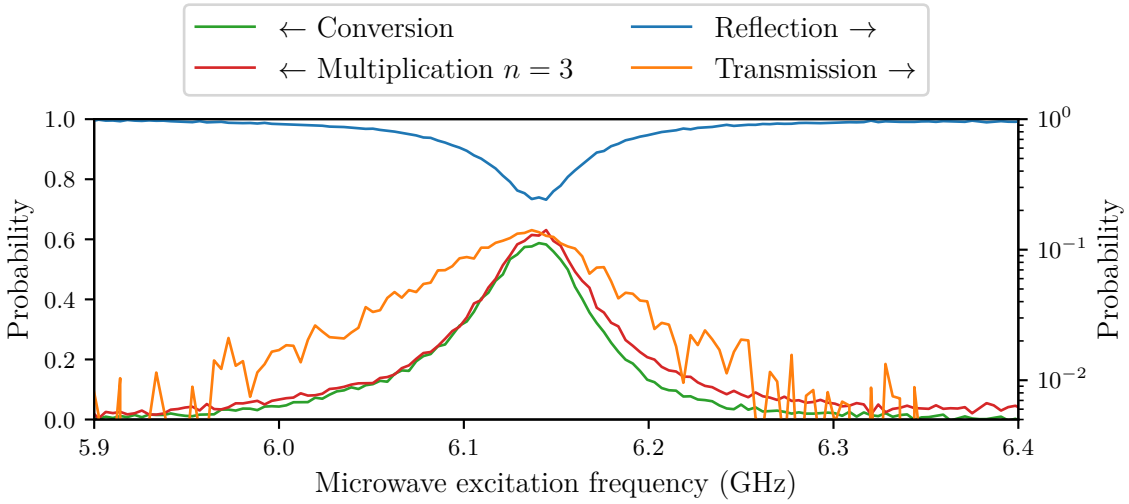

Figure 5.19: On the right axis, we represent the measured reflection and transmission probability as a function of the microwave excitation frequency. On the left axis, we show the measured conversion probability and the conversion probability deduced from the transmission and reflection measurement. These curves are measured for a fixed biasing voltage of 7.06 GHz, an input power of -126.1 ± 0.2 dBm and a flux bias of $0\Phi_0$ (current SQUID coil of 0.225 mA), which corresponds to the maximal Josephson energy. The bandwidth of integration is 200 MHz.

the conversion of one incoming photon into two photons with an efficiency of 80% and the conversion to three photons with an efficiency of 60%, limited by the maximum Josephson energy of our device. We observe that nearly 15% of the input power is not accounted for and further investigations are required to identify and mitigate this loss. Moreover, a significant inelastic scattering in the reflected power which is not considered in the theoretical approach presented.

Conclusion

This PhD work focuses on the detection of single microwave photons. We manage to perform a first step towards this goal through the demonstration of a photon multiplication by a factor $n = 2$ and $n = 3$. This device is the product of several important steps which we would like to recall here.

The first step was to understand the interaction of the charge transport through dc-biased Josephson junction with the electromagnetic environment surrounding it. This is why we have presented the $P(E)$ theory which provide a quantitative comprehension of the emission due to the strong non-linearity emerging from this interaction. Secondly, the theory developed by Juha Leppäkangas [41] highlights the important parameters in order to control the scattering of microwave radiation by such devices. A high characteristic impedance resonator for the output mode is essential for observing the photon multiplication effect, whereas the device gains at using a low input characteristic impedance resonator to improve the dynamic range.

The second and third steps are mutually dependent. Indeed, we modify our previous nano-fabrication process in order to fabricate new devices in a niobium based process. This process was developed by keeping in mind the design constraints which might have prevented the observation of wanted photon multiplication effect. For example, the understanding of the impact of the parasitic capacitance of the SQUID leads to the development of small size ($0.17\,\mu m \times 0.17\,\mu m$) Josephson junctions to mitigate its effect. Moreover, the high characteristic impedance of the output resonator required for a photon-multiplier forces us to study its fabrication and simulation early on. The fabrication was notably modified to achieve a high yield for the planar coil.

The experimental setup was modified too. The excess of voltage noise, observed since several years, was reduced to 6 MHz, i.e. divided by a factor 10 compared to previous bias circuits. Moreover, the lower impedance of this bias circuit prevents instabilities and allows us to work with higher critical current, necessary for the photo-multiplier. Finally, the software was adapted to limit the impact of the crosstalk on our measurement, notably on the direct transmission through the device.

Only the combination of all these elements makes it possible to observe a photon multiplication. We demonstrate the multiplication by a factor $n = 2$ with an efficiency of 80% and the multiplication by a factor $n = 3$ with an efficiency of 60% over a bandwidth near 100 MHz. Moreover, the spontaneous emission measurement allows us to characterize the electromagnetic environment and compare it with our design.

Naturally, several points still need to be further investigated. First, the power loss in our device forms its main drawback and we still need to study it further. Secondly, the parasitic capacitance of our device was not fully minimized which limits the characteristic impedance of our input resonator. This explains partially the limited conversion efficiency of the photon multiplication. Finally, the direct transmission was slightly higher than expected, which also decreases the conversion efficiency.

Towards single photon detection

In order to detect a single photon, we need to first increase the conversion efficiency. And secondly we must convert a single photon input to a higher number of output photons in order to detect it through subsequent linear amplification. Indeed, as this phase insensitive amplification stage adds noise (at least half a photon), a multiplication by a factor $n = 3$ is not enough to discriminate an incoming photon from vacuum. We need to achieve a higher multiplication factor to keep a good detection efficiency with a low dark count rate (see [41]).

Due to the limited characteristic impedance, it is complicated to consider a multiplication by a factor n higher than 3, because the Josephson energy and parasitic processes become too important. However, the high dynamical range of our device, see section 5.2.5, makes it possible to cascade two conversion stages to achieve higher multiplication factors. This can be done in principle by just connecting two presented devices, but it is more clever to integrate these two stages into a single device. Indeed, one of the resonators can be shared between the two multiplication stages, therefore we do not need to couple to a low impedance environment between the two stages.

We present in figure 1, a schematic of a cascaded photon multiplier. By tuning the bias voltages V_1 and V_2, it is possible to achieve a photo-multiplication by various factors. We present the conversion of one incoming photon into nine outgoing photons, as it is a process easily achievable and it can be used to fabricate a single photon detector with a total efficiency of 0.9 with a low dark count ($10^{-3} \times \gamma_o$). Notice that this device can achieve theoretically a perfect photon-multiplication by tuning the Josephson energy of only one of the two stages, therefore its matching is not more complicated than for a single stage device.

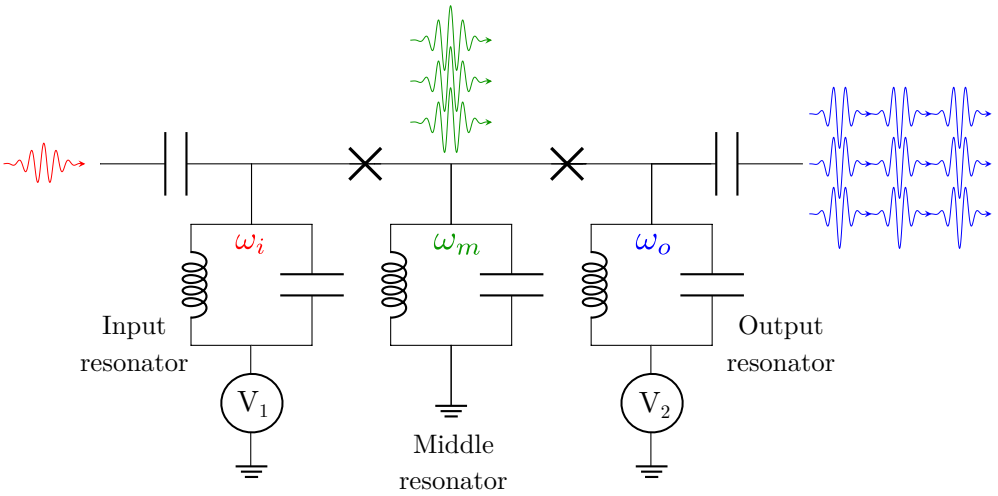

Figure 1: Schematic of a cascaded photo-multiplier device. We represent here a photon multiplication by a factor 3 for the first and second stage. Therefore a single incoming photon is converted to 9 outgoing photons.

This device, presented in figure 1, addresses one identified drawback of our current device, indeed it limits the direct transmission through the device. The frequency detuning

between the middle resonator and the input or output resonator decrease the direct coupling between them. The other drawbacks could be mitigated by modification of the fabrication process.

After the move of Max Hofheinz to Sherbrooke in January 2018, a new fabrication process was developed there by Youcef Ataellah Bioud and me. This process is very similar to the one used in this PhD thesis, as it is constituted by a base wiring and a counter-electrode in niobium with a silicon nitride dielectric between the two. However, we decided to give up the niobium junction in favor of a standard shadow evaporation of aluminum, in order to increase their fabrication yield. Therefore, we do not need the spacer which was a critical step of the previous process. Moreover, the etching of the niobium is now performed in a chlorine plasma which attacks selectively the niobium compared to the silicon nitride. The magnesium oxide is therefore not needed anymore. This will decrease the microwave loss which is the second main drawback of our device.

With our improved comprehension of the parasitic capacitance effect and the possibilities of the new fabrication process, we have designed a new mask set to increase the characteristic impedance of the resonators and add a cascaded photo-multiplier device, presented in figure 2. Its fabrication is currently ongoing and its characterization will be the direct continuation of this work.

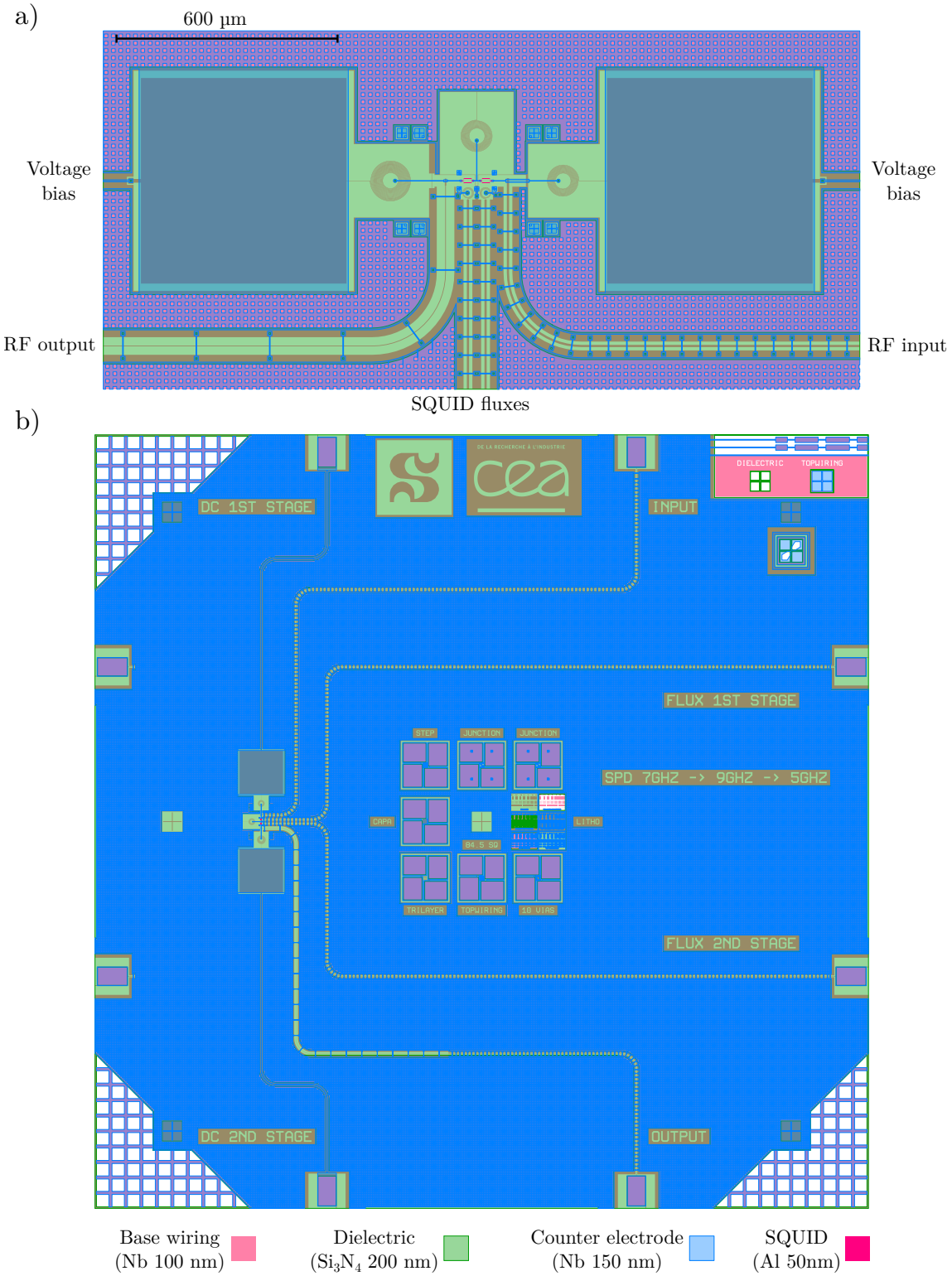

Figure 2: Layout of a dual stage photo-multiplier. a) Zoom on the active area of the device. We recognize three resonators, the input resonator is centered at 7 GHz, the middle resonator at 9 GHz and the output resonator at 5 GHz. b) Full view of a chip, the size of a die is 10 mm × 10 mm.

Appendices

Appendix A

Theory

A.1 Transformation between the charge node/branch for a chain

We will compute the Hamiltonian of the circuit in figure A.1 with the node method. For details on the computation of the matrices C and L^{-1}, see [36].

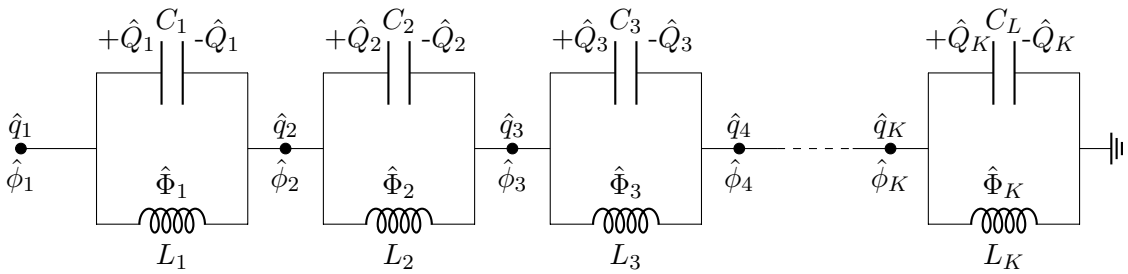

Figure A.1: Calderira-Leggett model of an impedance. These resonators can be described by two sets of variables, the charge $\hat{q}_k$ and flux $\hat{\phi}_k$ at the node k or the flux $\hat{\Phi}_k$ through the inductor k and the charge $\hat{Q}_k$ of the capacitor k.

We first compute the C matrix:

$$C = \begin{pmatrix} C_1 & -C1 & & & & & \\ -C_1 & C_1+C_2 & -C_2 & & & & \\ & -C_2 & C_2+C_3 & -C_3 & & & \\ & & \ddots & \ddots & \ddots & & \\ & & & -C_{K-2} & C_{K-2}+C_{K-1} & -C_{K-1} & \\ & & & & -C_{K-1} & C_{K-1}+C_K \end{pmatrix} \tag{A.1}$$

which can be inverted [97]:

$$C^{-1} = \begin{pmatrix} \sum_{k=1}^{K} C_k^{-1} & \sum_{k=2}^{K} C_k^{-1} & \sum_{k=3}^{K} C_k^{-1} & \dots & C_K^{-1} \\ \sum_{k=2}^{K} C_k^{-1} & \sum_{k=2}^{K} C_k^{-1} & \sum_{k=3}^{K} C_k^{-1} & \dots & C_K^{-1} \\ \sum_{k=3}^{K} C_k^{-1} & \sum_{k=3}^{K} C_k^{-1} & \sum_{k=3}^{K} C_k^{-1} & \dots & C_K^{-1} \\ \vdots & \vdots & \vdots & \ddots & \vdots \\ C_K^{-1} & C_K^{-1} & C_K^{-1} & \dots & C_K^{-1} \end{pmatrix} \tag{A.2}$$

The L^{-1} matrix can be written:

$$L^{-1} = \begin{pmatrix} L_1^{-1} & -L^{-1}1 & & & & \\ -L_1^{-1} & L_1^{-1}+L_2^{-1} & -L_2^{-1} & & & \\ & -L_2^{-1} & L_2^{-1}+L_3^{-1} & -L_3^{-1} & & \\ & & \ddots & \ddots & \ddots & \\ & & & -L_{K-2}^{-1} & L_{K-2}^{-1}+L_{K-1}^{-1} & -L_{K-1}^{-1} \\ & & & & -L_{K-1}^{-1} & L_{K-1}^{-1}+L_K^{-1} \end{pmatrix} \tag{A.3}$$

We can finally express the Hamiltonian:

$$\hat{H} = \frac{1}{2}\vec{\hat{q}}^t C^{-1}\vec{\hat{q}} + \frac{1}{2}\vec{\hat{\phi}}^t L^{-1}\vec{\hat{\phi}} \tag{A.4}$$

$$\hat{H} = \sum_{k=1}^{K}\frac{1}{2C_k}\left(\sum_{n=1}^{k}\hat{q}_n\right)^2 + \sum_{k=1}^{K}\frac{1}{2L_k}\left(\hat{\phi}_k - \hat{\phi}_{k+1}\right)^2 + \frac{\hat{\phi}_K^2}{2L_K} \tag{A.5}$$

where the conjugated variables are not evident.

We can define the change of variables:

$$\hat{Q}_k = \sum_{n=1}^{k}\hat{q}_n \quad \text{and} \quad \hat{\Phi}_k = \begin{cases} \hat{\phi}_k - \hat{\phi}_{k+1} & \text{if } k < K \\ \hat{\phi}_K & \text{if } k = K \end{cases} \tag{A.6}$$

This new variables are $\hat{Q}_k$, the charge of the capacitor C_k, and $\hat{\Phi}_k$, the flux through the inductor L_k, therefore the natural variables are the flux and charge of the branches and not of the nodes. We can verify that this change of variables conserves the commutator relation:

$$\left[\hat{q}_k, \hat{\phi}_n\right] = \left[\hat{Q}_k, \hat{\Phi}_n\right] = i\hbar\delta_{kn} \tag{A.7}$$

We obtain the Hamiltonian:

$$\hat{H} = \sum_{k=1}^{K}\left(\frac{\hat{Q}_k^2}{2C_k} + \frac{\hat{\Phi}_k^2}{2L_k}\right) \tag{A.8}$$

which is an ensemble of independent harmonic oscillators. We can then treat it as usual by introducing the creation and annihilation operator:

$$\hat{\Phi}_k = \Phi_k\left(\hat{a}_k + \hat{a}_k^\dagger\right) \quad \text{and} \quad \hat{Q}_k = Q_k\frac{\left(\hat{a}_k - \hat{a}_k^\dagger\right)}{\mathrm{i}} \tag{A.9}$$

with:

$$\Phi_k = \sqrt{\frac{\hbar Z_k}{2}} \quad \text{and} \quad Q_k = \sqrt{\frac{\hbar}{2Z_k}} \quad \text{where} \quad Z_k = \sqrt{\frac{L_k}{C_k}} \tag{A.10}$$

The Hamiltonian can finally be written:

$$\hat{H} = \sum_{k=1}^{K}\hbar\omega_k\left(\hat{a}_k^\dagger\hat{a}_k + \frac{1}{2}\right) \tag{A.11}$$

where $\omega_k = \left(\sqrt{L_k C_k}\right)^{-1}$. Notice that we have a diverging term when we take K to infinity, as usual in quantum field theory.

A.2 Details on the computation of P(E)

We will give here details on the $P(E)$ theory in second quantification, see section 1.1.2. The starting point is equation (1.16):

$$\vec{\Gamma} = \frac{\pi E_J^2}{2\hbar} \sum_{n_1,n_2\cdots} \sum_{m_1\cdots} \prod_{k=1}^{K} \left| \langle m_k | \, e^{\mathrm{i}g_k\left(\hat{a}_k + \hat{a}_k^\dagger\right)} \, |n_k\rangle \right|^2 P_{k,\beta}(|n_k\rangle) \frac{1}{\hbar} \delta\left(\sum_{k=1}^{K} [m_k - n_k]\omega_k + \omega_J \right) \tag{A.12}$$

We write the delta function as its inverse Fourier transform:

$$\Gamma = \frac{E_J^2}{4\hbar^2} \int_{-\infty}^{\infty} \mathrm{d}t \sum_{n_k} \sum_{m_k} \prod_{k=1}^{K} \left| \langle m_k | \, e^{\mathrm{i}g_k\left(\hat{a}_k + \hat{a}_k^\dagger\right)} \, |n_k\rangle \right|^2 e^{\mathrm{i}(m_k - n_k)\omega_k t} P_{k,\beta}(|n_k\rangle) e^{\mathrm{i}\omega_J t} \tag{A.13}$$

By changing the order of operator and using a classical identity for bosonic fields[1], we can absorb the exponential dependency in energy by expressing the operator in the Heisenberg picture:

$$\begin{aligned} &\left| \langle m_k | \, e^{\mathrm{i}g_k\left(\hat{a}_k + \hat{a}_k^\dagger\right)} \, |n_k\rangle \right|^2 e^{\mathrm{i}(m_k - n_k)\omega_k t} \\ &\quad = \langle n_k | \, e^{-\mathrm{i}\omega_k t \hat{a}_k^\dagger \hat{a}_k} e^{\mathrm{i}g_k\left(\hat{a}_k + \hat{a}_k^\dagger\right)} e^{\mathrm{i}\omega_k t \hat{a}_k^\dagger \hat{a}_k} \, |m_k\rangle \, \langle m_k | \, e^{-\mathrm{i}g_k\left(\hat{a}_k + \hat{a}_k^\dagger\right)} \, |n_k\rangle \\ &\quad = \langle n_k | \exp\Big[\mathrm{i}g_k \Big(\underbrace{\hat{a}_k e^{-\mathrm{i}\omega_k t}}_{\hat{a}_k(t)} + \hat{a}_k^\dagger e^{\mathrm{i}\omega_k t} \Big) \Big] \, |m_k\rangle \, \langle m_k | \, e^{-\mathrm{i}g_k\left(\hat{a}_k + \hat{a}_k^\dagger\right)} \, |n_k\rangle \end{aligned} \tag{A.14}$$

We can then write the tunneling rate by taking advantage of the completeness relation:

$$\vec{\Gamma} = \frac{\pi E_J^2}{2\hbar^2} \int_{-\infty}^{\infty} \mathrm{d}t \prod_{k=1}^{K} \sum_{n_k} \langle n_k | \, e^{\mathrm{i}g_k\left(\hat{a}_k(t) + \hat{a}_k^\dagger(t)\right)} e^{-\mathrm{i}g_k\left(\hat{a}_k(0) + \hat{a}_k^\dagger(0)\right)} \, |n_J\rangle \, P_{k,\beta}(|n_k\rangle) e^{i\omega_J t} \tag{A.15}$$

The next step is to make the hypothesis that each resonator is in thermal equilibrium, and rewrite the sum as an equilibrium correlation function. We then use the generalized Wick theorem for equilibrium functions, see [16]:

$$\begin{aligned} &\sum_{n_k} \langle n_k | e^{\mathrm{i}g_k\left(\hat{a}_k(t) + \hat{a}_k^\dagger(t)\right)} e^{-\mathrm{i}g_k\left(\hat{a}_k(0) + \hat{a}_k^\dagger(0)\right)} \, |n_J\rangle \, P_{k,\beta}(|n_k\rangle) \\ &\qquad = \left\langle e^{\mathrm{i}g_k\left(\hat{a}_k(t) + \hat{a}_k^\dagger(t)\right)} e^{-\mathrm{i}g_k\left(\hat{a}_k(0) + \hat{a}_k^\dagger(0)\right)} \right\rangle \\ &\qquad = \exp\Big[g_k^2 \Big\langle \Big(\hat{a}_k(t) + \hat{a}_k^\dagger(t) - \hat{a}_k(0) - \hat{a}_k^\dagger(0) \Big) \Big(\hat{a}_k(0) + \hat{a}_k^\dagger(0) \Big) \Big\rangle \Big] \end{aligned} \tag{A.16}$$

The tunneling rate can then be expressed as:

$$\vec{\Gamma} = \frac{\pi E_J^2}{2\hbar^2} \int_{-\infty}^{\infty} \mathrm{d}t \exp\Bigg[\underbrace{\sum_{k=1}^{K} g_k^2 \Big\langle \Big(\hat{a}_k(t) + \hat{a}_k^\dagger(t) - \hat{a}_k(0) - \hat{a}_k^\dagger(0) \Big) \Big(\hat{a}_k(0) + \hat{a}_k^\dagger(0) \Big) \Big\rangle}_{J(t)} \Bigg] e^{i\omega_J t} \tag{A.17}$$

[1] $e^{-\alpha \hat{a}^\dagger \hat{a}} \; f\left(\hat{a}^\dagger, \hat{a}\right) e^{\alpha \hat{a}^\dagger \hat{a}} = f\left(\hat{a}^\dagger e^{-\alpha}, \hat{a} \; e^{\alpha}\right)$

We can compute each term of the phase-phase correlation function as:

$$\begin{aligned}\Big\langle\Big(\hat{a}_k(t)+\hat{a}_k^\dagger(t)-\hat{a}_k(0)-\hat{a}_k^\dagger(0)\Big)\Big(\hat{a}_k(0)+\hat{a}_k^\dagger(0)\Big)\Big\rangle &= \\ &= \Big\langle\Big(\hat{a}_k e^{-\mathrm{i}\omega_k t}+\hat{a}_k^\dagger e^{\mathrm{i}\omega_k t}-\hat{a}_k-\hat{a}_k^\dagger\Big)+\Big(\hat{a}_k\hat{a}_k^\dagger\Big)\Big\rangle \\ &= \Big\langle\hat{a}_k^\dagger\hat{a}_k\Big\rangle\Big(e^{\mathrm{i}\omega_k t}-1\Big)+\Big\langle\hat{a}_k\hat{a}_k^\dagger\Big\rangle\Big(e^{-\mathrm{i}\omega_k t}-1\Big) \\ &= \coth\!\left(\frac{\beta\hbar\omega_k}{2}\right)[\cos(\omega_k t)-1]-\mathrm{i}\sin(\omega_k t)\end{aligned} \tag{A.18}$$

Finally, we can express the full phase-phase correlation function as a function of the impedance and transform the sum into an integral with appropriate limits:

$$\begin{aligned}J(t) &= \sum_{k=1}^{K}\frac{\pi Z_k}{R_Q}\left\{\coth\!\left(\frac{\beta\hbar\omega_k}{2}\right)[\cos(\omega_k t)-1]-\mathrm{i}\sin(\omega_k t)\right\} \\ &= 2\sum_{k=1}^{K}\Delta\omega\frac{\mathrm{Re}(Z(\omega_k))}{\omega_k R_Q}\left\{\coth\!\left(\frac{\beta\hbar\omega_k}{2}\right)[\cos(\omega_k t)-1]-\mathrm{i}\sin(\omega_k t)\right\} \\ &\underset{\substack{K\to\infty\\ \Delta\omega\to 0}}{=} 2\int_0^\infty\frac{\mathrm{d}\omega}{\omega}\frac{\mathrm{Re}Z(\omega)}{R_Q}\left\{\coth\!\left(\frac{\beta\hbar\omega}{2}\right)[\cos(\omega t)-1]-\mathrm{i}\sin(\omega t)\right\}\end{aligned} \tag{A.19}$$

A.3 High-frequency impedance

The impedance seen by the junction in the circuit in figure A.2 can be written:

$$\begin{aligned}Z[\omega] &= \left(\mathrm{j}C_{res}\omega+\frac{1}{\mathrm{j}\omega L_{res}}+\frac{1}{Z_0+\frac{1}{\mathrm{j}\omega C_c}}\right)^{-1} \\ &= \frac{\mathrm{j}L_{res}\omega\left(1+\mathrm{j}\frac{\omega}{\omega_Z}\right)}{1-\frac{\omega^2}{\omega_r^2}+\mathrm{j}\frac{\omega}{\omega_Z}\left(1-\frac{\omega^2}{\omega_{LC}^2}\right)}\end{aligned} \tag{A.20}$$

where $\omega_Z=(Z_0C_c)^{-1}$, $\omega_r=(L_{res}(C_{res}+C_c))^{-1/2}$ and $\omega_{LC}=(L_{res}C_{res})^{-1/2}$.

We can then compute its real part:

$$\mathrm{Re}(Z[\omega])=\frac{\frac{L_{res}\omega^2}{\omega_Z}\left(\frac{\omega^2}{\omega_r^2}-\frac{\omega^2}{\omega_{LC}^2}\right)}{\left[1-\frac{\omega^2}{\omega_r^2}\right]^2+\left[\frac{\omega}{\omega_Z}\left(1-\frac{\omega^2}{\omega_{LC}^2}\right)\right]^2} \tag{A.21}$$

For $\omega=\omega_r$, $\left[1-\frac{\omega^2}{\omega_r^2}\right]^2+\left[\frac{\omega}{\omega_Z}\left(1-\frac{\omega^2}{\omega_{LC}^2}\right)\right]^2\ll 1$ as $\omega_Z\gg\omega_r$. The maximum of the real part of impedance will be near ω_r. Therefore, we write its Taylor expansion to obtain:

$$\mathrm{Re}(Z[\omega\approx\omega_r])\approx\frac{\frac{L_{res}\omega_r}{2}\omega_r\frac{\omega_r^2}{2\omega_Z}\left(1-\frac{\omega_r^2}{\omega_{LC}^2}\right)}{(\omega-\omega_r)^2+\left[\frac{\omega_r^2}{2\omega_Z}\left(1-\frac{\omega_r^2}{\omega_{LC}^2}\right)\right]^2} \tag{A.22}$$

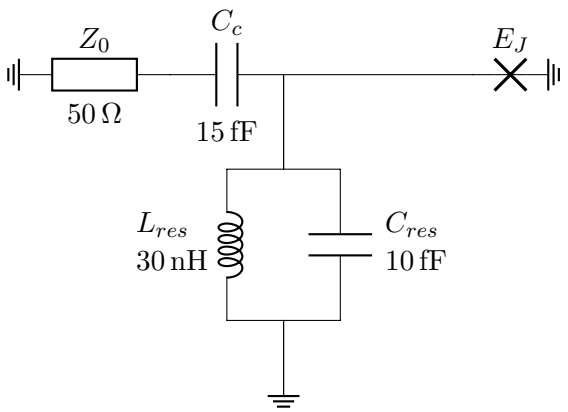

Figure A.2: Equivalent electrical schematic at high frequency of the figure 1.3. The parasitic capacitance of the Josephson junction can be absorbed in C_{res}.

Finally, we write its normalized value as a Lorentzian:

$$\frac{2\mathrm{Re}(Z[\omega \approx \omega_r])}{R_Q} = r\frac{1}{\pi}\frac{\gamma\omega_0}{(\omega-\omega_0)^2+\gamma^2} \tag{A.23}$$

where:

$$\omega_0 = \omega_r = \frac{1}{\sqrt{L_{res}(C_{res}+C_c)}} \tag{A.24}$$

$$\gamma = \frac{\omega_r^2}{2\omega_Z}\left(1-\frac{\omega_r^2}{\omega_{LC}^2}\right) = \frac{Z_0}{2L_{res}}\left(\frac{C_c}{C_{res}+C_c}\right)^2 \tag{A.25}$$

$$r = \frac{\pi L_{res}\omega_r}{R_Q} = \frac{\pi Z}{R_Q} \quad \text{with} \quad Z = \sqrt{\frac{L_{res}}{C_{res}+C_c}} \tag{A.26}$$

Notice that the condition $\omega_Z \gg \omega_r$ is verified if $\gamma \ll \omega_0$. In other words, this condition is verified if a strong resonance is present.

A.4 Computation of the Minnhagen equation

As described in section 1.1.4, it is clear that for a peaked environment at given angular frequency ω_0, the probability function $P(E)$ is peaked when the energy of the Cooper pair match the energy of emission. So to get a good understanding of the physics, we don't need to compute $P(E)$ fully but only for $E \approx n\hbar\omega_0$ where n is an integer. We will give an approximated derivation of the Minnhagen equation, similar to [1].

As explain in section 1.2.1, we consider the impedance:

$$r[\omega] = \frac{2\mathrm{Re}(Z[\omega])}{R_Q} = \frac{\rho}{1+\left(\frac{\omega}{\omega_R}\right)^2} + r\mathcal{L}[\omega,\omega_0,\gamma] \tag{A.27}$$

where $\mathcal{L}$ is a Lorentzian function:

$$\mathcal{L}[\omega,\omega_0,\gamma] = \frac{1}{\pi}\frac{\gamma\omega_0}{(\omega-\omega_0)^2+\gamma^2} \tag{A.28}$$

We start from the definition of $J(t)$ (equation (1.19)) which can be written:

$$J(t) = \int_{-\infty}^{\infty} \frac{\mathrm{d}\omega}{\omega} r[\omega] \frac{e^{-\mathrm{i}\omega t} - 1}{1 - e^{-\beta\hbar\omega}} \tag{A.29}$$

Then, we derive $e^{J(t)}$ and take the Fourier transform on each side. We obtain:

$$-\mathrm{i}\frac{E}{\hbar}P(E) = \frac{1}{2\pi\hbar}\int_{-\infty}^{\infty} \mathrm{d}t \frac{\mathrm{d}e^{J}}{\mathrm{d}t}(t) e^{\mathrm{i}\frac{Et}{\hbar}} = \frac{1}{2\pi\hbar}\int_{-\infty}^{\infty} \mathrm{d}t e^{J(t)} e^{\mathrm{i}\frac{Et}{\hbar}} \int_{-\infty}^{\infty} \mathrm{d}\omega \frac{r[\omega]}{1 - e^{-\beta\hbar\omega}} (-\mathrm{i}) e^{-\mathrm{i}\omega t} \tag{A.30}$$

We decompose this equation in two parts with the impedance (equation (A.27)):

$$\begin{aligned} \frac{E}{\hbar}P(E) = \int_{-\infty}^{\infty} \mathrm{d}\omega \frac{r\mathcal{L}[\omega, \omega_0, \gamma]}{1 - e^{-\beta\hbar\omega}} P(E - \hbar\omega) + \\ \underbrace{\frac{1}{2\pi\hbar}\int_{-\infty}^{\infty} \mathrm{d}t \int_{-\infty}^{\infty} \mathrm{d}\omega \frac{\rho}{1 + \left(\frac{\omega}{\omega_R}\right)^2} \frac{1}{1 - e^{-\beta\hbar\omega}} e^{J(t)} e^{\mathrm{i}\frac{(E-\hbar\omega)t}{\hbar}}}_{I_\rho(E)} \end{aligned} \tag{A.31}$$

The second term of this equation can be approximately computed due to the specific form of the impedance. $J(t)$ is linear in the impedance and can be written as:

$$J(t) = \underbrace{\int_{-\infty}^{\infty} \frac{\mathrm{d}\omega}{\omega} \frac{\rho}{1 + \left(\frac{\omega}{\omega_R}\right)^2} \frac{e^{-\mathrm{i}\omega t} - 1}{1 - e^{-\beta\hbar\omega}}}_{J_\rho(t)} + \underbrace{\int_{-\infty}^{\infty} \frac{\mathrm{d}\omega}{\omega} r\mathcal{L}[\omega, \omega_0, \gamma] \frac{e^{-\mathrm{i}\omega t} - 1}{1 - e^{-\beta\hbar\omega}}}_{J_\mathcal{L}(t)} \tag{A.32}$$

The next step is to notice that

$$\frac{\rho}{1 + \left(\frac{\omega}{\omega_R}\right)^2} \frac{1}{1 - e^{-\beta\hbar\omega}} \underset{\omega \to 0}{\longrightarrow} \infty \tag{A.33}$$

This means that the asymptotic at $t \to \infty$ dominates the value of the integral $I_\rho(E)$. As $J_\mathcal{L}(\infty)$ is finite, we can fix it to its limit. Therefore, we can write it using [98] for the asymptotic comportment of $J_\rho(t)$ and the Minnhagen type equation for J_ρ alone:

$$\begin{aligned} I_\rho(E) &\approx \frac{1}{2\pi\hbar} e^{J_\mathcal{L}(\infty)} \int_{-\infty}^{\infty} \mathrm{d}t \int_{-\infty}^{\infty} \mathrm{d}\omega \frac{\rho}{1 + \left(\frac{\omega}{\omega_R}\right)^2} \frac{1}{1 - e^{-\beta\hbar\omega}} e^{J_\rho(t)} e^{\mathrm{i}\frac{(E-\hbar\omega)t}{\hbar}} \\ &= \frac{E}{\hbar} e^{J_\mathcal{L}(\infty)} \frac{1}{2\pi\hbar} \int_{-\infty}^{\infty} \mathrm{d}t e^{J_\rho(t)} e^{\mathrm{i}\frac{Et}{\hbar}} = \frac{E}{\hbar} e^{J_\mathcal{L}(\infty)} \frac{1}{2\pi\hbar} \int_{-\infty}^{\infty} \mathrm{d}t e^{-\frac{\rho\pi}{\hbar\beta}|t|} e^{\mathrm{i}\frac{Et}{\hbar}} \\ &= \frac{E}{\hbar} e^{J_\mathcal{L}(\infty)} \frac{1}{\pi\hbar} \frac{\gamma_T}{\gamma_T^2 + \left(\frac{E}{\hbar}\right)^2} \end{aligned} \tag{A.34}$$

where $\gamma_T = \frac{\rho\pi}{\hbar\beta}$.

Finally, we can write with the expression [1] of $J_\mathcal{L}(\infty) \approx -r$:

$$P(E) = \frac{\hbar}{E} \int_{-\infty}^{\infty} \mathrm{d}\omega r\mathcal{L}[\omega, \omega_0, \gamma] P(E - \hbar\omega) + \frac{e^{-r}}{\pi\hbar} \frac{\gamma_T}{\gamma_T^2 + \left(\frac{E}{\hbar}\right)^2} \tag{A.35}$$

as $\hbar(\omega_0 - \gamma) \gg k_B T$.

Appendix B

Fabrication

B.1 ICP etching

Step	Plasma pressure (mT)	Gas	Flow (sccm)	Power (W)	ICP power (W)	Time (s)
Resist removing	10	O_2	50	20	1200	240
LOR removing	10	O_2	50	40	1200	240
Nb etching	5 (15)	SF_6 CH_2F_2 Ar	5 25 40	70 (100)	500	EDP
Nb overetching	20	SF_6 CH_2F_2 Ar	10 10 40	20 (70)	500	30
Al etching	5	Ar	100	150	500	30
Si_3N_4 etching	5 (15)	SF_6 CH_2F_2 Ar	5 25 40	50 (100)	250 (500)	EDP

Table B.1: Etching recipes for the Plasmalab100 from Oxford. The values between brackets are the burst values applied for 5 s to 10 s to initiate the plasma.

Appendix C

Miscellaneous calculation

C.1 Characteristic impedance extraction

In section 2.6.2, we present a lumped elements circuit to model the two first modes of a spiral planar coil. The goal of this appendix is to compute the impedance of the model presented figure 2.11 and to compute the properties of these modes, i.e. resonance frequencies and characteristic impedances.

The impedance of an LC resonator can be written:

$$Z(\omega) = \frac{\mathrm{j}\omega L}{1 - \left(\frac{\omega}{\omega_0}\right)^2} = \frac{\mathrm{j}\frac{\omega}{\omega_0} Z_{\text{eff}}}{1 - \frac{\omega^2}{\omega_0^2}} \tag{C.1}$$

where $Z_{\text{eff}} = \sqrt{\frac{L}{C}}$ and $\omega_0 = \frac{1}{\sqrt{LC}}$

The impedance of the model in figure 2.11 can be written when we connect the side 2 to the ground:

$$Z(\omega) = \frac{\mathrm{j}\omega L_{eq}\left(1 - \frac{\omega^2}{\omega_c^2}\right)}{\left(1 - \frac{\omega^2}{\omega_0^2}\right)\left(1 - \frac{\omega^2}{\omega_1^2}\right)} \tag{C.2}$$

where:

$$L_{eq} = L_1 + L_2 - 2M \text{ with } M = k\sqrt{L_1 L_2} \tag{C.3}$$

$$\omega_c = \sqrt{\frac{L_{eq}}{C_2 L_1 L_2 (1 - k^2)}} \tag{C.4}$$

$$\omega_{0/1}^2 = \frac{1}{2}\left(\omega_c^2 + \frac{\omega_{eq}^2 \omega_c^2}{\omega_M^2} \mp \sqrt{\left(\omega_c^2 + \frac{\omega_{eq}^2 \omega_c^2}{\omega_M^2}\right)^2 - 4\omega_c^2 \omega_{eq}^2}\right) \tag{C.5}$$

with

$$\omega_{eq} = \frac{1}{\sqrt{L_{eq} C_{eq}}} \quad \text{with} \quad C_{eq} = C_1 + C_1' \tag{C.6}$$

$$\omega_M = \frac{1}{\sqrt{C_2 L_2}} \tag{C.7}$$

So we observe two maxima which can be mapped to a LC resonators with characteristic impedance:

$$Z_{eff}(\omega_0) = \frac{L_{eq}\omega_0\left(1 - \frac{\omega_0^2}{\omega_c^2}\right)}{1 - \frac{\omega_0^2}{\omega_1^2}} \tag{C.8}$$

$$Z_{eff}(\omega_1) = \frac{L_{eq}\omega_1\left(\frac{\omega_1^2}{\omega_c^2} - 1\right)}{\frac{\omega_1^2}{\omega_0^2} - 1} \tag{C.9}$$

Notice that two maxima exist when $M < L_2$, otherwise, there is only one solution.

Bibliography

[1] C. Rolland, A. Peugeot, S. Dambach, M. Westig, B. Kubala, Y. Mukharsky, C. Altimiras, H. le Sueur, P. Joyez, D. Vion, P. Roche, D. Esteve, J. Ankerhold, and F. Portier, "Antibunched Photons Emitted by a dc-Biased Josephson Junction", Physical Review Letters **122**, 186804 (2019) (cit. on pp. vii, x, xiii, 7, 13, 36, 105, 106).

[2] A. Grimm, F. Blanchet, R. Albert, J. Leppäkangas, S. Jebari, D. Hazra, F. Gustavo, J.-L. Thomassin, E. Dupont-Ferrier, F. Portier, and M. Hofheinz, "Bright On-Demand Source of Antibunched Microwave Photons Based on Inelastic Cooper Pair Tunneling", Physical Review X **9**, 021016 (2019) (cit. on pp. vii, x, 63).

[3] M. Hofheinz, F. Portier, Q. Baudouin, P. Joyez, D. Vion, P. Bertet, P. Roche, and D. Esteve, "Bright Side of the Coulomb Blockade", Physical Review Letters **106**, 217005 (2011) (cit. on pp. vii, x, xi, 6, 41).

[4] M. C. Cassidy, A. Bruno, S. Rubbert, M. Irfan, J. Kammhuber, R. N. Schouten, A. R. Akhmerov, and L. P. Kouwenhoven, "Demonstration of an ac Josephson junction laser", Science **355**, 939 (2017) (cit. on pp. vii, x, 41).

[5] S. Jebari, F. Blanchet, A. Grimm, D. Hazra, R. Albert, P. Joyez, D. Vion, D. Estève, F. Portier, and M. Hofheinz, "Near-quantum-limited amplification from inelastic Cooper-pair tunnelling", Nature Electronics **1**, 223 (2018) (cit. on pp. vii, x, 41, 64).

[6] Y. M. Blanter and M. Büttiker, "Shot noise in mesoscopic conductors", Physics Reports **336**, 1 (2000) (cit. on p. vii).

[7] C. A. Neugebauer and M. B. Webb, "Electrical Conduction Mechanism in Ultrathin, Evaporated Metal Films", Journal of Applied Physics **33**, 74 (1962) (cit. on p. viii).

[8] T. A. Fulton and G. J. Dolan, "Observation of single-electron charging effects in small tunnel junctions", Physical Review Letters **59**, 109 (1987) (cit. on p. viii).

[9] D. V. Averin and K. K. Likharev, "Coulomb blockade of single-electron tunneling, and coherent oscillations in small tunnel junctions", Journal of Low Temperature Physics **62**, 345 (1986) (cit. on p. viii).

[10] K. K. Likharev, "Correlated discrete transfer of single electrons in ultrasmall tunnel junctions", IBM Journal of Research and Development **32**, 144 (1988) (cit. on p. viii).

[11] P. Delsing, K. K. Likharev, L. S. Kuzmin, and T. Claeson, "Effect of high-frequency electrodynamic environment on the single-electron tunneling in ultrasmall junctions", Physical Review Letters **63**, 1180 (1989) (cit. on p. viii).

[12] L. J. Geerligs, V. F. Anderegg, C. A. van der Jeugd, J. Romijn, and J. E. Mooij, "Influence of Dissipation on the Coulomb Blockade in Small Tunnel Junctions", Europhysics Letters (EPL) **10**, 79 (1989) (cit. on p. viii).

[13] A. N. Cleland, J. M. Schmidt, and J. Clarke, "Charge fluctuations in small-capacitance junctions", Physical Review Letters **64**, 1565 (1990) (cit. on p. viii).

[14] Y. V. Nazarov, "Anomalous current-voltage characteristics of tunnel junctions", Sov. Phys. JETP **68**, 561 (1989) (cit. on p. viii).

[15] M. H. Devoret, D. Esteve, H. Grabert, G.-L. Ingold, H. Pothier, and C. Urbina, "Effect of the electromagnetic environment on the Coulomb blockade in ultrasmall tunnel junctions", Physical Review Letters **64**, 1824 (1990) (cit. on p. viii).

[16] G.-L. Ingold and Y. V. Nazarov, in *Single Charge Tunneling*, NATO ASI Series (Springer, Boston, MA, 1992), pp. 21–107 (cit. on pp. viii, 4, 12, 103).

[17] G.-L. Ingold and H. Grabert, "Finite-Temperature Current-Voltage Characteristics of Ultrasmall Tunnel Junctions", EPL (Europhysics Letters) **14**, 371 (1991) (cit. on p. viii).

[18] T. Holst, D. Esteve, C. Urbina, and M. H. Devoret, "Effect of a Transmission Line Resonator on a Small Capacitance Tunnel Junction", Physical Review Letters **73**, 3455 (1994) (cit. on pp. ix, x, 6).

[19] M. H. Devoret and R. J. Schoelkopf, "Superconducting Circuits for Quantum Information: An Outlook", Science **339**, 1169 (2013), pmid: 23471399 (cit. on p. x).

[20] M. Kjaergaard, M. E. Schwartz, J. Braumüller, P. Krantz, J. I.-J. Wang, S. Gustavsson, and W. D. Oliver, "Superconducting Qubits: Current State of Play", (2019), arXiv:1905.13641 (cit. on p. x).

[21] M. Westig, B. Kubala, O. Parlavecchio, Y. Mukharsky, C. Altimiras, P. Joyez, D. Vion, P. Roche, D. Esteve, M. Hofheinz, M. Trif, P. Simon, J. Ankerhold, and F. Portier, "Emission of Nonclassical Radiation by Inelastic Cooper Pair Tunneling", Physical Review Letters **119**, 137001 (2017) (cit. on pp. x, xiii, 73).

[22] C. Macklin, K. O'Brien, D. Hover, M. E. Schwartz, V. Bolkhovsky, X. Zhang, W. D. Oliver, and I. Siddiqi, "A near–quantum-limited Josephson traveling-wave parametric amplifier", Science **350**, 307 (2015), pmid: 26338795 (cit. on p. xi).

[23] N. Bergeal, F. Schackert, M. Metcalfe, R. Vijay, V. E. Manucharyan, L. Frunzio, D. E. Prober, R. J. Schoelkopf, S. M. Girvin, and M. H. Devoret, "Phase-preserving amplification near the quantum limit with a Josephson ring modulator", Nature **465**, 64 (2010) (cit. on p. xi).

[24] M. A. Castellanos-Beltran and K. W. Lehnert, "Widely tunable parametric amplifier based on a superconducting quantum interference device array resonator", Applied Physics Letters **91**, 083509 (2007) (cit. on pp. xi, 36).

[25] C. M. Caves, "Quantum limits on noise in linear amplifiers", Physical Review D **26**, 1817 (1982) (cit. on p. xi).

[26] J. Govenius, R. E. Lake, K. Y. Tan, and M. Möttönen, "Detection of Zeptojoule Microwave Pulses Using Electrothermal Feedback in Proximity-Induced Josephson Junctions", Physical Review Letters **117**, 030802 (2016) (cit. on p. xii).

[27] J. Bueno, O. Yurduseven, S. J. C. Yates, N. Llombart, V. Murugesan, D. J. Thoen, A. M. Baryshev, A. Neto, and J. J. A. Baselmans, "Full characterisation of a background limited antenna coupled KID over an octave of bandwidth for THz radiation", Applied Physics Letters **110**, 233503 (2017) (cit. on p. xii).

[28] B. Royer, A. L. Grimsmo, A. Choquette-Poitevin, and A. Blais, "Itinerant Microwave Photon Detector", Physical Review Letters **120**, 203602 (2018) (cit. on p. xii).

[29] B. Fan, G. Johansson, J. Combes, G. J. Milburn, and T. M. Stace, "Nonabsorbing high-efficiency counter for itinerant microwave photons", Physical Review B **90**, 035132 (2014) (cit. on p. xii).

[30] S. R. Sathyamoorthy, L. Tornberg, A. F. Kockum, B. Q. Baragiola, J. Combes, C. M. Wilson, T. M. Stace, and G. Johansson, "Quantum Nondemolition Detection of a Propagating Microwave Photon", Physical Review Letters **112**, 093601 (2014) (cit. on p. xii).

[31] Y.-F. Chen, D. Hover, S. Sendelbach, L. Maurer, S. T. Merkel, E. J. Pritchett, F. K. Wilhelm, and R. McDermott, "Microwave Photon Counter Based on Josephson Junctions", Physical Review Letters **107**, 217401 (2011) (cit. on p. xii).

[32] L. C. G. Govia, E. J. Pritchett, S. T. Merkel, D. Pineau, and F. K. Wilhelm, "Theory of Josephson photomultipliers: Optimal working conditions and back action", Physical Review A **86**, 032311 (2012) (cit. on p. xii).

[33] L. C. G. Govia, E. J. Pritchett, C. Xu, B. L. T. Plourde, M. G. Vavilov, F. K. Wilhelm, and R. McDermott, "High-fidelity qubit measurement with a microwave-photon counter", Physical Review A **90**, 062307 (2014) (cit. on p. xii).

[34] K. Inomata, Z. Lin, K. Koshino, W. D. Oliver, J.-S. Tsai, T. Yamamoto, and Y. Nakamura, "Single microwave-photon detector using an artificial Λ-type three-level system", Nature Communications **7**, 12303 (2016) (cit. on p. xii).

[35] R. Lescanne, S. Deléglise, E. Albertinale, U. Réglade, T. Capelle, E. Ivanov, T. Jacqmin, Z. Leghtas, and E. Flurin, "Detecting itinerant microwave photons with engineered non-linear dissipation", (2019), arXiv:1902.05102 (cit. on p. xii).

[36] U. Vool and M. Devoret, "Introduction to quantum electromagnetic circuits", International Journal of Circuit Theory and Applications **45**, 897 (2017) (cit. on pp. 1–3, 6, 14, 58, 101).

[37] M. H. Devoret, "Quantum Fluctuations in Electrical Circuits", Les Houches, Session LXIII **7**, 351 (1997) (cit. on p. 1).

[38] A. A. Clerk, M. H. Devoret, S. M. Girvin, F. Marquardt, and R. J. Schoelkopf, "Introduction to quantum noise, measurement, and amplification", Reviews of Modern Physics **82**, 1155 (2010) (cit. on pp. 1, 14, 58).

[39] A. O. Caldeira and A. J. Leggett, "Quantum tunnelling in a dissipative system", Annals of Physics **149**, 374 (1983) (cit. on p. 3).

[40] G.-L. Ingold and H. Grabert, "Finite-Temperature Current-Voltage Characteristics of Ultrasmall Tunnel Junctions", Europhysics Letters (EPL) **14**, 371 (1991) (cit. on pp. 7, 10, 11).

[41] J. Leppäkangas, M. Marthaler, D. Hazra, S. Jebari, R. Albert, F. Blanchet, G. Johansson, and M. Hofheinz, "Multiplying and detecting propagating microwave photons using inelastic Cooper-pair tunneling", Physical Review A **97**, 013855 (2018) (cit. on pp. 14–16, 19, 20, 49, 95, 96).

[42] A. Roy and M. Devoret, "Quantum-limited parametric amplification with Josephson circuits in the regime of pump depletion", Physical Review B **98**, 045405 (2018) (cit. on p. 14).

[43] A. Grimm, S. Jebari, D. Hazra, F. Blanchet, F. Gustavo, J.-L. Thomassin, and M. Hofheinz, "A self-aligned nano-fabrication process for vertical NbN–MgO–NbN Josephson junctions", Superconductor Science and Technology **30**, 105002 (2017) (cit. on p. 22).

[44] A. Grimm, "Josephson photonics: Statistics of photons emitted by inelastic Cooper pair tunneling", PhD thesis (Grenoble University, Oct. 2, 2015) (cit. on pp. 22, 41, 64).

[45] S. Jebari, "Un amplificateur basé sur le tunneling inélastique de paires de Cooper", PhD thesis (Université Grenoble Alpes, June 26, 2017) (cit. on pp. 22, 64).

[46] S. Nagasawa, K. Hinode, T. Satoh, M. Hidaka, H. Akaike, A. Fujimaki, N. Yoshikawa, K. Takagi, and N. Takagi, "Nb 9-Layer Fabrication Process for Superconducting Large-Scale SFQ Circuits and Its Process Evaluation", IEICE Transactions on Electronics **E97.C**, 132 (2014) (cit. on p. 22).

[47] B. D. Jackson and T. M. Klapwijk, "The current status of low-noise THz mixers based on SIS junctions", Physica C: Superconductivity **372-376**, 368 (2002) (cit. on p. 22).

[48] R. Behr, O. Kieler, J. Kohlmann, F. Müller, and L. Palafox, "Development and metrological applications of Josephson arrays at PTB", Measurement Science and Technology **23**, 124002 (2012) (cit. on p. 22).

[49] *Hypres*, `https://www.hypres.com/foundry/` (visited on 04/03/2019) (cit. on p. 22).

[50] T. Imamura and S. Hasuo, "Fabrication of high quality Nb/AlO/sub x/-Al/Nb Josephson junctions. II. Deposition of thin Al layers on Nb films", IEEE Transactions on Applied Superconductivity **2**, 84 (1992) (cit. on pp. 23, 30).

[51] T. Imamura, T. Shiota, and S. Hasuo, "Fabrication of high quality Nb/AlO/sub x/-Al/Nb Josephson junctions. I. Sputtered Nb films for junction electrodes", IEEE Transactions on Applied Superconductivity **2**, 1 (1992) (cit. on p. 30).

[52] T. Shiota, T. Imamura, and S. Hasuo, "Fabrication of high quality Nb/AlO/sub /x-Al/Nb Josephson junctions. III. Annealing stability of AlO/sub /x tunneling barriers", IEEE Transactions on Applied Superconductivity **2**, 222 (1992) (cit. on pp. 30, 32).

[53] V. Ambegaokar and A. Baratoff, "Tunneling Between Superconductors", Physical Review Letters **10**, 486 (1963) (cit. on p. 30).

[54] V. Ambegaokar and A. Baratoff, "Tunneling Between Superconductors", Physical Review Letters **11**, 104 (1963) (cit. on p. 30).

[55] V. Novotny and P. P. M. Meincke, "Single superconducting energy gap in pure niobium", Journal of Low Temperature Physics **18**, 147 (1975) (cit. on p. 33).

[56] A. W. Kleinsasser, R. E. Miller, and W. H. Mallison, "Dependence of critical current density on oxygen exposure in Nb-AlO/sub x/-Nb tunnel junctions", IEEE Transactions on Applied Superconductivity **5**, 26 (1995) (cit. on p. 32).

[57] H. Sugiyama, A. Fujimaki, and H. Hayakawa, "Characteristics of high critical current density Josephson junctions with Nb/AlO/sub x//Nb trilayers", IEEE Transactions on Applied Superconductivity **5**, 2739 (1995) (cit. on p. 32).

[58] E. Dumur, "A V-shape superconducting artificial atom for circuit quantum electrodynamics", PhD thesis (Université Grenoble Alpes, Feb. 2015) (cit. on p. 35).

[59] C. Altimiras, O. Parlavecchio, P. Joyez, D. Vion, P. Roche, D. Esteve, and F. Portier, "Tunable microwave impedance matching to a high impedance source using a Josephson metamaterial", Applied Physics Letters **103**, 212601 (2013) (cit. on p. 36).

[60] M. T. Bell, I. A. Sadovskyy, L. B. Ioffe, A. Y. Kitaev, and M. E. Gershenson, "Quantum Superinductor with Tunable Nonlinearity", Physical Review Letters **109**, 137003 (2012) (cit. on p. 36).

[61] N. A. Masluk, I. M. Pop, A. Kamal, Z. K. Minev, and M. H. Devoret, "Microwave Characterization of Josephson Junction Arrays: Implementing a Low Loss Superinductance", Physical Review Letters **109**, 137002 (2012) (cit. on p. 36).

[62] D. C. Mattis and J. Bardeen, "Theory of the Anomalous Skin Effect in Normal and Superconducting Metals", Physical Review **111**, 412 (1958) (cit. on p. 36).

[63] D. Niepce, J. Burnett, and J. Bylander, "High Kinetic Inductance NbN Nanowire Superinductors", Physical Review Applied **11**, 044014 (2019) (cit. on p. 36).

[64] M.-C. Harabula, T. Hasler, G. Fülöp, M. Jung, V. Ranjan, and C. Schönenberger, "Measuring a Quantum Dot with an Impedance-Matching On-Chip Superconducting LC Resonator at Gigahertz Frequencies", Physical Review Applied **8**, 054006 (2017) (cit. on p. 36).

[65] S. S. Mohan, "The design, modeling and optimization of on-chip inductor and transformer circuits", PhD thesis (Stanford University Stanford, CA, 1999) (cit. on p. 36).

[66] J. Chen and J. J. Liou, "On-chip spiral inductors for rf applications: an overview", Journal of Semiconductor Technology and Science **4**, 149 (2004) (cit. on p. 36).

[67] J. N. Burghartz and B. Rejaei, "On the design of RF spiral inductors on silicon", IEEE Transactions on Electron Devices **50**, 718 (2003) (cit. on p. 36).

[68] D. M. Pozar, *Microwave Engineering, 4th Edition* (Wiley, Nov. 4, 2011), 756 pp. (cit. on pp. 38, 46, 57, 58).

[69] F. Blanchet, "Josephson photonics : microwave generation & amplification in the quantum regime", PhD thesis (Université Grenoble Alpes, Dec. 2018) (cit. on p. 55).

[70] J. H. Nielsen, W. H. Nielsen, M. Astafev, alexcjohnson, D. Vogel, sohail chatoor, G. Ungaretti, MerlinSmiles, Adriaan, S. Pauka, qSaevar, P. Eendebak, S. Droege, P. Eendebak, R. van Gulik, N. Pearson, damazter, A. Corna, damazter2, Thorvald-Larsen, A. Geller, euchas, V. Hartong, S. Asaad, C. Granade, L. Drmić, S. Borghardt, mltls, GeneralSarsby, and A. Akhmerov, *QCoDeS/Qcodes: v0.4.0, June 2019 Release*, Zenodo, July 2, 2019 (cit. on p. 55).

[71] M. S. Bartlett, "PERIODOGRAM ANALYSIS AND CONTINUOUS SPECTRA", Biometrika **37**, 1 (1950) (cit. on p. 57).

[72] H. Nyquist, "Thermal Agitation of Electric Charge in Conductors", Physical Review **32**, 110 (1928) (cit. on p. 57).

[73] J. B. Johnson, "Thermal Agitation of Electricity in Conductors", Physical Review **32**, 97 (1928) (cit. on p. 57).

[74] S. Krinner, S. Storz, P. Kurpiers, P. Magnard, J. Heinsoo, R. Keller, J. Lütolf, C. Eichler, and A. Wallraff, "Engineering cryogenic setups for 100-qubit scale superconducting circuit systems", EPJ Quantum Technology **6**, 2 (2019) (cit. on p. 60).

[75] J.-H. Yeh, Y. Huang, R. Zhang, S. Premaratne, J. LeFebvre, F. C. Wellstood, and B. S. Palmer, "Hot electron heatsinks for microwave attenuators below 100 mK", Applied Physics Letters **114**, 152602 (2019) (cit. on p. 60).

[76] J.-H. Yeh, J. LeFebvre, S. Premaratne, F. C. Wellstood, and B. S. Palmer, "Microwave attenuators for use with quantum devices below 100 mK", Journal of Applied Physics **121**, 224501 (2017) (cit. on p. 60).

[77] Z. Wang, S. Shankar, Z. Minev, P. Campagne-Ibarcq, A. Narla, and M. Devoret, "Cavity Attenuators for Superconducting Qubits", Physical Review Applied **11**, 014031 (2019) (cit. on p. 60).

[78] K. Bladh, D. Gunnarsson, E. Hürfeld, S. Devi, C. Kristoffersson, B. Smålander, S. Pehrson, T. Claeson, P. Delsing, and M. Taslakov, "Comparison of cryogenic filters for use in single electronics experiments", Review of Scientific Instruments **74**, 1323 (2003) (cit. on p. 63).

[79] M. Thalmann, H.-F. Pernau, C. Strunk, E. Scheer, and T. Pietsch, "Comparison of cryogenic low-pass filters", Review of Scientific Instruments **88**, 114703 (2017) (cit. on p. 63).

[80] D. H. Slichter, O. Naaman, and I. Siddiqi, "Millikelvin thermal and electrical performance of lossy transmission line filters", Applied Physics Letters **94**, 192508 (2009) (cit. on p. 63).

[81] D. F. Santavicca and D. E. Prober, "Impedance-matched low-pass stripline filters", Measurement Science and Technology **19**, 087001 (2008) (cit. on p. 63).

[82] R. Kalra, A. Laucht, J. P. Dehollain, D. Bar, S. Freer, S. Simmons, J. T. Muhonen, and A. Morello, "Vibration-induced electrical noise in a cryogen-free dilution refrigerator: Characterization, mitigation, and impact on qubit coherence", Review of Scientific Instruments **87**, 073905 (2016) (cit. on p. 64).

[83] C. P. Scheller, S. Heizmann, K. Bedner, D. Giss, M. Meschke, D. M. Zumbühl, J. D. Zimmerman, and A. C. Gossard, "Silver-epoxy microwave filters and thermalizers for millikelvin experiments", Applied Physics Letters **104**, 211106 (2014) (cit. on pp. 65, 66).

[84] B. Huard, H. Pothier, D. Esteve, and K. E. Nagaev, "Electron heating in metallic resistors at sub-Kelvin temperature", Physical Review B : Condensed matter and materials physics **76**, 165426 (2007) (cit. on p. 65).

[85] H. Homulle, "Cryogenic electronics for the read-out of quantum processors", PhD thesis (Delft University of Technology, 2019) (cit. on p. 66).

[86] H. Homulle, S. Visser, B. Patra, and E. Charbon, "Design techniques for a stable operation of cryogenic field-programmable gate arrays", Review of Scientific Instruments **89**, 014703 (2018) (cit. on p. 66).

[87] F. Teyssandier and D. Prêle, "Commercially Available Capacitors at Cryogenic Temperatures", in Ninth international workshop on low temperature electronics - WOLTE9 (June 2010) (cit. on p. 66).

[88] S. S. Gerber, "Performance of high-frequency high-flux magnetic cores at cryogenic temperatures", in Energy Conversion Engineering Conference, 2002. IECEC '02. 2002 37th Intersociety (July 2002), pp. 249–254 (cit. on p. 66).

[89] H. P. Quach and T. C. P. Chui, "Low temperature magnetic properties of Metglas 2714A and its potential use as core material for EMI filters", Cryogenics, 2003 Space Cryogenics Workshop **44**, 445 (2004) (cit. on p. 66).

[90] A. D. Armour, M. P. Blencowe, E. Brahimi, and A. J. Rimberg, "Universal Quantum Fluctuations of a Cavity Mode Driven by a Josephson Junction", Physical Review Letters **111**, 247001 (2013) (cit. on pp. 80, 81).

[91] V. Gramich, B. Kubala, S. Rohrer, and J. Ankerhold, "From Coulomb-Blockade to Nonlinear Quantum Dynamics in a Superconducting Circuit with a Resonator", Physical Review Letters **111**, 247002 (2013) (cit. on p. 80).

[92] H. Wang, M. P. Blencowe, A. D. Armour, and A. J. Rimberg, "Quantum dynamics of a Josephson junction driven cavity mode system in the presence of voltage bias noise", Physical Review B **96**, 104503 (2017) (cit. on p. 80).

[93] B. Kubala, V. Gramich, and J. Ankerhold, "Non-classical light from superconducting resonators coupled to voltage-biased Josephson junctions", Physica Scripta **T165**, 014029 (2015) (cit. on p. 80).

[94] A. D. Armour, B. Kubala, and J. Ankerhold, "Noise switching at a dynamical critical point in a cavity-conductor hybrid", Physical Review B **96**, 214509 (2017) (cit. on p. 80).

[95] W. T. Morley, A. Di Marco, M. Mantovani, P. Stadler, W. Belzig, G. Rastelli, and A. D. Armour, "Theory of double Cooper-pair tunneling and light emission mediated by a resonator", Physical Review B **100**, 054515 (2019) (cit. on p. 82).

[96] W. C. Smith, A. Kou, X. Xiao, U. Vool, and M. H. Devoret, "Superconducting circuit protected by two-Cooper-pair tunneling", (2019), arXiv:1905.01206 (cit. on p. 82).

[97] R. A. Usmani, "Inversion of a tridiagonal jacobi matrix", Linear Algebra and its Applications **212-213**, 413 (1994) (cit. on p. 101).

[98] H. Grabert, G.-L. Ingold, and B. Paul, "Phase diffusion and charging effects in Josephson junctions", EPL (Europhysics Letters) **44**, 360 (1998) (cit. on p. 106).